Faculty of Engineering

Experimental and Numerical Investigation of CO_2 Laser Cutting of Carbon/Kevlar Hybrid Composite

Kaveh Moghadasi Koohi

Master of Engineering
2020

Experimental and Numerical Investigation of CO_2 Laser Cutting of Carbon/Kevlar Hybrid Composite

Kaveh Moghadasi Koohi

A thesis submitted

In fulfillment of the requirements for the degree of Master of Engineering

(Mechanical Engineering)

Faculty of Engineering
UNIVERSITI MALAYSIA SARAWAK
2020

DECLARATION

I declare that the work in this thesis was carried out in accordance with the regulations of Universiti Malaysia Sarawak. Except where due acknowledgements have been made, the work is that of the author alone. The thesis has not been accepted for any degree and is not concurrently submitted in candidature of any other degree.

Signature

Name: Kaveh Moghadasi Koohi

Matric No.: 17020109

Faculty of Engineering

Universiti Malaysia Sarawak

Date : 24th November 2020

ACKNOWLEDGEMENT

Foremost, I would like to express my sincere gratitude to my supervisor, Ir Dr Khairul Fikri Tamrin for the continuous support of my Master study and related research, for his patience, motivation, and immense knowledge. His guidance helped me in all the time of research and writing of this thesis. Additionally, I would like to thank my co-supervisor, Dr Mahshuri Yusof for her support during the study. I am also grateful to the following university staff: Mdm. Hasmiza Kontet and Mr. Sabariman Bakar for their unfailing support and assistance. This research is fully-funded by the Ministry of Higher Education Malaysia with the grant no. F02/FRGS/1619/2017. Last but not the least, I would like to thank my family: My partner, Marzi, for her endless love, kindness and support she has shown during the past two years it has taken me to finalize this thesis. Furthermore, I would also like to thank my parents for their love and support throughout my life.

ABSTRACT

Carbon/Kevlar hybrid composites are increasingly being utilized in aerospace and automotive industries due to their superior structural (both in fatigue and static conditions) and lightweight characteristics. Laser cutting is an effective way to perform precise cutting of the composites due to its non-contact method. Accordingly, use of powerful lasers in cutting of composites is fairly wide to overcome some challenges concerning anisotropic properties of these materials at the expense of large heat-affected zones (HAZs) and kerf width, and fiber pullout. However, use of low power lasers due to possessing lower beam intensity for cutting fiber reinforced composite is not quite common. The situation becomes more challenging when it comes to cutting hybrid composites owing to constituting more than two dissimilar materials. Additionally, complexities in definition of constituents materials properties of hybrid composites has being led to pay less attention in numerical modelling of laser processing of these types of composites, while numerical modelling offers considerable promise to reduce costs associated with trial-and-error process in laser cutting. Therefore, the aim of this study is to investigate low-power CO_2 laser cutting of a synthetic carbon/Kevlar hybrid composite and to introduce a new method of numerical modelling using a novel technique of element deletion during laser movement to achieve kerf characteristics and HAZ. Response surface methodology (RSM) along with Box-Behnken design was employed to understand the interactions between the process parameters such as laser power, cutting speed and standoff distance (SOD), and their effects on the cut quality characteristics including size of HAZ and kerf characteristics. Following this, process parameter optimization was successfully carried out using ANOVA to minimize HAZ and kerf widths in multi-pass scanning. ANOVA shows that medium power level (37.6 W) at maximum level of cutting speed (25 mm/s) and SOD of 51.04 mm are optimum in multi-

pass scanning of carbon/Kevlar composite. Based on these parameters, the experimentally optimized kerf characteristics and HAZ were measured less than 10%. Qualitative measurement using scanning electron microscope was performed to evaluate the effects of process parameters and fiber orientation on fiber pullout, HAZ and material decomposition. Difference between the thermal properties of carbon fibers, Kevlar fibers and polymer matrix (epoxy) was found to influence HAZ and kerf widths. Due to limitation of the experiment to measure thermal stresses, numerical simulation utilizing Abaqus was performed to calculate the stresses and damaged area developed in the cutting region. At the same time, element removal of the ablated composite was successfully predicted using temperature dependent Hashin-damage criteria. It was discovered that the temperature gradient around the fibers is inhomogeneous due to higher thermal conductivity of carbon fibers than Kevlar fibers. Additionally, stress profile shows that the stress generally increases with the number of passes. The numerical simulation agrees well with the experimentally measured HAZ and kerf widths. The study is expected to be the first step towards an application of rules for manufacturability of carbon/Kevlar hybrid composite, specifically in aerospace and automobile industries especially in designing high-stiffness and lightweight structures for ailerons, fuselages, landers, rovers, and satellite buses.

Keywords: Laser cutting, carbon/Kevlar hybrid composite, response surface methodology, finite element modelling

Kajian Eksperimen dan Berangka bagi Pemotongan Laser CO_2 Komposit Hibrid Karbon/Kevlar

ABSTRAK

Komposit gentian hibrid semakin digunakan dalam industri aeroangkasa dan automotif kerana ciri-ciri struktur unggul mereka dan sifatnya yang ringan. Pemotongan laser adalah cara yang berkesan untuk melakukan pemotongan komposit yang tepat kerana kaedah operasinya yang tidak bersentuhan. Penggunaan laser berkuasa tinggi dalam pemotongan komposit ini adalah agak luas untuk mengatasi halangan pemotongan dari segi sifat anisotropik komposit ini. Walau bagaimanapun, ini secara tidak langsung menyebabkan kelebaran zon haba (HAZ) dan saiz pemotongan dan penarikan serat. Walau bagaimanapun, penggunaan laser kuasa rendah untuk memotong komposit bertetulang gentian tidak begitu biasa. Keadaan menjadi lebih mencabar ketika memotong komposit hibrid kerana penyusunan lebih dari dua bahan yang tidak serupa. Selain itu, kerumitan dalam definisi sifat bahan konstituen komposit hibrid telah menyebabkan kesukaran dalam pemodelan numerik pemprosesan laser jenis komposit ini. Pemodelan berangka memberi kelebihan untuk mengurangkan kos yang berkaitan dengan proses percubaan dan kesalahan dalam proses pemotongan. Matlamat utama projek ini adalah untuk mengkaji pemotongan komposit sintetik karbon/Kevlar hibrid menggunakan CO_2 laser kuasa rendah dan memperkenalkan kaedah baharu pemodelan numerik menggunakan teknik pemadaman elemen baharu semasa pergerakan laser untuk mencapai ciri-ciri kerf dan HAZ. Metodologi permukaan tindak balas (RSM) dan reka bentuk Box-Behnken digunakan untuk memahami interaksi antara parameter proses seperti kuasa laser, kelajuan pemotongan dan jarak pemotongan (SOD), dan kesannya terhadap ciri-ciri kualiti pemotongan termasuk saiz HAZ. Pengoptimuman parameter proses telah berjaya dijalankan menggunakan ANOVA untuk

meminimumkan lebar HAZ dan saiz pemotongan. ANOVA menunjukkan bahawa laser pada tahap kuasa sederhana (37.6 W) pada kelajuan maksimum pemotongan (25 mm/s) dan SOD 51.04 mm adalah parameter optimum dalam pemotongan komposit karbon/Kevlar. Penggunaan parameter laser yang telah dioptimumkan menghasilkan HAZ dan saiz pemotongan yang berbeza hanya sebanyak 10%. Pengukuran kualitatif menggunakan mikroskop elektron pengimbasan dilakukan untuk menilai kesan parameter proses dan orientasi gentian terhadap penarikan gentian, HAZ dan penguraian bahan. Perbezaan antara ciri-ciri haba pada gentian karbon, gentian Kevlar dan matriks polimer (epoksi) didapati mempengaruhi HAZ dan kelebaran saiz pemotongan. Oleh kerana kelemahan eksperimen untuk mengukur tekanan haba semasa proses pemotongan, simulasi berangka menggunakan Abaqus dilakukan untuk mengira tekanan haba dan saiz kerosakan yang terhasil akibat pemotongan tersebut. Pada masa yang sama, penyingkiran elemen komposit berjaya diramalkan menggunakan kriteria kerosakan Hashin yang bergantung pada suhu semasa komposit. Keputusan simulasi menunjukkan bahawa kecerunan suhu di sekeliling gentian adalah tidak seimbang kerana keadaan konduktiviti gentian karbon yang lebih tinggi berbanding gentian Kevlar. Selain itu, profil tekanan menunjukkan bahawa tekanan secara amnya meningkat dengan bilangan pemotongan. Keputusan simulasi berangka menunjukkan persamaan dengan HAZ dan saiz pemotongan yang dibuat secara eksperimen. Kajian ini diharapkan dapat menjadi langkah pertama menuju penerapan peraturan untuk pembuatan komposit hibrid karbon/Kevlar, khususnya dalam industri aeroangkasa dan automobil terutama dalam merancang struktur kekakuan tinggi dan ringan untuk aileron, pesawat, pendaratan, rover, dan bas satelit.

Kata kunci: *Pemotongan laser, komposit hibrid karbon/Kevlar, metodologi permukaan tindak balas, pemodelan unsur terhingga*

TABLE OF CONTENTS

LIST OF TABLES

LIST OF FIGURES

LIST OF ABBREVIATIONS

a	Absorptivity
Al_2O_3	Aluminium oxide
ANOVA	Analysis of variance
B_4C	Boron carbide
B_K	Bottom kerf width, mm
CARALL	Carbon reinforced aluminium laminate
CFRP	Carbon fiber reinforced polymer
C_p	Specific heat, W/m˚K^4
CMC	Ceramic matrix composite
CO_2	Carbon dioxide
CW	Continuous wave
DoE	Design of experiment
DPSS	Diode pumped solid state
E_{cl}	Elastic modulus of composite in axial direction to fiber, N/m^2
E_{ct}	Elastic modulus of composite in transverse direction to fiber, N/m^2
E_f	Elastic modulus of fiber, N/m^2
E_m	Elastic modulus of matrix, N/m^2
E_1	Longitudinal elastic modulus, N/m^2
E_2	Transverse elastic modulus, N/m^2
f	Confidence level
FDM	Finite difference method
FEM	Finite element method

FVM	Finite volume method
G_{12}	Shear modulus, N/m^2
GFRP	Glass fiber reinforced polymer
GLARE	Glass reinforced aluminium laminate
HAZ	Heat affected zone, mm
h_c	Convection factor, $W/m^{2\circ}K$
IR	Infrared spectrum
k	Number of the process parameters or variables
K	Thermal conductivity, W/m˚K
K_{cl}	Thermal conductivity of composite in axial direction to fiber, W/m˚K
K_{ct}	Thermal conductivity of composite in transverse direction to fiber, W/m˚K
K_f	Thermal conductivity of fiber, W/m˚K
K_m	Thermal conductivity of matrix, W/m˚K
KFRP	Kevlar fiber reinforced polymer
MMC	Metal matrix composite
MWCNT	Multi-walled carbon nanotube
Nd	Neodymium
P	Laser power, W
PMMA	Polymethyl methacrylate
PPS	Polyphenylene sulphide
Q	Heat source
Q_v	Heat loss
R	Laser beam radius, mm

R_f	Thermal resistance of fiber
R_m	Thermal resistance of matrix
RSM	Response surface methodology
s	Significant level
SiC_p	Particles of silicon carbide
SOD	Standoff distance, mm
S^L	Longitudinal shear strength
S^T	Transverse shear strength
S_{xx}	In-plane stress in x-direction, N/m^2
S_{zz}	In-plane stress in z-direction, N/m^2
TGA	Thermogravimetric Analysis
T_K	Top kerf width, mm
T_K/B_K	Kerf ratio
T_M	Fiber melting temperature
T_s	Surface temperature
T_0	Initial temperature
UV	Ultraviolet spectrum
V	Laser beam velocity
V_c	Volume of composite
V_f	Volume of fibers
V_m	Volume of matrix
V_v	Volume of voids
X^C	Longitudinal compressive strength
X^T	Longitudinal tensile strength
x_i	Value of the i^{th} laser cutting parameters

y	Response
Y^C	Transverse compressive strength
Y^T	Transverse tensile strength
YAG	Yttrium-aluminium garnet
Yb	Ytterbium
Yt	Yttrium
YVO_4	Yttrium vanadate
Z_0	Initial beam position
α	Thermal expansion
β	Coefficient to determine the contribution of the shear stress to the fiber tensile initiation criterion
β_i	Linear coefficient
β_{ii}	Quadratic coefficient
β_{ij}	Interaction coefficient
β_0	Model constant
γ_{12}	Shear strain
ε_{em}	Emissivity
ε_{11}	Normal strain in longitudinal direction
ε_{22}	Normal strain in transverse direction
ν_{12}, ν_{21}	Poisson ratio
ρ	Density, Kg/m^3
ρ_f	Density of fibers
ρ_m	Density of matrix
σ_{SBc}	Stephan-Boltzmann constant, $W/m^{2\circ}K^4$
σ_1	Normal stress in longitudinal direction

σ_2	Normal stress in transverse direction
τ_{12}	Shear Stress
ϵ	Statistical experimental error

CHAPTER 1

INTRODUCTION

1.1 General Introduction

Composites are made by combining two or more constituent materials with significantly different mechanical, thermal and chemical properties to form a new material type with outstanding functional characteristics. The most popular composites are carbon fiber reinforced polymer (CFRP), glass fiber reinforced polymer (GFRP), Kevlar fiber reinforced polymer (KFRP), metal matrix composites (MMC) and ceramic matrix composites (CMC).

CFRP, GFRP and KFRP composites are formed through combination of fibers (carbon or glass or Kevlar) and a thermoset or thermoplastic matrix. Fibers are lightweight, stiff and strong, which provide most of the stiffness and strength of the composites. The polymer matrix binds the fibers together and transfers the load to reinforced fibers (Pesce et al., 2019). In recent years, the use of fiber reinforced polymers in high-performance structural applications has increased dramatically due to developments in processing technology, enabling production of products/parts with excellent strength-to-weight ratio. For instance, GFRP composites are found in fairings, storage room doors, landing gear doors and passenger compartments. CFRP composites are often used in wing boxes, horizontal stabilizers, vertical stabilizers and wing panels (Al-Lami et al., 2018; Kwon et al., 2019). In addition to GFRP and CFRP, KFRP composites are also used for many applications in aerospace, military and automotive industry (Chouhan et al., 2016).

MMC is a special type of composite. MMCs consist of thin sheets of metal alloy alternately bonded to plies of FRP adhesive (Aslan et al., 2018). The most commercially available MMCs are glass reinforced aluminium laminate (GLARE) and carbon reinforced aluminium laminate (CARALL) which are based on high strength glass fibers and carbon fibers, respectively (Khan et al., 2017). The MMCs due to taking advantages from metal and FRP have dominant mechanical properties than conventional FRP laminates or monolithic metals (principally titanium and aluminium) sheets. They offer several advantages such as better failure tolerance to fatigue crack growth and impact damage, especially for aircraft structural applications (Hayat et al., 2019; Suthar & Patel, 2018). In addition, traditional aerospace alloys are consistently being substituted with MMCs in aircraft components and structures (Botelho et al., 2006).

CMC is non-brittle resistant material designed for applications in severe environment such as high temperature, corrosive condition and high stress level. They are characterized by ceramic or carbon fibers embedded in ceramic matrix. Due to their high thermal stability and good corrosion resistance, they are used in long lasting applications and damage-tolerant structures in different industries such as automobiles (brake and clutch systems), mechanical engineering (bearings, ballistic protections) and power generation (heat exchangers) (Du et al., 2018).

To overcome limitations of a singular fiber-reinforcement, a number of hybrid composites have been developed consisting two or more different types of fibers in a common matrix. With right combination of dissimilar fibers, a new hybrid composite can be obtained possessing improved physical and thermal properties which is previously not possible with a single kind of reinforcement. This combination influences a variety of

properties such as the residual strength after impaction (Swolfs et al., 2019), tribological properties (Swolfs et al., 2014), stiffness and fracture performance (Giridharan, 2019). To date, various combinations of reinforcing fibers, such as carbon/Kevlar, glass/Kevlar and carbon/glass have been manufactured which are commercially available in the form of thin-ply composites where thickness varies in the range of fractions of a millimetre thick. For this reason, hybrid composites found applications in both aeronautics and space especially in designing high-stiffness and lightweight structures for ailerons, fuselages, landers, rovers, and satellite buses (Cugnoni et al., 2018).

1.2 Problem Statement

With growing production rates of structures/components required in the aerospace, marine, chemical processing equipment, sporting goods, automobiles and military sectors, there is a necessary demand for time- and cost-efficient manufacturing processes for rapid and volume production (Dubey & Yadava, 2008). Conventional contact method of cutting composites using e.g., milling machine results in high tool wear, poor cut surface quality and delamination (Gaitonde et al., 2008). Advanced cutting methods of the FRP composites include abrasive water jet cutting and ultrasonic cutting. Each has its own benefits alongside its disadvantages. The abrasive water jet cutting has several advantages compared to traditional methods such as the absence of thermal stress and high cutting speed (Vigneshwaran et al., 2018). However, the abrasive water jet cutting suffers from the problem of absorption of moisture and delamination, causing reduction in strength (Turner et al., 2015). Although ultrasonic cutting method produces high end quality cutting of parts, it is inherently very slow process which makes it unsuitable for high volume production (Ning et al., 2017).

Due to limitations of the aforementioned processing methods for cutting composites, laser cutting appears as a promising tool. Common types of lasers currently being used in industries are CO_2, excimer, Nd:YAG and fiber lasers. Laser cutting is an effective way to perform precise cutting due to its non-contact method. Additionally, laser cutting decreases the manufacturing cost because it can be integrated into assembly lines and programmed using computers for fabrication of complex geometrical cuts.

Use of powerful lasers (in the range of a few kW) in cutting of composites is fairly wide to overcome some challenges regarding anisotropic properties of these materials. On the contrary, it is desirable as well as cost-effective to utilize a low-power laser for economic and maintenance benefits, which its final cut characteristics is quite similar to high powerful lasers. On top of this, it is noted that use of lasers for cutting single fibre reinforced composites is quite common as compared to hybrid fibre reinforced composites, while it is seen many researches have previously done on laser cutting of CFRP or KFRP. However, to the best of author's knowledge, no investigation has been performed for cutting carbon/Kevlar hybrid fibre reinforced composite with low-power laser. The difficulties appear when there is a considerable difference between thermal properties of fibers and polymer matrix. The energy required to vaporize the fibers is generally higher than that required for melting the matrix. In contrast, higher thermal conductivity of fibers leads to large thermal energy transfer to the neighbouring matrix, producing large heat affected zone (HAZ), pullout of fibers, matrix decomposition and fiber delamination. In this research, the feasibility of cutting carbon/Kevlar composite using low-power CO_2 laser is investigated.

Numerical modelling of laser cutting of fiber reinforced composites is challenging due to complexity in defining thermal and mechanical properties of constituent materials.

However, numerical modelling offers considerable promise to reduce costs associated with trial-and-error process in the manufacturing industry. Therefore, a new method of numerical modelling of carbon/Kevlar composite using element deletion during laser movement is introduced to precisely predict temperature gradients, stress fields, kerf characteristics and heat affected zone (HAZ) in the cutting region.

1.3 Scope of Study

i. A continuous wave (CW) CO_2 laser is employed to cut 0.3 mm thick carbon/Kevlar hybrid composite.

ii. Laser processing parameters used: a) speed of cutting up to 25 mm/s, b) standoff distance of 50.8 ± 1 mm, and c) power of 38 ± 2 W.

iii. Optimization is performed using analysis of variance (ANOVA) and response surface methodology (RSM).

iv. Numerical modelling of laser heat flux is based on Gaussian laser beam. The laser beam is radially symmetric, and the energy is focused on the top surface of the carbon/Kevlar composite where the direction of cutting is in line with Kevlar fibers.

v. Carbon/Kevlar hybrid composite is modelled as twill weaved pattern. 2D Hashin criteria is considered to model continuum shell elements. Rule of mixtures is utilized to calculate thermo-mechanical properties of carbon/Kevlar hybrid composite.

vi. Temperature dependent Hashin criteria is employed to do element removal from the cutting region.

1.4 Research Questions

i. What are the optimum CO_2 laser parameters for cutting carbon/Kevlar hybrid composite to achieve the best cut characteristics?

ii. What are the parameters affecting decomposition rate and heat distribution?

iii. How to define a Gaussian laser beam and temperature dependent Hashin criteria for precise prediction of cut characteristics, temperature and stress fields?

1.5 Hypothesis

i. Low laser power and high cutting speed would produce small heat affected zone and kerf characteristics of carbon/Kevlar composite.

ii. Anisotropic thermal properties of different fibers and fiber arrangement (90 degree, 45 degree, etc.) may affect decomposition rate and heat distribution, respectively.

iii. User subroutine DFLUX and VUMAT can be employed to define Gaussian laser beam and Hashin criteria using thermo-mechanical properties of carbon/Kevlar composite.

1.6 Objectives

i. To examine the effect of different CO_2 laser cutting parameters on kerf characteristics and heat affected zone (HAZ) of carbon/Kevlar composite.

ii. To determine optimum laser process parameters by response surface methodology (RSM).

iii. To perform numerical simulation of multi-pass CO_2 laser cutting, and compare the cut characteristics with the experiment.

1.7 Chapter Summary

Multi-pass CO_2 laser cutting of carbon/Kevlar hybrid composite is the focus of the present thesis. Current literatures relevant to laser cutting of composites, laser parameter optimization, the effect of selected laser parameters on cut characteristics and ultimately, different numerical simulation methods in laser cutting of composites are reviewed in Chapter 2.

Chapter 3 presents detailed specification of carbon/Kevlar composite used and a CO_2 laser system. Design of experiment (DoE) based on response surface methodology (RSM) is employed to carry out experiments along with a three-factor three-level Box-Behnken design. Thereafter, the method of numerical simulation using ABAQUS interlinked with Fortran is explained, and a novel approach of element deletion based on temperature dependent Hashin criteria is defined to predict kerf characteristics and heat affected zone (HAZ).

Quantitative and qualitative results of experiments for kerf characteristics and HAZ based on analysis of variance (ANOVA) are studied in Chapter 4. The effect of laser parameters on fiber pullout is discussed. Then, the influence of fiber orientation of carbon/Kevlar composite on heat accumulation, extension of HAZ and widening the kerf width are studied. Results are supported by microscope and scanning electron microscope (SEM) micrographs. The results from the analytical and numerical models are then discussed, and temperature gradient and thermal stress are mapped. Numerical quantification is compared with the experiment in this chapter.

Finally, the summary and conclusions from the research, along with possibilities for further work in the future, are discussed in Chapter 5.

CHAPTER 2

LITERATURE REVIEW

2.1 Introduction

In this chapter, an overview about composites and previous research related to laser cutting of composites are discussed.

2.2 Composites

The increase use of products made of different composites is growing dramatically in many industries such as aerospace, shipbuilding, automotive parts, as well as pollution control accessories, buildings construction and electrical components. Major constituents in a fiber reinforced composite material are the reinforcing fibers and a matrix, in which the latter acts as a binder for the fibers. The most popular type of composites is fiber reinforced composite. Among the advantages that can be highlighted are high specific strength and stiffness, excellent corrosion resistance and anisotropic features of the reinforcing material. Manufacturing of a composite structure starts with the incorporation of a large number of fibers into a thin layer of matrix to form a lamina or ply. Fibers can be arranged either in unidirectional, bidirectional or multidirectional orientations. There are two types of fibers: natural and synthetic fibers (manufactured fibers). Synthetic fibers are commonly used in composite related engineering industries and are more expensive than natural fibers. Synthetic fiber-reinforced composites are not degradable due to their high molecular mass and hydrophobic character (Asim et al., 2017). Figure 2.1 depicts the classification of composite materials based on matrix and reinforcement.

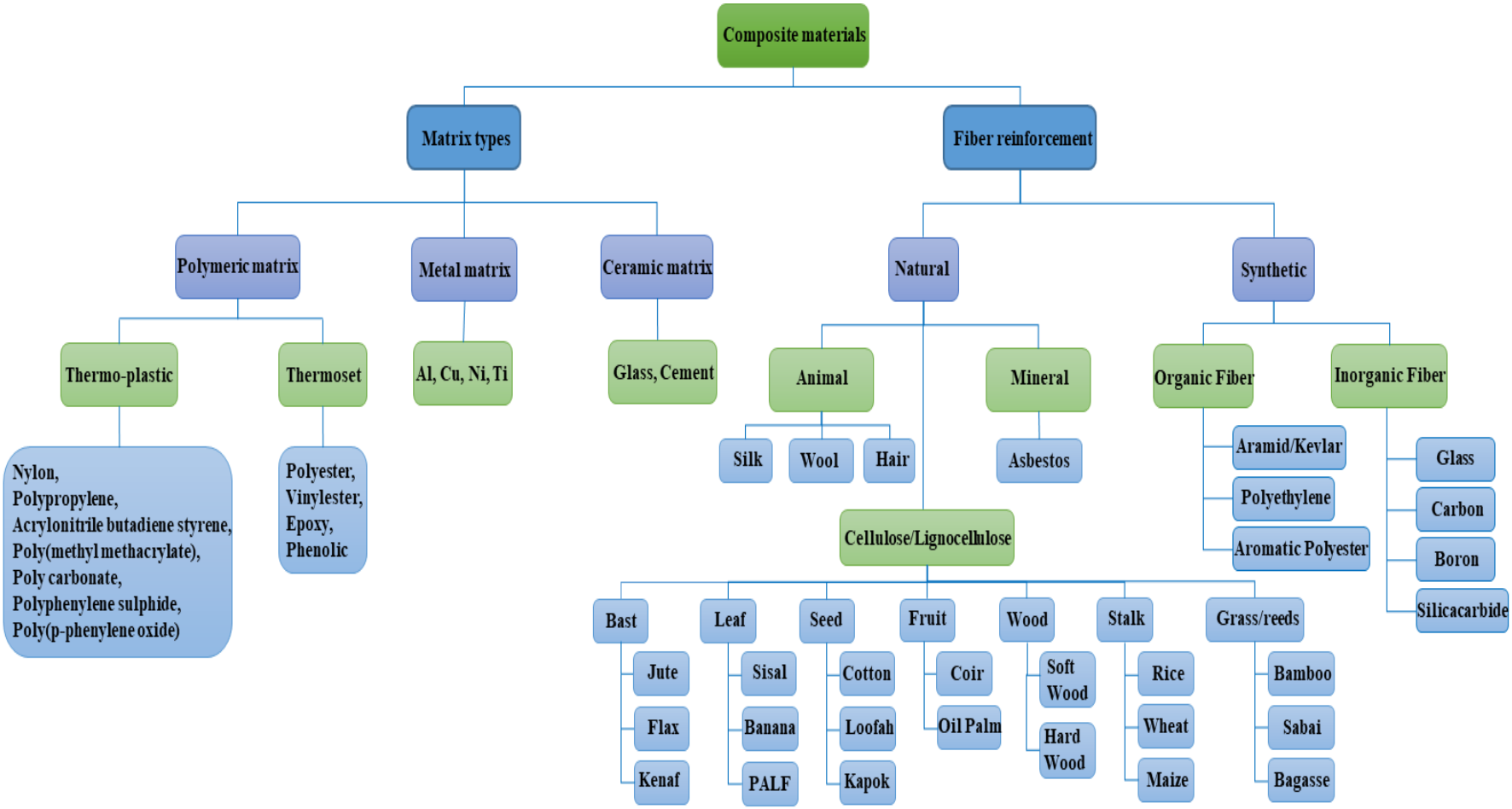

Figure 2.1: Classification of composites based on matrix and fibre reinforcement (Siakeng et al., 2019)

2.2.1 Carbon Fiber Reinforced Polymer (CFRP)

Carbon fiber reinforced polymers (CFRPs), manufactured by compressing and curing polymer matrix and carbon fibers under certain volume fraction and textile pattern, are a kind of composite materials widely used in the aerospace and automotive industries. Carbon fibers are made of graphitic and non-crystalline regions. Poly-acrylonitrile (PAN) is one of the most common precursors employed in carbon fiber production, which offers high tensile strength and higher elastic modulus. In this regard, CFRPs are commercially available with a range of elastic modulus ranging from 207 GPa to 1035 GPa. Among the advantages of carbon fiber composites are their extraordinarily high tensile strength–to–weight ratio, high elastic modulus–to–weight ratio, very low coefficient of linear thermal expansion (which provides dimensional stability in such structures, i.e. space antennas), high fatigue strength, and high thermal conductivity (higher as compare to copper). As a typical class of composite materials used in reality, plain woven CFRP usually presents anisotropic and tension/compression asymmetric characteristics (Mallick, 2007; Zhu et al., 2019).

2.2.2 Kevlar Fiber Reinforced Polymer (KFRP)

Kevlar is an aramid fiber of Poly-para-phenylen-terephtalamide (PPTA) with a rigid molecular structure. Kevlar fibers are the lowest density and the highest tensile strength-to-weight ratio among the current reinforcing fibers. Kevlar 49 is the trade name of one type of the Kevlar fibers available in the market. As a reinforcement, Kevlar fibers are used in many marine, military and aerospace applications where lightweight, high tensile strength and resistance to impact damage are extremely crucial. Some of the most frequent applications of KFRPs include bullet proof vests, cooling vehicles, ship hulls and structural strengthening of civil structures. Nevertheless, Kevlar fibers often present low compression strength. Additionally, the compressive modulus of Kevlar is of the same order as its tensile modulus.

Although, the fibers are compatible with almost any kind of polymeric matrix. Owing to their higher ductility, they are more compatible to Kevlar fibers (Di Ilio & Tagliaferri, 1989; Priyanka et al., 2019).

2.2.3 Glass Fiber Reinforced Polymer (GFRP)

Glass fiber reinforced polymers (GFRPs) are the most common of reinforcing fibers for polymeric matrix composites. The remarkable advantages of glass fibers are high tensile strength, low cost, high chemical resistance and excellent insulating properties. Nowadays, GFRPs are widely used in a variety of engineering applications, such as pipes in the petroleum and mining industries, helicopter rotor blades, pump impeller blades, high-speed vehicles, and aircraft parts. Glass fibers have been employed in various forms such as longitudinal, woven, chopped fiber (distinct) and chopped mats to enhance the mechanical and tribological properties of the fiber reinforced composites. The two types of glass fibers commonly used in the composites industry are E-glass and S-glass. Another type, known as C-glass, is used in chemical applications requiring greater corrosion resistance to acids. E-glass has the lowest cost of all commercially available reinforcing fibers, promoting its widespread use in the FRP industry. S-glass, originally developed for aircraft components, has the highest tensile strength among all fibers in use. However, the compositional difference and higher manufacturing cost make it more expensive than E-glass (Mallick, 2007; Wang et al., 2020).

2.2.4 Hybrid Composite

The incorporation of several different types of fibers into a single matrix has led to the development of hybrid composites. Using a hybrid composite that contains two or more dissimilar fibers, the advantages of one fiber could compensate limitations of the other fiber.

Generally, one type of fiber in the hybrid composite possesses a low modulus and/or lower cost, such as glass or Kevlar, whereas the other type has a greater modulus and/or higher cost, such as boron or carbon fibres. Low modulus fibers make hybrid composites more tolerant to damage and reduce overall costs, while high modulus fiber with more expensive cost provides higher composite stiffness and load bearing capabilities. Hence, a functional composite with a balance in cost and performance can be achieved. There are different types of hybrid composites commercially available such as carbon/Kevlar, Kevlar/glass and carbon/glass. The fiber combination has influence on elastic modulus, fracture energy, tensile and compressive strength of the composite (Gururaja & Rao, 2012; Safri et al., 2018).

2.2.5 Metal Matrix Composite (MMC)

Metal matrix composites (MMCs) owing to their unique physical/mechanical properties and performance have been considered for the applications in automotive and aerospace industries. MMCs possess superior properties at elevated-temperature, high thermal conductivity, high strength and stiffness, high strength-to-density ratio and low coefficient of thermal expansion (Reddy et al., 2018).

2.2.6 Ceramic Matrix Composite (CMC)

Ceramic matrix composites (CMCs) constitute of glass-ceramics, silicon carbide and carbon. These composites represent a new class of integrally woven ceramic-matrix-composites for high-temperature applications, where both the strength and thermal conductivity are important. Their mechanical properties include high strength and high stiffness at very high temperatures, low density, damage tolerance and thermal shock resistance (Whitlow et al., 2016).

2.2.7 Natural Fiber Reinforced Polymer (NFRP)

Natural fiber has recently being considered as a type of renewable source and a new generation of reinforcement for polymer based materials. The use of natural fiber reinforced polymers has become one of the trends among composite materials due to the increasing environmental awareness. Natural fibers are one such proficient material which replaces the synthetic materials and its related products for the less weight and energy conservation applications. The reason can be discovered in their flexibility during processing, the highly specific stiffness, and low cost which has made them suitable choice to manufacturers. Natural fiber reinforced polymer composites can be applied in the automobile, aircraft and packaging industries to cut down on material cost. Low density, low environmental impact and their renewable nature are other important advantages of natural fibers. Based on which part of the plant the fibers are sourced and classified into bast fibers (jute, flax and kenaf), leaf fibers (banana, sisal and pineapple), seed fibers (cotton, loofah and kapok), fruit fibers (coir and oil palm), grass and reed (bamboo, sabai and bagasse), and other types of fibers. Mechanical properties of natural fibers, especially flax, jute and sisal, may compete with synthetic fiber in specific strength (Jariwala & Jain, 2019). Figure 2.2 illustrates the comparison of strength among some fibers.

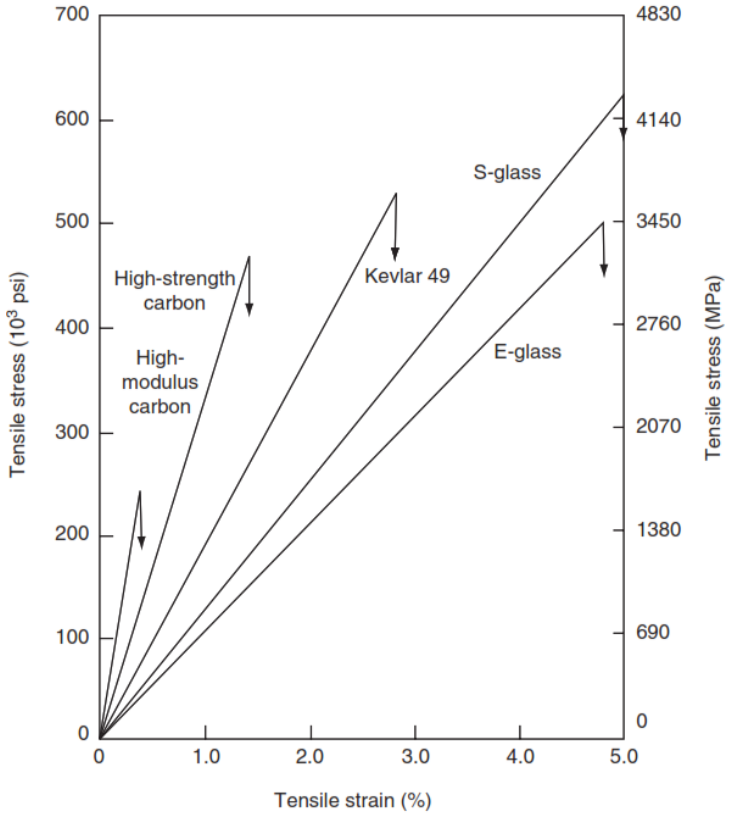

Figure 2.2: Comparison the strength of some fibers (Mallick, 2007)

2.3 Type of Lasers and their Applications

This section discusses type of some lasers and their applications in industries. There are different types of lasers such Nd:YAG, CO_2 and Fiber laser. A Nd:YAG laser is known as solid-state laser. This type of laser can be operated in either pulsed or continuous mode. It can be configured at high peak power enabling cutting of thick materials. Furthermore, due to its short wavelength (approximately 1 µm) it can be absorbed by high reflective materials (Meijer, 2004). A CO_2 laser has wavelength of 10.6 µm operating in the infrared region with power in the range of 40 W to 50 kW (Tabata et al., 1996). Fiber lasers involve the combination of diode pumped solid-state lasers and optical fiber technology. It has a beam quality 10 times better than Nd:YAG laser, low maintenance and high reliability. Disk

laser is one version of a diode-pumped solid-state laser which is depicted in Figure 2.3. The disk is a coin shape YAG crystal doped with ytterbium. This laser can produce over 500 W of high-quality beam at 1.03 μm wavelength (Steen & Mazumder, 2010).

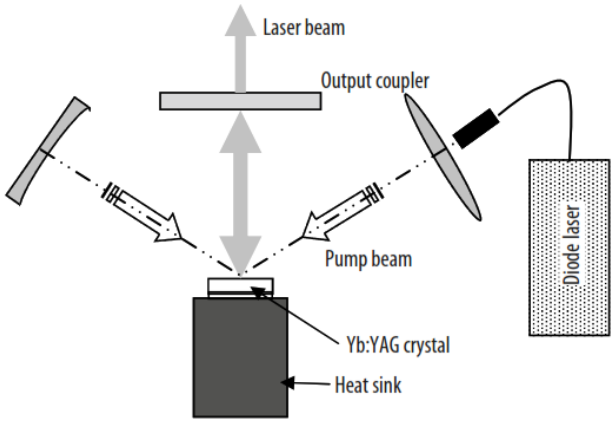

Figure 2.3: The schematic of a disk laser (Steen & Mazumder, 2010)

Now aerospace and automotive industries emphasize the application of laser processing because of its advantage of making precision structures, such as laser cutting, laser drilling, and laser welding. In automotive industry, CO_2 laser processing can be a suitable alternative to the mechanical cutting of automotive stamped part (Russo Spena, 2017). Laser beam welding is a proper method to achieve high static and dynamic strength in the joint. The process has quite a few advantages such as applicability in the atmospheric condition, possessing smaller heat affected zone, aesthetically beautiful and clean joining, and no requirements for post process (Hong & Shin, 2017). Laser drilling is used extensively in modern manufacturing and is a well-established technology for manufacturing micro-holes of various sizes and shapes in the aerospace industry (Marimuthu et al., 2019).

2.4 Effect of Cutting Parameters on Composites

In this section, the influence of cutting parameters on composites in terms of kerf characteristics (kerf width and kerf taper), heat affected zone (HAZ) and surface roughness is investigated, as illustrated in Figure 2.4.

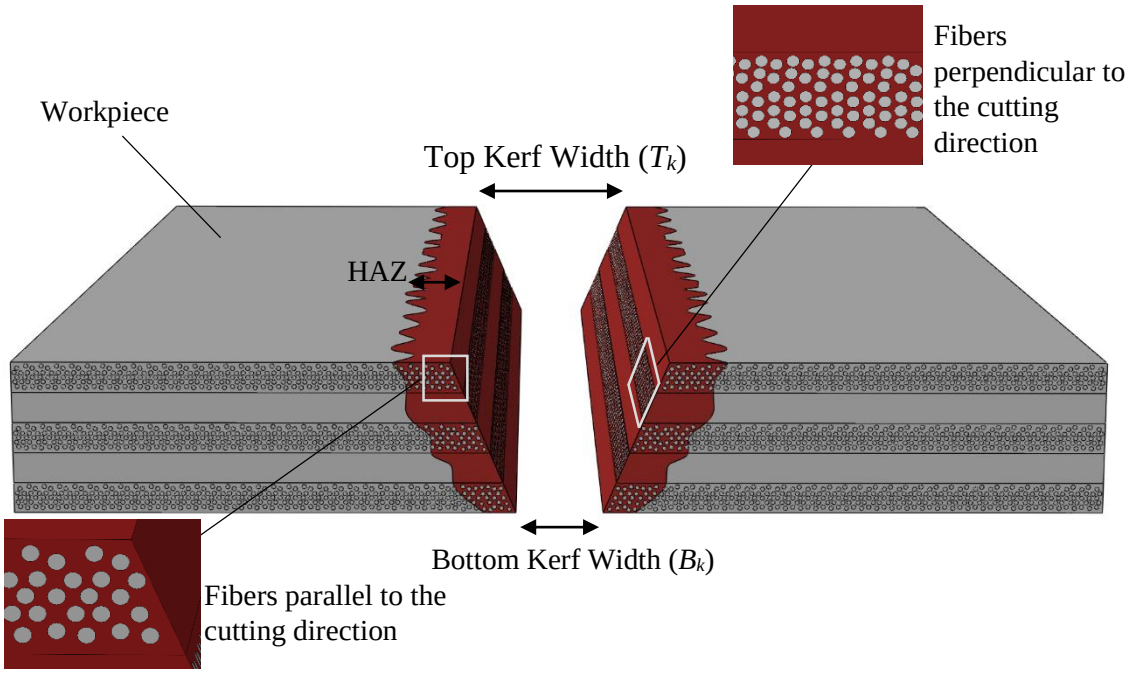

Figure 2.4: The schematic diagram of the composite laser cutting

The top kerf width (T_k) is measured at the entry of the laser beam on the top surface of the specimen which is ablated by the laser heat. Then the laser beam goes through the material and after generating the whole cut, the exit of the beam makes the bottom kerf width (B_k). Furthermore, the kerf ratio is calculated by dividing the top kerf to the bottom kerf (T_k/B_k). Heat affected zone (HAZ) can be defined as a region in which the original substrate experiences both physical deformation and thermal decomposition. This area varies in size based on the power/energy density, process employed and the material properties. Each parameter is studied in separate section.

2.4.1 Kerf Characteristics

Leone and Genna (2018) used Nd:YAG pulsed laser for cutting CFRP composites. In the experiment, spot overlap parameter (R%) was introduced. Results show that the top kerf width is unaffected by the increase of spot overlap at high frequency. On the other hand, the bottom kerf width significantly decreases at high spot overlap frequency. Moreover, the kerf taper increases when the spot overlap parameter at high frequencies decreases. Using Nd:YAG pulsed laser, Yang et al. (2017) also found out that the top kerf is bigger at high pulse frequency and high pulse energy. In addition, top kerf width increases with the increase of pulse frequency and decrease of pulse duration. On the other hand, the kerf taper follows a decrease and then an increase when the cutting speed ascends. Besides, an increase of pulse energy or pulse frequency involved an undesirable increase of kerf taper. Nevertheless, they managed to obtain minimum kerf taper of 2.71°.

Staehr et al. (2016) investigated laser cutting of CFRP using CW and pulsed mode. The CFRPs are made of two types resins, epoxy (EP) and polyphenylene sulphide (PPS). They found out the kerf width generated by pulsed mode are much wider than CW mode for both composites. In this experiment, cutting with pulsed mode requires up to 16 times more repetitions to achieve whole kerf depth than CW mode at 1.5 kW for both composites. On the other hand, pulsed mode for cutting CF-PPS needs less repetition rate than cutting CF-EP.

Herzog et al. (2016) studied laser cutting of 15 mm CFRP using three different methods. In the first method of cutting, laser is focused at the surface of material irrespective of number of passes. This means that the laser remains fixed as the kerf gets deeper. On the other hand, the second method involves changing of focal position with respect to material

surface as the kerf gets deeper. In this way, the focal position remains at the material surface. The third method uses the second method with parallel cutting at each ablation depth. This is illustrated in Figure 2.5. Using the first method, the maximum achievable kerf depth is 7.5 mm for 60 passes. For the second experiment, by retracing the focus position, the kerf width experiences the double size but there is no improvement for the kerf depth. The reason which prevents a further increase in kerf depth is when the focused position moves inside the composite, the beam spot at the top surface increases and part of laser beam cannot enter the pre-existent cutting groove.

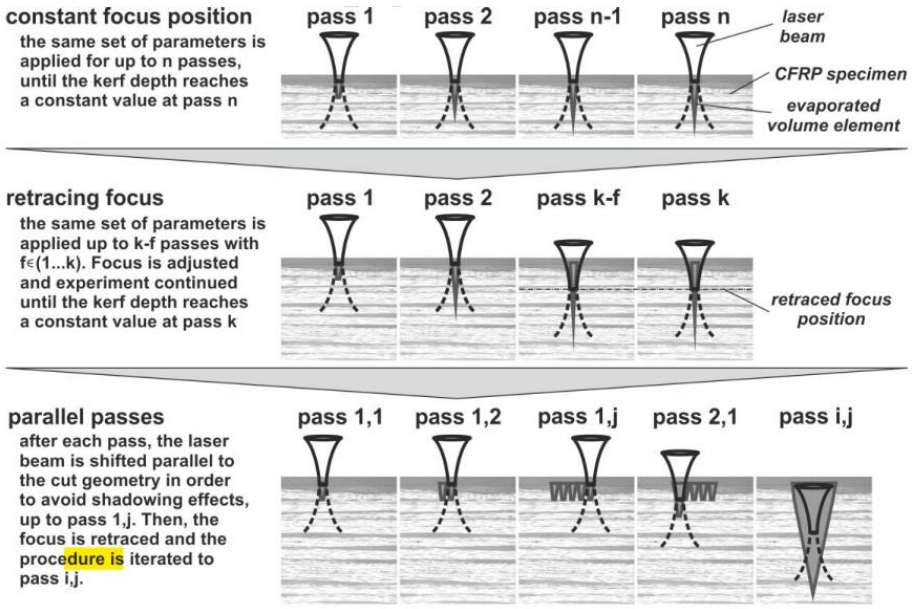

Figure 2.5: The schematic of three different methods for CFRP ablation (Herzog et al., 2016)

Riveiro et al. (2012) investigated the use of CW and pulsed CO_2 laser for cutting CFRP. In CW mode, they found the kerf width increases with the increase of power. However, this results in the decrease of kerf taper angle. It is noted that at constant laser power, the pulse energy increases with the decrease of pulse frequency. In pulsed mode, both

kerf width and kerf taper angle increase with the increase of pulse energy. In particular, the size of kerf width quadratically increases with duty cycle, and its minimum kerf can be obtained at 50% duty cycle. An increase of assist gas pressure was found to cause an increase in taper angle. These findings are quite similar to Yang et al. (2017).

Herzog et al. (2008) performed cutting of CFRP using three different high-power laser sources: a pulsed Nd:YAG laser, a disk laser and a CO_2 laser. Amongst these, the disk laser produced the smallest kerf width.

Jaeschke et al. (2014) studied the influence of 6 kW fiber laser at a wavelength of 1070 nm on cut quality of CFRP. It was noted at constant laser power, the kerf width was found to decrease with the increase of feed rate, and it increases with the increase of laser power.

Kononenko et al. (2014) investigated cutting of bidirectional (perpendicular) and unidirectional (parallel) CFRPs using 27 W picosecond pulsed laser and two different assist gases (oxygen and nitrogen). It was discovered that the kerf width increases with the increase of pulse energy and number of passes. At the same pulse energy (43 J/cm^2) and same number of passes (300), the laser managed to ablate up to sixth and fifth layer for unidirectional and bidirectional, respectively. This is because when the laser beam penetrates inside the composite at which the fibers are parallel to the laser direction, some of the incident beam are reflected partly by the cylindrical surfaces of the fibers. This phenomenon leads to scattering and accumulating of heat to the perpendicular direction of the fibers. This effect results in wider kerf width and deeper kerf depth. They found out oxygen as an assist gas can improve the ablation rate of CFRP with bidirectional layers i.e., deeper kerf depth. The effect of nitrogen gas is similar to when assist gas was turned off.

Salama et al. (2016) also reported the same trend for kerf width using considerably high power 250 kW CO_2 laser. In comparison to nitrogen, oxygen was found good to improve the kerf depth of bidirectional layers.

Leone et al. (2014) employed 20 kW Yb:YAG fiber laser for cutting CFRP. By increasing the scanning speed up to 100 mm/s, both upper and lower kerf increase but these kerfs decrease as the speed reaches 400 mm/s. The increment of pulse power leads to the increase of the upper kerf and decrease of the bottom kerf. Furthermore, the kerf taper angle increases slightly by increasing the effective cutting speed and pulse power.

Using 1070 nm fiber laser at 400 W, Rao et al. (2017) found out that the kerf width increases with the increment of laser power and gas flow rate but it reduces with cutting speed. Similar trend is observed for kerf taper angle. Reduction in kerf width and taper angle at high cutting speed can be attributed to less interaction time between the laser beam and workpiece. In addition, the use of assist gas helps in effective material removal from the cutting zone and prevents high thermal damage but it causes larger taper angle.

Ghavidel et al. (2015) investigated the influence of carbon nanotubes on 120 W CO_2 laser cutting of injection moulded multi-walled carbon nanotubes/polymethyl methacrylate (MWCNT/PMMA) composite. They found out that different amount of MWCNT has various effects on kerf parameters. The increase of kerf width is found linearly proportional with the increase of MWCNT but this trend is seen valid up to 1 wt%. Further increase of MWCNT to 1.5 wt% however results in the decrease of kerf width due to efficient heat conduction to the surrounding as compared to the former. This also contributes to smaller kerf taper angle.

Niino et al. (2014) studied laser cutting of CFRP using a 1090 nm 1 kW CW fiber laser. To cut through the CFRP with minimum kerf width, the power should be minimum at high cutting speed and large number of passes. The number of passes is greatly dependent on material thickness. These findings agree with other literature results (Leone et al. (2014); Rao et al. (2017) Jaeschke et al. (2014); Riveiro et al. (2012)).

Nattapat et al. (2015) studied the possibility of removing the top resin layer of CFRP using 60 W CO_2 laser. The results demonstrate the increase of laser power and decrease of cutting speed lead to more ablation of resin and fiber damage and deeper kerf depth.

Xu and Hu (2017) predicted the ablation depth per scanning pass of laser processing on CFRP using a nanosecond pulsed laser system Nd:YVO_4 . As shown in Figure 2.6, when the spacing distance between neighbouring passes is sufficiently large, the average ablation depth is significantly small. On the other hand, smaller spacing distance causes overlapping of neighbouring passes which causes deeper ablation depth.

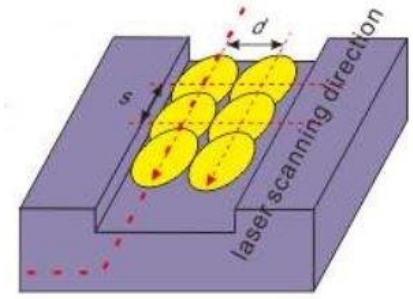

Figure 2.6: Characterization of laser scanning direction (Xu & Hu, 2017)

Negarestani et al. (2010) investigated CFRP laser cutting using Nd:YVO_4 ultraviolet laser. Thermal damage and ablation depth decrease with the increase of cutting speed, leading to shorter fiber pull out. At high cutting speed, more passes are needed to achieve

through cut. Similarly, results of Salama et al. (2016) showed increased ablation rate at high energy and repetition rate using 250 kW CO_2 laser. Using picosecond pulsed laser radiation, Finger et al. (2013) noted increased ablation rate due to superimposed of laser pulses and consequently accumulation of heat in the localized region. In their experiment, Wu et al. (2015) favoured shorter pulse duration to achieve minimum kerf taper at certain ablation depth. Yang et al. (2017) demonstrated faster ablation rate using Nd:YAG pulsed laser at the expense of larger HAZ due to insufficient cooling time.

Nagesh et al. (2017) investigated the influence of adding nickel nano powder and carbon black as nano fillers in CW CO_2 laser cutting of vinyl ester/glass nanocomposite. Adding more nickel nano fillers leads to comparatively small kerf width and char reduction as compared to carbon black. This is because nickel nano fillers covers the glass fibers completely and due to the higher thermal conductivity and lower heat capacity than carbon, they produce lower char after cutting and smaller kerf width.

Fürst et al. (2016) employed CW CO_2 laser and CW Nd:YAG for cutting glass fiber reinforced thermoplastics. They combined two beam radiations with the wavelengths of 1.09 and 10.6 μm. They found out single CO_2 laser has the biggest kerf width compared to other proportions of combined laser beams and single Nd:YAG laser. The reason is that the big spot diameter of the CO_2 laser causes the evaporation of much bigger volume and bigger kerf. On the other hand, high intensity and narrow beam of Nd:YAG laser lead to narrow cutting kerf.

Choudhury and Chuan (2013) investigated cutting quality of GFRP by using single pass and double pass 500 W CW CO_2 laser. The results depict that for the single pass beam, the upper kerf width increases with the increase of assist gas nozzle diameter but it decreases

when the material thickness and cutting speed increase. Additionally, lower kerf width decreases with the increase of nozzle diameter, material thickness and laser cutting speed. The same result can be observed in double pass beam but the difference is that the double pass beam generates lower kerf width as compared to single pass beam.

Al-Sulaiman et al. (2009) investigated the effect of assist gas pressure (nitrogen) and laser power for cutting Kevlar-49 using 2 kW CO_2 laser. They found out the kerf width size increases with the increase of assist gas pressure and laser power. This is because nitrogen prevents oxidation and sideways burning in the cut region. In this case, one would observe high rate of mass removal rate at the expense of reduced cooling effect. Consequently, this leads to increased kerf width and kerf quality.

Yilbas et al. (2010) investigated the influence of 4 kW CO_2 laser on 7050 aluminium alloy reinforced with Al_2O_3 and B_4C particles. It is noted that the increase of laser power results in the increase of kerf width for both types of metal composites. In addition, they discovered the increase of particles percentage leads to the increase of kerf width. The reason is that the increment of reinforcement particles causes the increase of specific heat capacity and reduction of thermal conductivity. In this case, low thermal conductivity decreases the heat loss by conduction, as well as, high specific heat leads to the increase of enthalpy. Therefore, the energy available in the cutting process enhances and the kerf width increases. This trend is similar to findings of Nagesh et al. (2017) who added carbon and nickel nano fillers to GFRP. Furthermore, it should be noted that the presence of B_4C results in less kerf width variation and better cut quality rather than that of Al_2O_3. This is because high temperature oxidation causes Al_2O_3 to reduce to AlO and Al_2O, releasing free O_2 molecules

and forming AlO around the cutting edges. For this reason, black spots were observed around the cutting edge. However, this was not observed for the B_4C particles.

Adalarasan et al. (2015) studied cutting process of Al6061/SiCp/Al_2O_3 metal matrix composite using 3.8 kW pulsed CO_2 laser. They found out that minimum dross height and decreased kerf width can be obtained at high nitrogen gas pressure due to easy ejection of molten metal. In contrast, the combined effect of higher pulse energy at high frequency and lower cutting speed causes overlapping of successive beam spots and re-solidification of the overlapped regions, which in turn ruins the surface finish. Similarly, higher cutting speed and high pulse energy result in poor finish cut due to less interaction time between the material and laser beam. Therefore, a modest level of cutting speed (19.94 mm/s) was found acceptable for better kerf and the quality of cut.

Tong et al. (2013) studied the ablation behaviour of C/SiC composite using a Nd:YAG pulsed laser. The linear ablation rate of the composite increases when the laser power increases. In contrast, the linear ablation rate decreases with prolonged ablation time.

Eltawahni et al. (2011) used a 1.5 kW CO_2 laser for cutting MDF of three different thicknesses. It was found when the focal point position is on the surface, the upper kerf decreases. On the other hand, defocusing the laser beam below the cutting surface results in wider upper kerf width due to enlarged beam spot area. Furthermore, they obtained reduced bottom kerf at high cutting speed with beam spot positioned on the surface of 4 mm and 6 mm thick MDF. Similarly, reduced bottom kerf can be acquired at low cutting speed and deeper focal position.

2.4.2 Surface Roughness

Takahashi et al. (2015) studied the effect of hatching distance for cutting CFRP using 1064 nm 125 W fiber laser. It was discovered that surface roughness decreases with the increase of hatching distance up to 150 µm, but its effect is negligible beyond this value. This is because the increase of hatching distance results in easier laser light penetration into the CFRP and reduced heat accumulation. Therefore, the ejection of ablated material is very smooth resulting in lower surface roughness especially at higher scanning speed. Figure 2.7 defines the scanning direction and hatching distance.

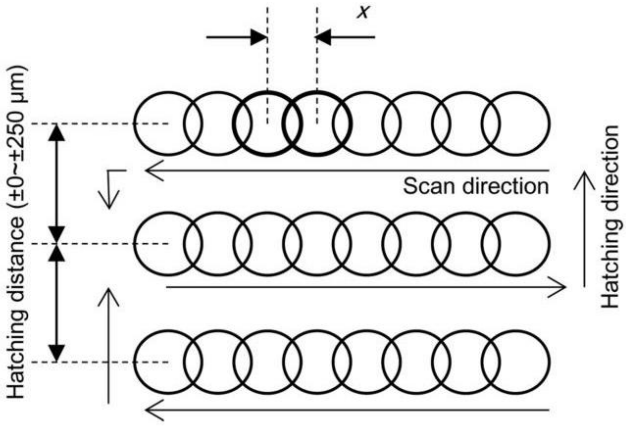

Figure 2.7: Definition of scanning direction and hatching distance (Takahashi et al., 2015)

Karimzad Ghavidel et al. (2016) investigated the effects of adding carbon nanotubes inside the MWCNT/PMMA nanocomposite. The result shows the increase of surface roughness with the increase of carbon nanotubes percentage. This is because higher percentage of carbon nanotubes improves laser-material absorptivity and decreases thermal conductivity (Nagesh et al., 2017; Yilbas et al., 2010). The reduction in thermal conductivity of the nanocomposite causes the solidification of melted material on the surface, roughening

the cut surface. Furthermore, laser power and cutting speed have negligible influence on surface roughness.

Choudhury and Chuan (2013) discovered that the surface finish of GFRP in double-pass CO_2 laser cutting is better than single-pass mode. This is because in single-pass mode the cutting speed was set at low pace to allow through cut but this causes charred surface. On the contrary, in double-pass mode the cutting speed was set at relatively high pace which positively leads to smoother surface and no burnt region. The effect of assist gas nozzle diameter on surface roughness was also investigated in both cutting modes. It was found that the nozzle diameter has insignificant effect on the surface roughness in single-pass laser beam. However, the effect of changing nozzle diameter is more pronounced in double-pass especially at low cutting speed.

Nagesh et al. (2017) found out by adding nano fillers (nickel and carbon black) to the FRP nanocomposites (vinyl ester/glass), surface roughness and quality of surface cut can be improved. In comparison to carbon black, nickel nano powder produces smoother surface and better cut quality due to its higher thermal conductivity and lower heat capacity. This effectively improves heat dissipation and reduces char formation. It was found that char content directly influences surface roughness in which lesser char was observed for composite added with nickel nano fillers.

Al-Sulaiman et al. (2009) studied the effect of assist gas pressure in cutting KFRP. By increasing the assist gas pressure, the surface roughness decreases. At high gas pressure, the extent of burnt kerf reduces due to shielding effect which minimizes oxidation.

Adalarasan et al. (2015) demonstrated the use of nitrogen assist gas at high pressure for easy ejection of molten Al6061/SiCp/Al_2O_3 metal matrix composite in pulsed CO_2 laser cutting. This minimizes dross and improves surface roughness.

Quintero et al. (2011) studied CO_2 laser cutting of phenolic resin board and particleboard. It was noted surface roughness decreases with the increase of laser power. This can be attributed to stable and uniform cutting front at considerably high laser power of 3.5 kW used, producing a cleaner cut. Low surface roughness can also be achieved at deeper focal position (below material surface). However, by increasing the gas pressure, the increase of surface roughness is not appreciable. This result agrees with the findings of Eltawahni et al. (2011).

2.4.3 Heat Affected Zone (HAZ)

Leone and Genna (2018) studied laser cutting of CFRP using Nd:YAG pulsed laser. They found out high pulse energy at low frequency and high cutting speed lead to low HAZ. On the contrary, bigger HAZ was obtained for low pulse energy at high frequency and low cutting speed. It was found the maximum HAZ extension occurs at the centre of the laminate in the range 170-1600 µm.

Yang et al. (2017) evaluated the effect of Nd:YAG pulsed laser cutting quality of CFRP. They discovered that HAZ increases with the increase of pulse frequency, pulse duration and pulse energy. The increase of both pulse frequency and pulse duration have effect similar to laser operating in continuous mode.

Staehr et al. (2016) studied the influence of two different type of lasers for cutting CFRP; a single mode fiber laser emitting continuous wave and a high power thin disk laser

emitting nanosecond pulses. They figured out the former produces small HAZ at low cutting speed whereas the latter produces small HAZ at high cutting speed.

Herzog et al. (2016) experimentally studied cutting of 15 mm CFRP. They used three methods (Figure 2.5). In the first method, laser is focused at the surface of material regardless of number of passes. In the second method, the focal position changes proportionally relative to material surface as the kerf gets deeper. Third method uses the second method with parallel cutting at each ablation depth. In overall, the HAZ is unaffected by all these three methods.

Bluemel et al. (2015) investigated two different HAZ measurements using thermography for surface temperature and thermocouples for internal body temperature. The measured temperature at the specified distances from the cutting edge by these two methods states that the HAZ decreases when the distance from the cutting region increases. This trend is similar for both surface and internal body of composite. In general thermography is more appropriate for HAZ measurement as compared to thermocouple due to its non-contact method.

Xu and Hu (2017) studied the effect of HAZ after cutting CFRP using a Nd:YVO_4 nanosecond pulsed laser system. It was observed high overlapping rate and low scanning speed can contribute to large HAZ at the expense of reduced machining efficiency.

Herzog et al. (2008) investigated the influence of three types of laser sources on the cut quality of CFRP: a pulsed Nd:YAG laser (λ = 1064 nm), a disk laser (λ = 1030 nm) and a CO_2 laser (λ = 10600 nm). They indicated the dimensions of the HAZ depends on the laser wavelength where the pulsed Nd:YAG laser and the CO_2 laser produce the smallest and the largest HAZ, respectively. Moreover, they showed the fiber orientation can influence the

size of HAZ and tensile strength. When the fibers are perpendicular to the cutting direction, the measured HAZ increases which results in the decrease of tensile strength. This can be attributed to thermal damage of the fibers within the HAZ region. In contrast, reduced HAZ and improved tensile strength were obtained when cutting direction is parallel to the fiber orientation.

Riveiro et al. (2012) studied the effect of both CW and pulsed CO_2 laser on the cutting quality of 3 mm CFRP. In CW mode, the increase of power leads to the increase of HAZ. Similarly, the increase of duty cycle causes the increase of HAZ. It was found the increase of assist gas pressure does not have significant effect on the reduction of HAZ. Furthermore, due to high thermal conductivity of carbon fibers and the conduction of heat along the fibers, the extent of HAZ in cutting perpendicular to the fiber axis is higher (Herzog et al. (2008)).

Takahashi et al. (2016) investigated cutting parameters of CFRP using Nd:YAG laser for both ultraviolet (UV-λ=266 nm) and infrared (IR-λ=1064 nm). They found out HAZ produced by IR irradiation is wider than that of UV irradiation. This is because irradiation by IR laser allows the laser beam to pass through the resin and subsequently absorbed by the carbon fiber underneath the resin. In contrast, UV light heats only the resin surface. Hence, heat propagation in the former case is comparatively larger than that of the latter, producing greater HAZ.

Li et al. (2010) investigated laser cutting of CFRP using a nanosecond pulsed diode pumped solid state Nd:YVO_4 (DPSS) UV laser for achieving minimum HAZ. They discovered nanosecond laser–material interaction time is favourable to decrease HAZ at high

scanning speed. Use of this type of laser causes minimum polymer burn out and reduced HAZ as compared to CW CO_2 laser (Davim et al. (2008); Muramatsu et al. (2015)).

Negarestani et al. (2010) investigated the effect of cutting speed for cutting CFRP using a 355 nm DPSS Nd:YVO_4 ultraviolet laser machine. The result indicates higher cutting speed is favourable to ensure controlled decomposition of the polymer matrix. Reduced HAZ can be attributed to shorter fiber pull out and less burning on the cutting edges.

Jaeschke et al. (2014) investigated the impact of thermal damage on cutting CFRP using a 6 kW fiber laser. At constant laser power 6 kW, they found the width of HAZ decreases with the increase of cutting speed. On the other hand, by altering the laser power at a constant cutting speed, the width of HAZ remains constant. They showed a decrease of HAZ results in the increase of tensile strength (Herzog et al. (2008); Muramatsu et al. (2015)).

Leone et al. (2014) did experiments on laser cutting of CFRP using Q-Switched Yb:YAG fiber laser. They found out the increment of either scanning speed or the pulse power contributes to a decrease in HAZ. The reason is that the increase of scanning speed allows a better cooling of the composite and consequently a reduction of the cutting temperature. Similarly, the increase of pulse power allows efficient material removal and this mitigates heat conduction and absorption to the neighbouring regions. All these effects contribute to reduction in HAZ.

Muramatsu et al. (2015) investigated the effect of HAZ on the tensile strength of CFRP. They used three different types of lasers; (1) a CO_2 laser (λ = 10.6 μm) with a processing speed of 1.0 m/min and a power of 800 W, (2) a single-mode fiber laser (λ = 1.06 μm) with a processing speed of 1.0 m/min and a power of 350 W and (3) a single-mode fiber

laser (λ = 1.06 μm) with a processing speed of 7.0 m/min and a power of 2 kW. Of these, the fiber laser produces the lowest HAZ when set at high laser energy and high cutting speed (Leone et al. (2014)). This favourably results in high tensile strength (Jaeschke et al. (2014)).

Herzog et al. (2015) studied the effect of 30 kW Yt:YAG fiber laser on cutting CFRP by separately applying one-pass and multi-pass strategies. They obtained minimum HAZ of 139 μm in single pass strategy at maximum power and maximum cutting speed of 1.2 m/s. On the contrary, in multi-pass strategy, the optimum passes required to acquire minimum HAZ (78.3 μm) is 12. The increase in number of passes results in a steep increase of HAZ. Furthermore, decreasing the delay time below 100 ms between 2 passes causes sharp increase in HAZ. The same trend can be observed by decreasing the interaction time between the material and the laser beam below 10 μs (Leone and Genna (2018); Leone et al. (2014)).

Takahashi et al. (2015) studied the effect of hatching distance on the cut quality of CFRP using 125 W pulsed fiber laser. It was observed HAZ decreases when both hatching distance and scanning speed increase. This is because narrower hatching distance causes heat accumulation inside the groove and consequently an increase in HAZ. On the other hand, larger hatching distance allows easier penetration of the laser light into the substrate and reduction of heat accumulated inside the groove. As a result, the measured HAZ is significantly smaller.

Karimzad Ghavidel et al. (2016) studied the effect of 130 W CO_2 laser on the cutting quality of MWCNT/PMMA nanocomposite. The nanocomposite was fabricated using injection moulding technique where carbon nanotubes are usually aligned in the direction of flow injection. The increase of MWCNT percentage leads to the increase of HAZ and the burr in the direction of flow injection. Similarly, the power increase results in larger HAZ

and burr. On the other hand, HAZ and burr increase by increasing the MWCNT percentage in perpendicular to the flow injection. In the latter case, HAZ is comparatively unchanged but burr decreases with the increase of laser power. It is noted the increase of cutting speed leads to the decrease of HAZ and burr for both carbon nanotubes alignments.

Rao et al. (2017) studied the effect of laser cutting parameters on cut surface integrity of CFRP. It was observed that the HAZ increases when the laser power and assist gas increase. In addition, the HAZ decreases when the cutting speed increases due to less exposure time. As a result, the melting zone adjacent to HAZ appears narrower.

Ghavidel et al. (2015) investigated the effect of carbon nanotubes on laser cutting of MWCNT/PMMA nanocomposite by using 60 W CW CO_2 laser. Thermal conductivity was found to increase with the increase of the amount of carbon nanotube percentage. This resulted in HAZ decrease when the laser power and cutting speed increased.

Salama et al. (2016) studied the influence of 250 kW short pulsed CO_2 laser (8 µs) on the cut quality of CFRP. It was observed higher scanning speed leads to less energy input per unit length to the material and effectively reduces HAZ. They found out slower scanning speed leads to longer laser-material interaction time and larger spot overlaps which in turn creates larger HAZ. It is interesting to note that the HAZ was found minimum at high scanning speed and low/high repetition rate. They demonstrated better quality and lower HAZ than those using continuous CO_2, fiber, and Nd:YAG lasers (Negarestani et al., 2010; Shyha, 2013).

Using a picosecond pulsed laser, Finger et al. (2013) found the width of HAZ is smaller for lower repetition rate. The cause of this effect is that the applied energy for ablation process is superimposed by the accumulation of heat due to overlap of laser pulses.

However, the HAZ is large at high repetition rate which is contrary to finding in (Salama et al., 2016). Furthermore, it is noted that HAZ decreases in higher scanning speeds, but remains constant at repetition rate between 200 kHz to 500 kHz.

Niino et al. (2014) investigated the effect of multi-pass CW IR fiber laser (λ=1090 nm) on cutting 3 mm thick CFRP. It was discovered a linear relationship exists between cutting depth and number of passes at varying scanning speed. In addition, small HAZ was obtained at high scanning speed due to minimum thermal decomposition of the resin and lesser heat accumulation in that region.

Davim et al. (2008) investigated CO_2 laser cutting of two thermosets namely, epoxy resin reinforced with glass fibers and phenolic resin reinforced with Algodon. They found out the HAZ increases with the increase of power, and it decreases with the increase of cutting speed.

2.4.4 Mechanical Strength

Herzog et al. (2008) studied the static strength of CFRPs cut using three different laser sources: a pulsed Nd:YAG laser, a disc laser and a CO_2 laser. They found out the values of static- or bending strength produced by laser methods are far above as compared with conventional machining methods. Moreover, the pulsed Nd:YAG laser produces the highest strength having the smallest HAZ in which there exists a linear relationship between the width of the HAZ and the tensile strength (Jaeschke et al. (2014)). Results show the fiber orientation can influence the static strength where it reduces by about 84 MPa and 35 MPa for a fiber orientation of 90˚ and 45˚, respectively. This implies that static strength effectively decreases with the increase of degree of orientation and HAZ.

Li et al. (2010) investigated the quality of cutting CFRP by using a short pulsed diode pumped solid state (DPSS) UV laser for acquiring minimum HAZ. They found out the bearing strength of CFRP using laser machine has similar failure strength as mechanical cutting.

Jaeschke et al. (2014) studied the impact of thermal damage of a 6 kW fiber laser on the tensile strength of CFRP., The thermal damage in the interlaminar section due to laser cutting shows reduction of maximum shear stress than that of conventional methods (milling and abrasive water jet). While varying the laser power from 550 W to 6 kW at constant feed rate of v=1.2 m/min, it was observed that the output power has minor effect on the static tensile strength. At constant power of 6 kW, the tensile strength increases by 25% by increasing the feed rate from 1.2 m/min to 13.1 m/min.

Muramatsu et al. (2015) reported reduction in stress and increase of HAZ in laser cutting of CFRP sheets using three laser types. In comparison, strength of CFRP specimen cut by 2 kW fiber laser is better than that of 800 W CO_2 laser and 350 W fiber laser.

2.5 Simulations

Three established methods to simulate laser cutting of composites is discussed in this section.

2.5.1 Finite Element Method (FEM)

Negarestani et al. (2010) developed a new model for simulating transient temperature of laser cutting of CFRP using finite element method (FEM). They investigated the effects on ablation depth and HAZ by changing the spacing distance of laser tracks. All surfaces are considered adiabatic except the top surface and the groove side. Increasing the cutting speed

causes the decrease of the thermal damage, HAZ and ablation depth which favourably leads to shorter fiber pull out.

Nattapat et al. (2015) investigated the possibility of removing the top resin layer of CFRP sheet using FEM analysis. They performed both experiment and FEM by considering laser powers (8 W, 14 W and 20 W) and cutting speed of 880 mm/s. The FEM model used in this work is based on heat conduction formulation previously developed by Negarestani et al. (2010). They found out no damage of fibers happens if the power is lower than 8 W. Removal of resin without damage to the layers is possible if the power is between 8 W and 20 W. The substrate damage is more apparent for laser power higher than 20 W. The result of numerical simulation is shown in Figure 2.8. Of various beam overlaps (0%, 25%, and 50%), they discovered 25% beam overlap gives good surface characteristic without damage to layers at laser power of 14 W.

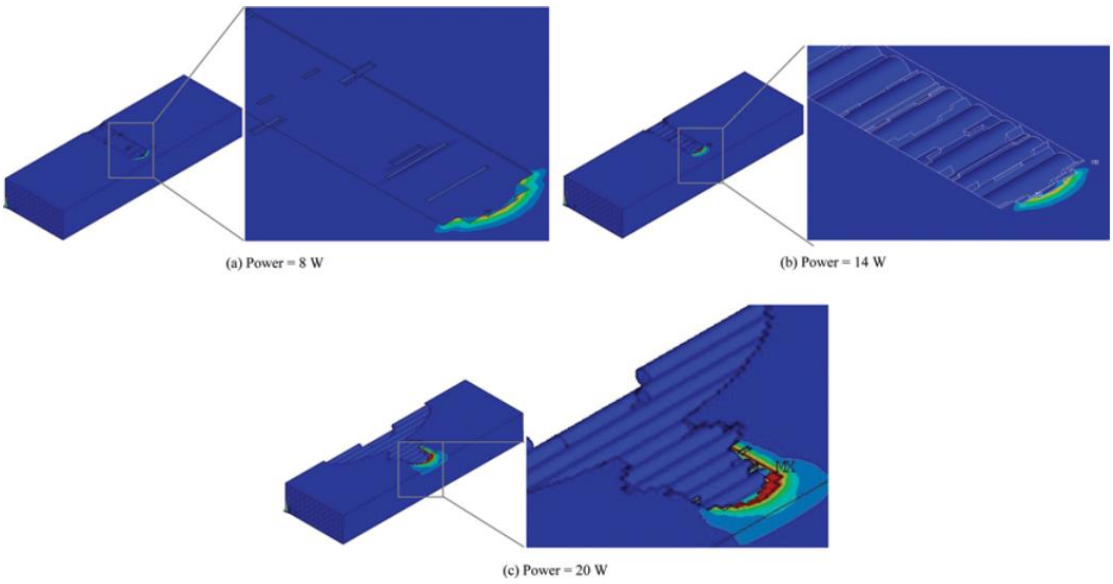

Figure 2.8: The effect of laser power on the ablation characteristics (Nattapat et al., 2015)

Wu et al. (2015) performed experiment and simulated ablation behaviour of CFRP using three different laser operation modes: continuous wave, long duration pulsed wave and short duration pulsed wave lasers. The CFRP model and boundary conditions are illustrated in Figure 2.9. Comparatively, the short duration pulsed laser did not lead to much ablation. Numerical computation shows that the peak temperature developed by CW laser was stabilized around the sublimation point of epoxy. For the cases of pulsed laser, first pulse resulted in ultra-high temperature (over 25,000 K) in the top carbon fabric layer, and then the temperature returned and stabilized around the sublimation point of the epoxy matrix soon after the end of the pulse.

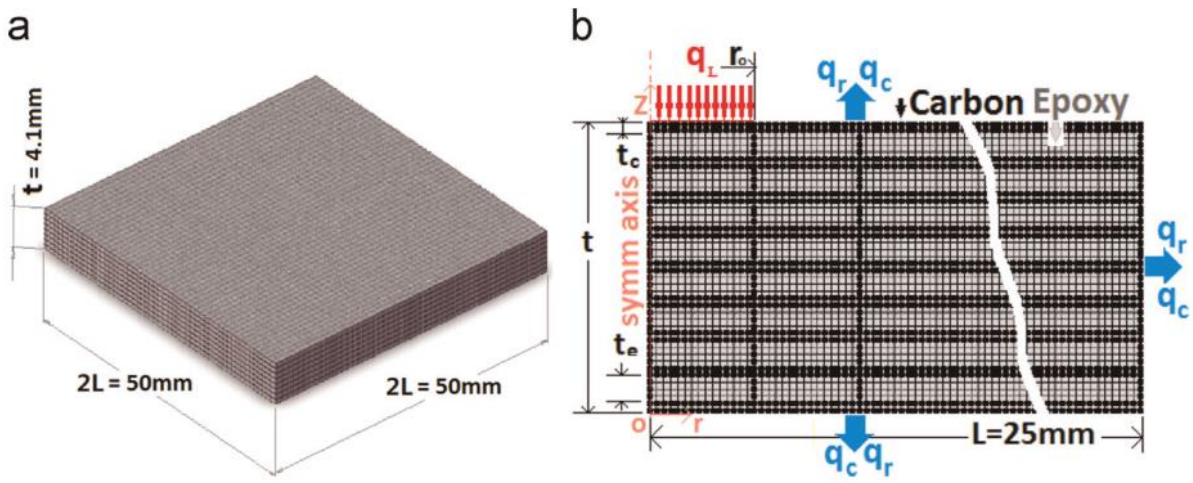

Figure 2.9: CFRP model and definition of thermal loads and boundary condition (Wu et al., 2015)

Liu et al. (2017) performed FEM analysis to calculate the interface stress by studying the inter laminar damages of CFRP using CW CO_2 laser. They utilized heat conduction equation and thermal boundary conditions described by Wu et al. (2015). By increasing the laser power from 500 W to 1000 W, the location of primary cracks come toward to the backward surface of the CFRP. Results show that interlaminar cracks increases with the

increase of power due to increased maximum normal and shear stresses at the interfaces between the lamina.

Sun et al. (2018) used ‘element birth and death’ technique in single-pass unidirectional CFRP laser cutting with and without the assistance of waterjet. Comparatively, smaller HAZ and shallower ablation depth were observed for the former case. In addition, the HAZ remains constant irrespective of varying cutting speeds due to efficient cooling effect of the waterjet. On the other hand, an increase of cutting speed promotes reduced thermal damage for the latter case.

2.5.2 Finite Difference Method (FDM)

Xu and Hu (2017) used finite difference method (FDM) to model ablation of CFRP using single and consecutive short laser pulses. Figure 2.10 shows the model of CFRP and definition of spacing distance between two laser pulses. They found out high overlapping rate can cause reduction of the machining efficiency and enlargement of HAZ. On the other hand, by increasing the power the ablation depth increases.

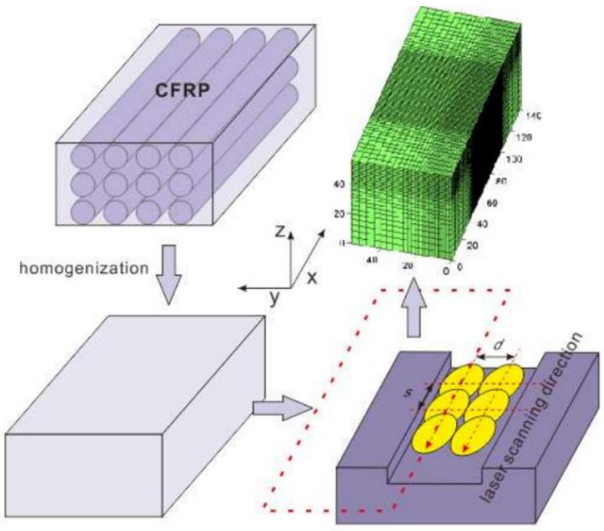

Figure 2.10: The schematic view of CFRP model and laser direction (Xu & Hu, 2017)

2.5.3 Finite Volume Method (FVM)

Ohkubo et al. (2017) performed three-dimensional numerical simulation of cutting CFRP using Finite volume method (FVM) by Open-Foam. A simplified equation model considering the thermal conduction in the CFRP as a time-dependent heat conduction equation was used (Negarestani et al. (2010)). Carbon fiber can be eliminated faster than resin at first stage due to difference in thermal conductivity. Removal of resin is attributed to its low combustion temperature. Figure 2.11 shows the removed length for both fiber and resin.

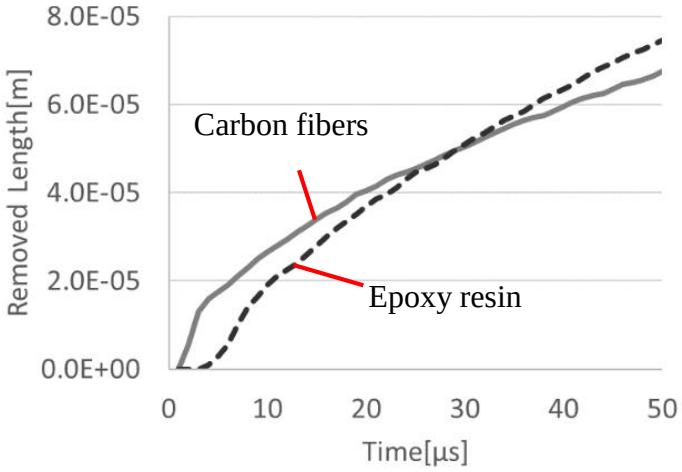

Figure 2.11: Removed length for both fiber and resin (Ohkubo et al., 2017)

2.6 Summary

A of summary this chapter is given in Table 2.1.

Table 2.1: Literature review

Type of laser	Material	Machining condition	Output parameter investigation	References
Nd:YAG	CFRP	150 W, λ= 1064 nm, pulse frequency up to 3 kHz	Kerf characteristics, HAZ extension	Leone and Genna (2018)
Nd:YAG	CFRP	2.5-8 kW, λ= 1064 nm, pulse frequency 10-100 Hz	Kerf characteristics, DoE (CCD)	Yang et al. (2017)
Disk laser (nano second laser in pulsed mode) Fibre laser (CW)	CFRP (EP-PPS)	1.5 kW, Disk laser: λ= 1030 nm, pulse frequency 5-50 kHz Fibre laser: λ= 1070 nm, frequency 5 kHz	Kerf characteristics, HAZ	Staehr et al. (2016)
Yb:YAG (disk laser)	CFRP	6 kW, wave length 1030 nm	Kerf (maximum kerf depth), HAZ	Herzog et al. (2016)
Yt:YAG fiber laser	CFRP	30.5 kW	HAZ	Herzog et al. (2015)
CO_2 (operated CW and pulsed mode)	CFRP	3.5 kW, λ= 10600 nm, pulse frequency 10 Hz- 4 kHz	Kerf characteristics, HAZ, tensile strength	Riveiro et al. (2012)
CO_2 laser, pulsed Nd:YAG laser and Disk laser	CFRP (90˚,45˚)	CO_2 laser: 500 W, λ= 10600 nm, Nd:YAG laser: 18 kW, λ= 1064 nm, pulse frequency between 10-100 Hz Disk laser: 3 kW, λ= 1030 nm	Kerf width, HAZ, tensile strength	Herzog et al. (2008)

Table 2.1 continued

Fiber laser	CFRP	6 kW, wavelength 1070 nm	HAZ, tensile strength	Jaeschke et al. (2014)
Nd:YAG	CFRP	Pulse energy 910 mJ, λ= 1064 nm	HAZ, Numerical simulation	Ohkubo et al. (2016)
Laser	CFRP	--	HAZ, FVM simulation (investigation ablation rate of carbon and epoxy)	Ohkubo et al. (2017)
Picosecond pulsed lase	CFRP	27 W, generating 8 ps pulses at a λ= 515 nm, repetition rate of f=800 kHz	Kerf characteristics	Kononenko et al. (2014)
CO_2 (operated pulsed mode)	CFRP	250 kW, pulse duration 8 μs, λ= 10600 nm	Kerf depth, HAZ	Salama et al. (2016)
Yb:YAG fibre laser	CFRP	20 kW, λ= 1064 nm, pulse frequency 30 to 80 kHz	Kerf characteristics, HAZ	Leone et al. (2014)
Fiber laser	CFRP	400 W	Kerf width, HAZ, DoE (CCD)	Rao et al. (2017)
CO_2	MWCNT/ PMMA	120 W	Kerf characteristics, HAZ, DoE (full factorial method)	Ghavidel et al. (2015)
CW fiber laser	CFRP	1 kW, λ= 1090 nm	HAZ	Niino et al. (2014)

Table 2.1 continued

CO_2	CFRP	60 W	Kerf depth and ablation rate, FEM simulation	Nattapat et al. (2015)
nanosecond pulsed laser system Nd:YVO_4	CFRP	10-20 W, frequency 50 kHz	Kerf depth and ablation rate	Xu and Hu (2017)
Nd:YVO_4 ultraviolet laser	CFRP	10 W, λ= 355 nm, frequency of 40 kHz	Kerf depth and HAZ	Negarestani et al. (2010)
TEA CO_2	CFRP	250 kW, λ= 10600 nm, Pulse repetition rate up to 150 Hz	Kerf characteristics, HAZ, DoE (ANOVA results)	Salama et al. (2016)
picosecond Nd:YAG	CFRP	80 W, λ= 1064 nm, repetition rates adjustable between 0.2 and 10 MHz	Kerf depth, HAZ	Finger et al. (2013)
Nd:YAG (operated in CW and pulsed mode)	CFRP	100 W, λ= 1064 nm	FEM model, kerf taper	Wu et al. (2015)
Nd:YAG	CFRP	single pulse energy up to 8J, λ= 1064 nm, frequency range 10 to 100 Hz	Kerf characteristics, HAZ, DoE (CCD)	Yang et al. (2017)

Table 2.1 continued

Fiber laser	CFRP	125 W, λ= 1064 nm, repetition rate up to 167 kHz	HAZ, surface roughness	Takahashi et al. (2015)
Nd:YAG (UV & IR)	CFRP	Laser energy of 3.9 mJ per pulse, λ= 1064 nm (IR) and 266 nm (UV), repetition rate of 10 Hz	HAZ	Takahashi et al. (2016)
CO_2	CFRP	1 kW, λ= 1080 nm	HAZ	Bluemel et al. (2015)
Fiber laser	CFRP	6 kW, λ= 1070 nm	HAZ, tensile strength	Jaeschke et al. (2014)
Nd:YVO_4 ultraviolet laser	CFRP	10 W, λ= 355 nm, repetition rate of 40 kHz	HAZ, bearing strength	Li et al. (2010)
CO_2 , fiber laser	CFRP	800 W, λ= 10600 nm (CO_2)- 350 W, λ= 1060 nm - 2 kW, λ= 1060 nm (fiber laser)	HAZ, tensile strength	Muramatsu et al. (2015)
CW CO_2	CFRP	1 kW, λ= 1070 nm	FEM analysis (thermal stress distribution)	Liu et al. (2017)

Table 2.1 continued

CO_2	MWCNT/ PMMA	130 W	HAZ, surface roughness	Karimzad Ghavidel et al. (2016)
CW CO_2	GFRP	1.6 kW	Kerf characteristics, HAZ, surface roughness, DoE (grey-Taguchi method)	Nagesh et al. (2017)
Combination of CO_2-slab laser and Nd:YAG	GFRP	3 kW CW (CO_2)- λ= 10600 nm, 1.8 kW CW (Nd:YAG)- λ= 1090 nm	Kerf characteristics	Fürst et al. (2016)
CW CO_2	GFRP	500 W	Kerf characteristics, HAZ, surface roughness, DoE (CCD)	Choudhury and Chuan (2013)
CW CO_2	GFRP	1.7 kW	HAZ	Davim et al. (2008)
CO_2	KFRP	2 kW	Kerf characteristics, surface roughness	Al-Sulaiman et al. (2009)
CO_2	MMC	4 kW	Kerf characteristics	Yilbas et al. (2010)
Nd:YAG	CMC (C/SiC)	laser power densities of 150, 500, 1000 and 1500 W/cm^2, λ= 1064 nm, frequency 20 Hz	Kerf depth and ablation rate	Tong et al. (2013)

Table 2.1 continued

pulsed CO_2	MMC (Al6061/SiCp/Al_2O_3)	3.8 kW	Kerf characteristics, surface roughness, DoE (grey relational generation)	Adalarasan et al. (2015)
CO_2 (CW)	Wood composite (MDF)	1.5 kW	Kerf characteristics, surface roughness, DoE (Box-Behnken)	Eltawahni et al. (2011)
CO_2 (CW)	Wood composite (MDF)	3.5 kW, λ= 10600 nm	Surface roughness	Quintero et al. (2011)

CHAPTER 3

MATERIALS AND METHODS

3.1 Introduction

In this chapter, the methodology adopted to perform the experiment and simulation of CO_2 laser cutting of carbon/Kevlar composite is discussed.

3.2 Material

A rectangular carbon/Kevlar composite sheet (Composite Envisions, USA) with dimension of 100×120 mm^2 and 300 µm thick was used in the experiment (Figure 3.1). The reinforcing materials are T300 carbon fibers and Kevlar-49. It is woven in bi-directional 2x2 twill weave with epoxy resin as a binding element, having density of 0.344 kg/m^3 which corresponds to fiber volume of 60%. It is noted that in the last stage of making the composite, a peel ply fabric was used along with epoxy for curing the composite. After removing the peel ply, the epoxy was imprinted with the shape of weaved fibers of the peel ply (Figure 3.1c and Figure 3.1d). The thermal properties such as specific heat capacity (C_p), thermal conductivity (K) and thermal expansion (α) are given in Table 3.1. The decomposition temperatures of CFRP and KFRP were obtained from TGA results reported in (Isa et al., 2013; Yang et al., 2015). It was discovered that the material decomposition for CFRP and KFRP starts at 823 ˚K and 653 ˚K and 90 percent weight loss occurs at 1073 ˚K and 873 ˚K, respectively. Mechanical properties of CFRP and KFRP at ambient temperature are shown in Table 3.2. E_1 and E_2 are longitudinal and transverse elastic moduli, respectively; G is the shear modulus; υ_{12} is the Poisson ratio.

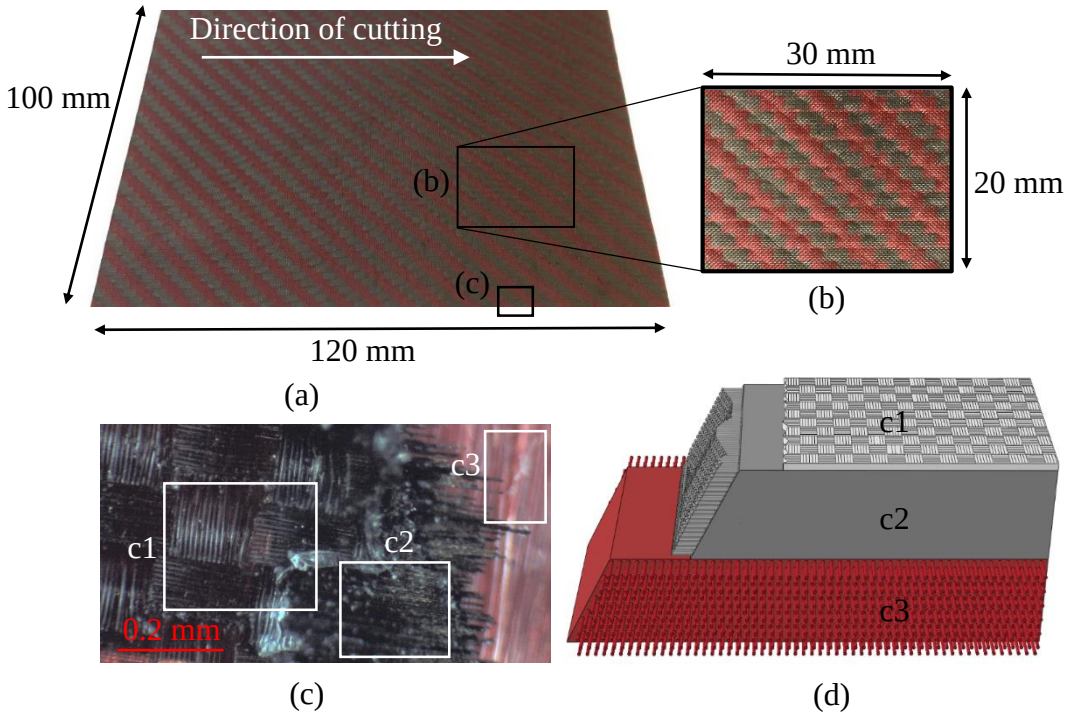

c1: Layer of epoxy (imprinted shape of weaved fibers of peel ply fabric)

c2: Carbon fibers bonded by epoxy

c3: Kevlar fibers bonded by epoxy

Figure 3.1: (a) Sample of carbon/Kevlar composite; (b) enlarged image of weaved fibers; (c) and (d) cross section of carbon/Kevlar composite

Table 3.1: Selected thermal properties at different temperatures of carbon/Kevlar composite (Al-Sulaiman et al., 2009; Negarestani et al., 2010)

Temperature (˚K)	**Specific heat (J/kg ˚K)**		**Thermal Conductivity (W/m˚K)**				**Thermal expansion (1/ ˚K)**			
	CFRP	**KFRP**	**CFRP**		**KFRP**		**CFRP**		**KFRP**	
			Kx	**Ky= Kz**	**Kx**	**Ky= Kz**	**α_1**	**$\alpha_2=\alpha_3$**	**α_1**	**$\alpha_2=\alpha_3$**
298	1008	1464	50	36	0.41	0.41	4e-6	4e-5	2e-6	2e-6
573	1907	2824	35.1	25.6	0.4	0.4	4e-6	4e-5	2e-6	2e-6

Table 3.1 continued

873	1628	2900	24.3	18.4	0.39	0.39	4e-6	4e-5	2e-6	2e-6
1073	1713	2900	19.6	14.9	0.38	0.38	4e-6	4e-5	2e-6	2e-6

Table 3.2: Mechanical properties of carbon/Kevlar composite (Fu & Ye, 2019)

	Mechanical properties					
Material	**E_1 (GPa)**	**E_2 (GPa)**	**υ_{12}**	**G_{12} (GPa)**	**G_{13} (GPa)**	**G_{23} (GPa)**
CFRP	153	10.3	0.28	6	6	3.7
	X^T (MPa)	X^C (MPa)	Y^T (MPa)	Y^C (MPa)	S^L (MPa)	S^T (MPa)
	2537	1580	82	236	90	40
KFRP	**E_1 (GPa)**	**E_2 (GPa)**	**υ_{12}**	**G_{12} (GPa)**	**G_{13} (GPa)**	**G_{23} (GPa)**
	75	9.2	0.28	6.14	6.14	6.14
	X^T (MPa)	X^C (MPa)	Y^T (MPa)	Y^C (MPa)	S^L (MPa)	S^T (MPa)
	1300	280	30	140	60	60

3.3 Experimental Procedure

3.3.1 CO_2 Laser System

A 40 W CO_2 laser system with a wavelength of 10.6 µm operable in continuous mode was used for the experiments. The laser spot size for the focused beam is 200 µm. The focal length of the lens is 50.8 mm. The laser system employs Gaussian beam (TEM_{00}) due to its intensity profile and its consistency along propagation direction. This makes Gaussian beam much easier to use and calibrate (Le et al., 2020). The workable area of the cutting table is 900 mm × 600 mm, controlled by two separate stepper motors for x- and y-directions.

The quality of the laser light, specifically its wavelength purity, can be affected by variations in temperature. In cases where the temperature becomes very high, then the light-emitting components of the laser may also be damaged, which further degrades the quantity and quality of the light produced. Even in applications that do not require precise control of temperature, the majority of the lasers still have to be cooled to avoid overheating of important components and to preserve the service life of the laser. The laser source is continuously cooled by circulating water during the operation. Calibration of the laser tracking system consists of two stages: (a) adjustment of mirror centers, and (b) identification of geometric parameters and lens distance offsets. The interior mirrors must be adjusted, so that the laser beam hits the mirrors centers. The adjustment is a monotonous manual task due to trial and error process. After all mirror centers are properly adjusted, the nominal geometric parameters and distance offsets are measured using a caliper. The top surface of the specimen is considered as a reference of measurement from the ZnSe lens (Figure 3.4).

The exhaust fumes are absorbed by a fume collector which is connected to a fume extraction unit. Figure 3.2 and Figure 3.3 show different parts of the laser system. The laser beam passes through three mirrors and the lens before reaching the workpiece. The laser processing parameters can be controlled by a FABOOL software with maximum cutting speed of 133.3 mm/s. The position of the ZnSe focal lens relative to the top surface of the material is defined as stand-off distance (SOD), as shown in Figure 3.4. At SOD of 50.8 mm, the beam spot is exactly on the surface of the workpiece which is similar to the lens's focal length.

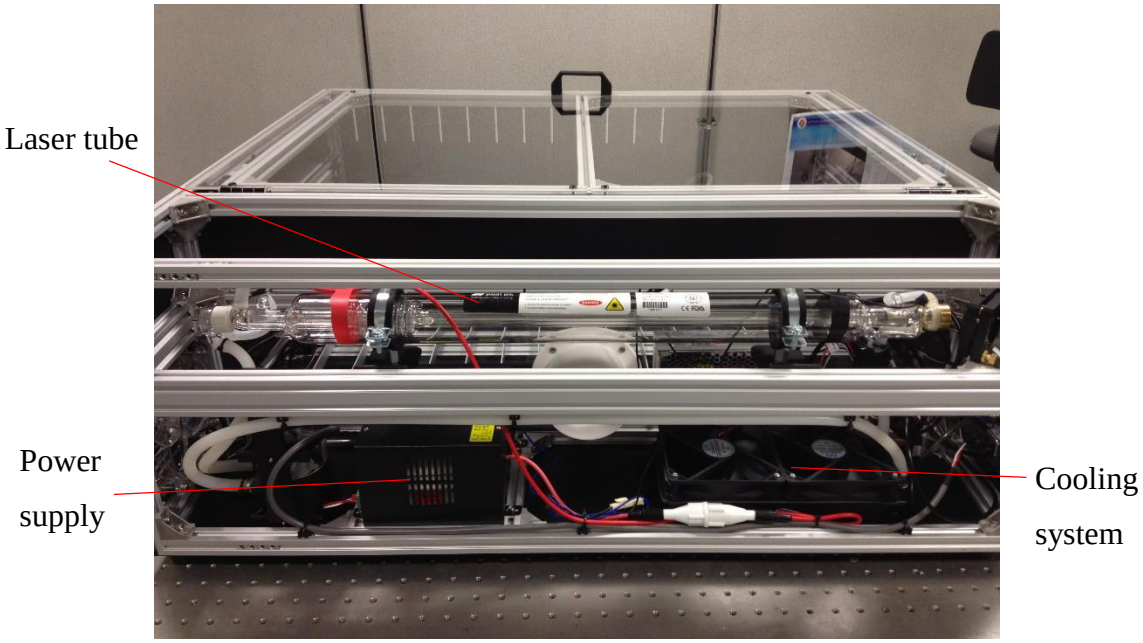

Figure 3.2: CO_2 laser system

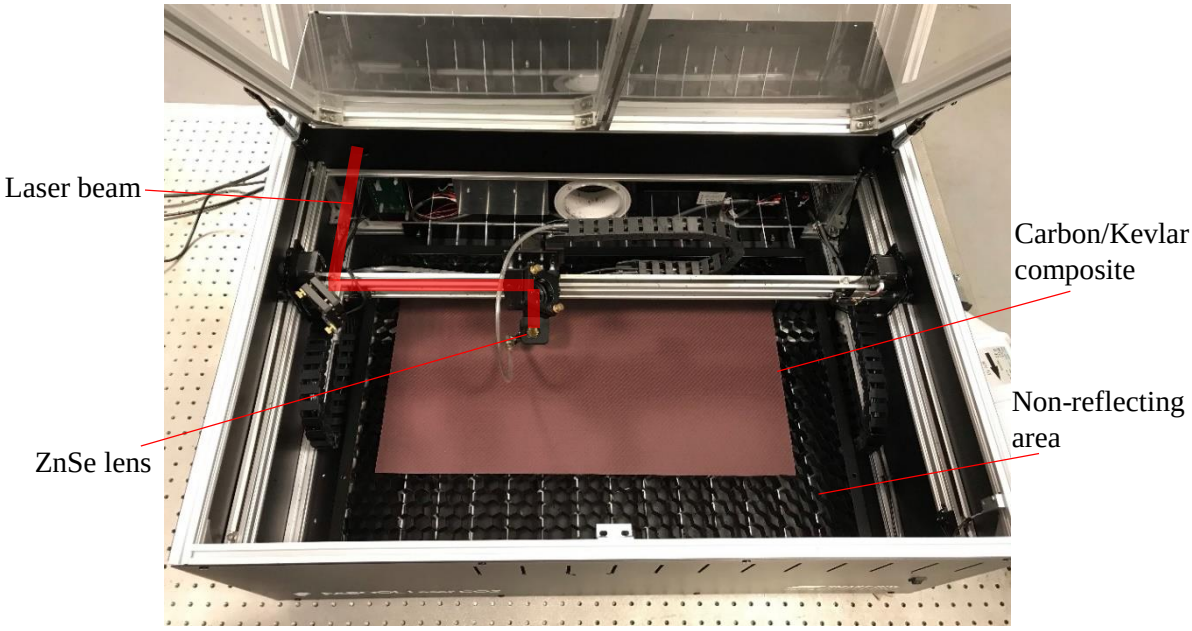

Figure 3.3: Cutting table

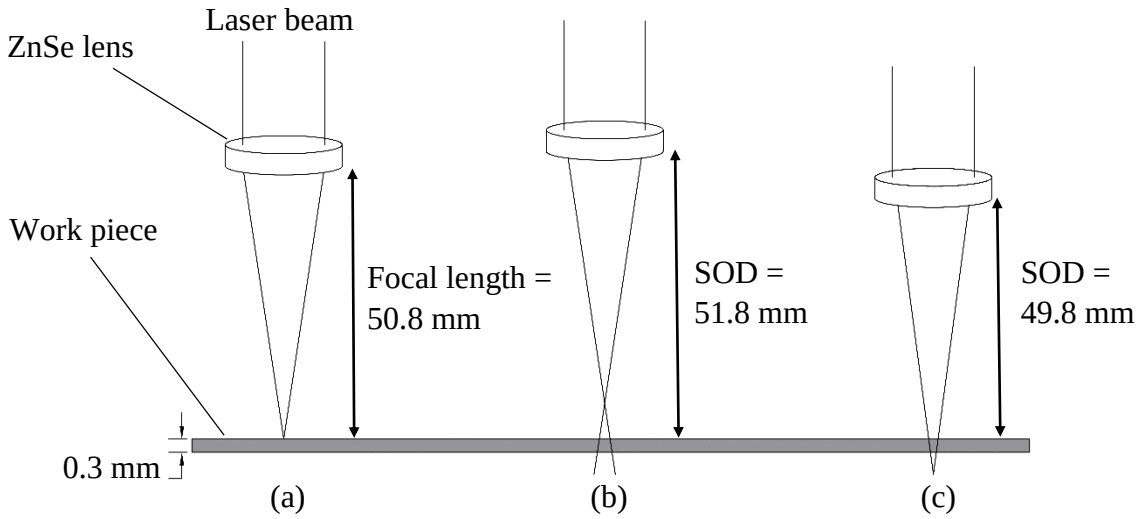

Figure 3.4: Schematic diagram of focal plane position and standoff distance with regard to the surface of the work piece

3.3.2 Optical and SEM Characterization/Measurement

A commercial digital microscope (MD500, AmScope) was used for measuring the heat affected zone and kerf characteristics. A Positive USAF 1951 Test Target was utilized for the calibration and it was found out that it has resolutions of 0.57 and 0.225 µm/pixel for 4x and 10x objectives, respectively. Scanning electron microscopy (SEM; TM3030, HITACHI) was also used for obtaining micrographs of the cut section and its microstructure. Figure 3.5 shows the digital microscope and SEM machine used in the study.

(a) (b)

Figure 3.5: Sample characterization using, (a) digital microscope; (b) SEM machine

3.4 Preliminary Experiment

A number of preliminary tests were performed at 36 W by changing cutting speed and repeating the passes until a complete cut was obtained. Experimentally, the number of passes necessary to completely cut the carbon/Kevlar composite is three. Thereafter, the range of cutting speeds at different laser powers were determined. In contrast, more number of passes were needed for achieving through cut at speed higher than 30 mm/s and laser power less than 30 W. Figure 3.6a shows a sample cut at power 38 W and cutting speed lower than 10 mm/s. In addition, sufficiently long interaction time between laser beam and composite results in excessive carbonization and large heat affected zone along with more carbon fibers pullout and melted Kevlar fibers, as shown in Figure 3.6b and Figure 3.6c. The observed variation of thermal damage can be attributed to lower combustion temperature of Kevlar as compared to carbon fibers (873 ˚K and 1073 ˚K, respectively). The cutting speed, laser power and standoff distance were selected on the basis of these preliminary tests, as

shown in Table 3.3. It should be noted that all linear cuts of 20 mm length were performed in perpendicular to Kevlar fibers and parallel to the carbon fibers.

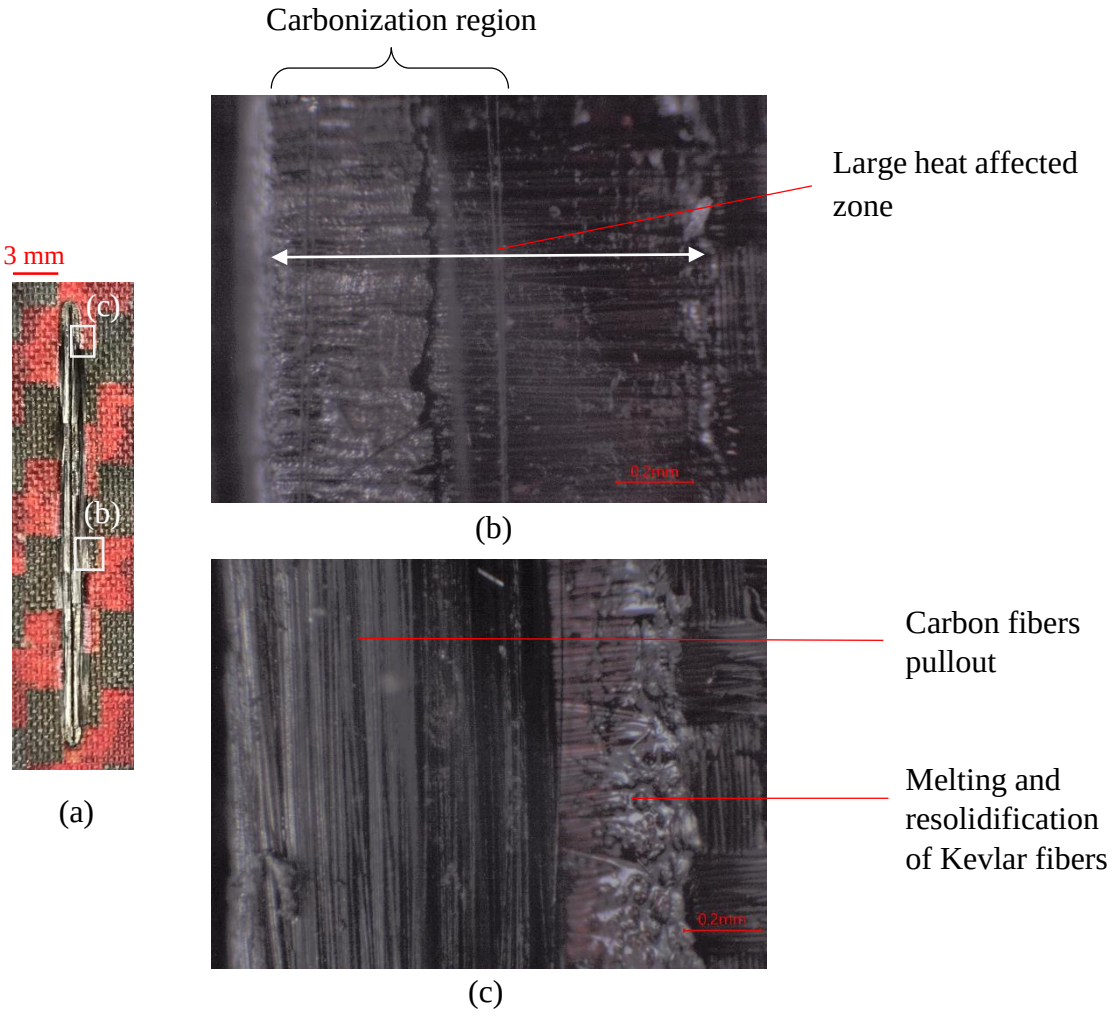

Figure 3.6: Optical micrographs, (a) a sample of laser cut (38 W, 5 mm/s and 50.8 mm SOD); (b) excessive carbonization and large HAZ; (c) carbon fibers pullout and melting of Kevlar fibers

3.5 Laser Processing Parameters

Design of Experiment (DoE) based on response surface methodology (RSM) was employed to systematically carry out experiments within a wide range of process parameters and to find out the optimum cut quality. Carbon/Kevlar composite Table 3.3 shows a three-

factor three-level Box-Behnken design that was developed. The factor levels were coded as –1 (low), 0 (centre point or middle) and +1 (high).

Table 3.3: Input processing parameters based on Box-Behnken design

			Extension		
Parameter	**Unit**	**Annotation**	**-1**	**0**	**+1**
Laser Power	W	Power	36	38	40
Cutting speed	mm/s	Speed	15	20	25
Standoff distance	mm	SOD	49.8	50.8	51.8

In overall, there are 15 sets of experiments as given in Table 3.4. The number of experiments is based on standard order of Box-Behnken design. Three repeats of experiments were conducted for the centre point in order to achieve high accuracy of the statistical analysis. The experiments were performed in a randomized order to reduce the effect of uncontrollable experimental conditions that can influence the results of the experiments and avoid biased experimental results. The mathematical models of the experimental data provide the second-order polynomial equation for the optimization of the process parameters. The following quadratic (second order) polynomial model explains the behaviour of the parameter interactions (Biswas et al., 2010), as shown in Equation 3.1:

$$y=\beta_0+\sum_{i=1}^{k}\beta_i x_i+\sum_{i=1}^{k}\beta_{ii}x_i^2+\sum_{i}\sum_{j}\beta_{ij}x_i x_j+\epsilon \qquad \text{Equation 3.1}$$

where y is the response and x_i is the value of the i^{th} laser cutting parameters; β_0 is the model constant; β_i represents the linear coefficient; β_{ii} denotes the quadratic coefficient; β_{ij} is the interaction coefficient; k is the number of the process parameters or variables; and ϵ is the statistical experimental error. The RSM was carried out at 95% confidence level (f =

0.05) to find the significant input parameters that are affecting the response characteristics using analysis of variance (ANOVA) in a Minitab-18 software. Each response was measured three times to get the average response value.

Table 3.4: Sets of experiments based on Box-Behnken design

Experiment parameters			
No. (Standard order)	**Laser Power (W)**	**Cutting Speed (mm/s)**	**Standoff Distance (mm)**
1	36	15	50.8
2	40	15	50.8
3	36	25	50.8
4	40	25	50.8
5	36	20	49.8
6	40	20	49.8
7	36	20	51.8
8	40	20	51.8
9	38	15	49.8
10	38	25	49.8
11	38	15	51.8
12	38	25	51.8
13	38	20	50.8
14	38	20	50.8
15	38	20	50.8

3.6 Numerical Simulation of Laser Cutting

Based on literature review in Chapter 2, finite element method was chosen for simulating the laser cutting process using Abaqus 6.14 software, primarily to obtain temperature history, residual stress, HAZ and kerf width in the carbon/Kevlar composite.

The software has the capability to interlink with FORTRAN compiler for defining heat source (laser) and material removal. The following discusses laser-material interaction and inter-dependencies of the simulation model.

3.6.1 Rule of Mixtures

The composite property can be considered as the volume weighed average of the phases (matrix and fiber) properties. Here, rule of mixtures is an approach to estimate composite properties based on the following assumptions (Kim, 2000):

i. Fibers are uniformly distributed throughout the matrix.
ii. Perfect bonding between fibers and matrix.
iii. Matrix is free of voids.
iv. Applied loads are either parallel or normal to the fiber direction.
v. Lamina is initially in a stress-free state (no residual stresses).
vi. Fiber and matrix behave as linearly elastic materials.

The relationship between volume fractions (V) of fiber composites is as follows:

$$V_f + V_m + V_v = 1 \qquad \text{Equation 3.2}$$

where f, m and v indices refer to composite, fibers, matrix and void, respectively. Accordingly, the properties of composite (e.g., mass, density, elastic modulus, thermal conductivity or electrical conductivity) are estimated as follow:

Density, ρ:

$$\rho_c = \rho_f . V_f + \rho_m . V_m \qquad \text{Equation 3.3}$$

Elastic modulus, E:

In the axial direction to the fiber orientation:

$$E_{cl}=E_f V_f+E_m V_m$$ Equation 3.4

In the transverse direction to the fiber orientation:

$$\frac{1}{E_{ct}}=\frac{V_m}{E_m}+\frac{V_f}{E_f}$$ Equation 3.5

The estimated thermal conductivity (*K*) based on rule of mixtures (Pan & Hocheng, 2001) in the axial direction to the fiber orientation or along the x axis:

$$K_{cl}=V_f K_f+V_m K_m$$ Equation 3.6

Whereas, in the transverse direction and depth (y and z direction respectively):

$$\frac{1}{K_{ct}}=\frac{V_f}{K_f}+\frac{V_m}{K_m}$$ Equation 3.7

Figure 3.7 depicts thermal resistance model which is used for estimation of thermal conductivity of fiber and matrix constituents.

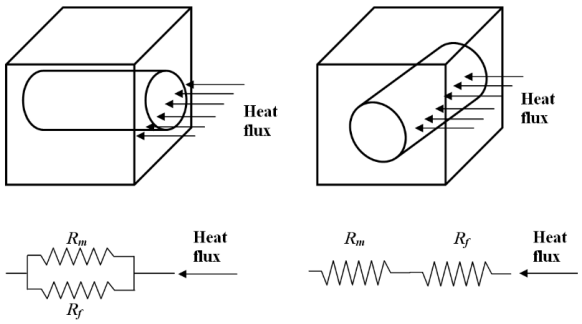

Figure 3.7: Thermal resistance model used to estimate thermal conductivity of FRP in axial and transverse direction (Pan & Hocheng, 1996)

3.6.2 Geometric Model and FE Mesh

A three-dimensional finite element model was developed to simulate laser cutting process for carbon/Kevlar fiber-reinforced hybrid composite. Figure 3.8a shows that the composite was modelled as twill weaved pattern and each fiber type can been distinguished by different colours. The overall shape of the model is a rectangle with dimensions 12×8 mm^2 of 0.3 mm thick. The model was restricted to a small portion of the actual workpiece because of hardware limitation (laptop with quad core CPU at 2.8 GHz and 12 GB RAM). The FE model consists of elements with (in total) 592,245 nodes and 471,040 elements. A relatively denser mesh was used in the cutting region to improve accuracy of the kerf width and resolve steep temperature gradients around the heating zone. A compromise between computing time and accuracy resulted in the final mesh as shown in Figure 3.8b. The composite was discretized into three different sections where each section has different element size as illustrated in Figure 3.8b: (i): 20 µm×20 µm×75 µm, (ii): 50 µm×20 µm×75 µm and (iii): 500 µm×20 µm×75 µm. Figure 3.8c depicts mesh configuration at regions (i) and (ii). The selected element types for thermal heat transfer analysis and stress analysis are the eight-node linear convection/diffusion elements (DCC3D8) and the eight-node quadrilateral continuum shell (SC8R with reduced integration), respectively. As illustrated in Figure 3.9, the bottom and top faces consist of corner nodes 1, 2, 3, 4 and corner nodes 5, 6, 7, 8, respectively. The stacking direction and thickness direction have been defined to be in the direction from the bottom to the top face.

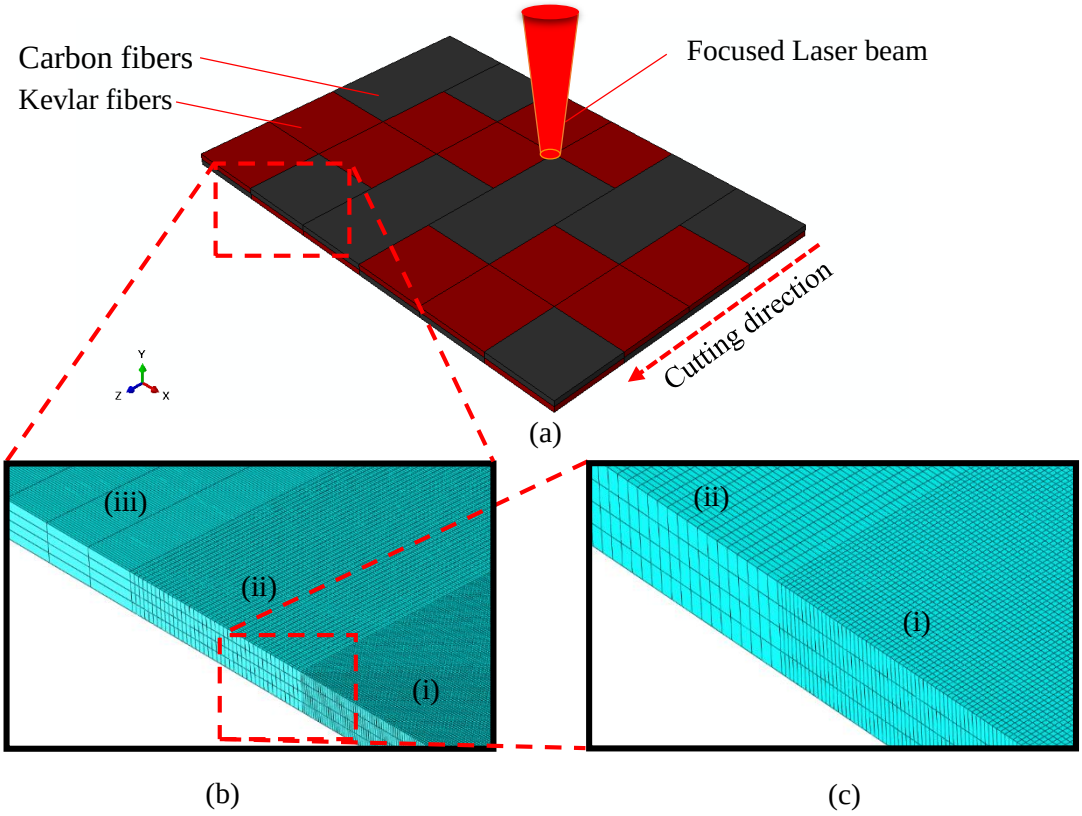

Figure 3.8: (a) The schematic view of carbon/Kevlar hybrid composite and laser position; (b) the mesh distribution perpendicular to cutting direction; (c) magnified image of denser mesh near cutting area

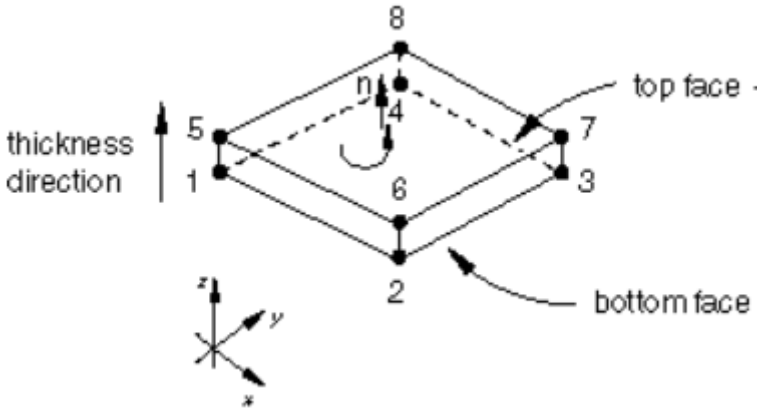

Figure 3.9: Normal and thickness direction for continuum shell element (SC8R) (Abaqus, 2014)

3.6.3 Finite Element Analysis

An uncoupled thermo-mechanical analysis approach was employed for finite element analysis. Firstly, the thermal analysis was performed independently in order to adjust the heat source parameters, incorporating thermal boundary conditions including convection and radiation. Temperature histories calculated during thermal analysis were then used as a predefined field for mechanical analysis. Then, mechanical boundary conditions and loadings were applied during mechanical analysis. Thereafter, thermal stress analysis was performed involving a nonlinear transient thermal analysis followed by a stress analysis. Since the simulation consists of non-linear material behaviour, it is mandatory to choose a non-linear explicit analysis to obtain converged results.

3.6.3.1 Thermal Analysis

The thermal analysis was carried out using temperature-dependent material properties. The developed model is based on the conventional heat diffusion equation with a heat source, a CO_2 laser with Gaussian temporal and spatial profiles. The laser heating process is involved with the transient situation during the cutting process (Negarestani et al., 2010). The governing partial differential equation for the transient heat conduction is:

$$\rho \frac{dC_p T_i}{dt} = \nabla(K \nabla T) + Q - Q_v \qquad \text{Equation 3.8}$$

where ρ is the density of the material (kg/m^3), K is the thermal conductivity (W/m˚K), C_p is the specific heat capacity (J/kg ˚K), T_i is the temperature (˚K), t is time variable (s), Q is the heat source and Q_v is the heat loss due to heat convection. At the surface of composite, convectional heat transfer and radiant heat transfer are responsible for the heat loss, considering other free surfaces to be adiabatic. The heat loss, Q_v can be formulated using:

$$Q_v = h_c(T_s - T_0) + \varepsilon_{em}\sigma_{SBc}(T_s^4 - T_0^4)$$ Equation 3.9

where h_c is the convection factor, ε_{em} is the emissivity, σ_{SBc} is the Stefan-Boltzmann constant, T_s and T_0 are respectively the surface and the initial temperatures. The predefined values of these constants are $h_c = 30$, $\varepsilon_{em} = 0.05$ and $\sigma_{SBc} = 5.67\times10^{-8}$. The adiabatic surfaces follow:

$$\nabla(K\nabla T) = 0$$ Equation 3.10

The laser beam and its heat distribution in the cutting direction was modelled as a 3D moving heat source in the form of a Gaussian beam intensity distribution, Q which can be expressed as (Goldak et al., 1984; Sheng & Joshi, 1995):

$$Q = \frac{aP}{\pi R^2} exp(-\frac{-(Vt - Z_0)^2 + x^2}{R^2})$$ Equation 3.11

where a is the absorptivity, P is the beam power, R is the beam radius, Z_0 is the initial beam position and V is the beam velocity. The cumulative beam energy at a given point (x,z) is the time integral of the beam intensity. Laser heat flux of 37.6 W with a prescribed velocity of 25 mm/s along the z-axis and multi-pass technique through user subroutine DFLUX is applied to the thermal model.

3.6.3.2 Stress Analysis

In stress analysis, the history of altered temperature derived from the thermal analysis was entered into the stress analysis as a thermal loading. The temperature data was transferred to the elements used for the stress analysis through the connectivity matrix. This provides less computational time for the converged results. Thermal stresses and strains were then calculated at each time increment, giving final state of residual stresses. The fixed boundary conditions were applied on both the ends of the workpiece resembling the earlier

experimental work. The same meshing size from thermal analysis was imported to stress analysis to facilitate compatibility and convergence of nodal data mapping during the stress analysis.

An equivalently significant assumption in the development of the mechanics of fiber-reinforced composites is the plane-stress assumption (Hyer & White, 2009). Following the plane-stress assumption, components σ_3, τ_{23} and τ_{13} are set to zero which leads to a relation involving only σ_1, σ_2, τ_{12} and ε_1, ε_2, γ_{12}, such that:

$$\begin{Bmatrix}\sigma_1\\ \sigma_2\\ \tau_{12}\end{Bmatrix}=\begin{bmatrix}\frac{E_1}{1-\nu_{12}\nu_{21}} & \frac{\nu_{21}E_1}{1-\nu_{12}\nu_{21}} & 0\\ \frac{\upsilon_{21}E_1}{1-\nu_{12}\nu_{21}} & \frac{E_2}{1-\nu_{12}\nu_{21}} & 0\\ 0 & 0 & G_{12}\end{bmatrix}\begin{Bmatrix}\varepsilon_1\\ \varepsilon_2\\ \gamma_{12}\end{Bmatrix} \qquad \text{Equation 3.12}$$

where σ_1, σ_2, τ_{12} are components of the stress tensor, ε_1, ε_2, γ_{12} are components of strain tensor, E_1 and E_2 are elastic moduli in longitudinal and transverse direction, ν is the Poisson ratio and G_{12} is the shear modulus. When a fiber-reinforced composite material is heated or cooled, the material expands or contracts. This is a deformation that takes place independently of any applied load. If the temperature as an external load is changed by an amount of ΔT at different instants, the stresses caused by the temperature change are:

$$\begin{Bmatrix}\sigma_1\\ \sigma_2\\ \tau_{12}\end{Bmatrix}=\begin{bmatrix}\frac{E_1}{1-\nu_{12}\nu_{21}} & \frac{\nu_{21}E_2}{1-\nu_{12}\nu_{21}} & 0\\ \frac{\nu_{21}E_1}{1-\nu_{12}\nu_{21}} & \frac{E_2}{1-\nu_{12}\nu_{21}} & 0\\ 0 & 0 & G_{12}\end{bmatrix}\begin{Bmatrix}\varepsilon_1-\alpha_1\Delta T\\ \varepsilon_2-\alpha_2\Delta T\\ \gamma_{12}\end{Bmatrix} \qquad \text{Equation 3.13}$$

where α is thermal expansion and ΔT is the temperature difference. It is noted that elastic modulus and ultimate strength are temperature-dependent parameters, which can be used as input parameters for characterizing FRP damage at various operating temperatures as follow (Mivehchi & Varvani-Farahani, 2010):

$$E(T) = E(T_0)\left[1-\frac{\left(\frac{E(0)}{E(T_0)}-1\right)}{ln\,(1-\frac{T_0}{T_m})}\,ln\,(\frac{\left(1-\frac{T}{T_m}\right)}{\left(1-\frac{T_0}{T_m}\right)})\right] \quad \text{Equation 3.14}$$

$$\sigma_{ult}(T)=\sigma_{ult}(T_0)\left[1-\frac{\left(\frac{\sigma_{ult}(0)}{\sigma_{ult}(T_0)}-1\right)}{ln\,(1-\frac{T_0}{T_M})}\,ln\,(\frac{\left(1-\frac{T}{T_M}\right)}{(1-\frac{T_0}{T_M})})\right] \quad \text{Equation 3.15}$$

where $E(T)$ and $\sigma_{ult}(T)$ are the elastic modulus and the ultimate strength at an arbitrary temperature, respectively. $E(T_0)$ and $\sigma_{ult}(T_0)$ are the elastic modulus and the ultimate strength at ambient temperature, respectively. $E(0)$ and $\sigma_{ult}(0)$ are the elastic modulus and the ultimate strength at absolute zero temperature (0˚K= -273˚C). T_m indicates the fiber melting temperature of the composite. T, T_m and T_0 are all in Kelvin. Based on Equation 3.13 to Equation 3.15, the increase of temperature leads to residual thermal stresses and mechanical degradation in both strength and stiffness of the composite.

After obtaining transient temperature field of the composite laminate, element deletion on the basis of temperature history and Hashin-damage criteria (Hashin, 1980) were employed in stress analysis. The fundamental failure modes of Hashin-damage criteria are essentially temperature dependent on both elastic moduli and strength. As the temperature increases, the composite strength starts to decay due to stiffness degradation and interlaminar cracks occurring in the temperature affected area (Kim et al., 1999), accelerating damage initiation in both fibers and matrix. At this juncture, any element which meets all the predefined damage criteria at sufficiently high temperature will start losing its strength. When exposed to laser beam, these elements will be ablated and removed. In this way, prediction of kerf width and HAZ can be implemented and then used to characterize damage in fibers and matrix.

Element deletion in a mesh can be controlled during the course of an Abaqus analysis through subroutine VUMAT (Abaqus, 2014). There are four different initiation failure modes considered in Hashin criteria: fiber tension (Equation 3.16), fiber compression (Equation 3.17), matrix tension (Equation 3.18) and matrix compression (Equation 3.19).

Fiber tension ($\sigma_1 \geq 0$):

$$\left(\frac{\sigma_1}{X^T_{(temp)}}\right)^2 + \beta\left(\frac{\tau_{12}}{S^L_{(temp)}}\right)^2 = \begin{cases} \geq 1 & Failure \\ < 1 & No\ failure \end{cases} \quad \text{Equation 3.16}$$

Fiber compression ($\sigma_1 < 0$):

$$\left(\frac{\sigma_1}{X^C_{(temp)}}\right)^2 = \begin{cases} \geq 1 & Failure \\ < 1 & No\ failure \end{cases} \quad \text{Equation 3.17}$$

Matrix tension ($\sigma_2 \geq 0$):

$$\left(\frac{\sigma_2}{Y^T_{(temp)}}\right)^2 + \left(\frac{\tau_{12}}{S^L_{(temp)}}\right)^2 = \begin{cases} \geq 1 & Failure \\ < 1 & No\ failure \end{cases} \quad \text{Equation 3.18}$$

Matrix compression ($\sigma_2 < 0$):

$$\left(\frac{\sigma_2}{2S^T_{(temp)}}\right)^2 + \left[\left(\frac{Y^C_{(temp)}}{2S^T_{(temp)}}\right)^2 - 1\right]\frac{\sigma_2}{Y^C_{(temp)}} + \left(\frac{\tau_{12}}{S^L_{(temp)}}\right)^2 = \begin{cases} \geq 1 & Failure \\ < 1 & No\ failure \end{cases} \quad \text{Equation 3.19}$$

where X^T is the longitudinal tensile strength, X^C is the longitudinal compressive strength, Y^T is the transverse tensile strength, Y^C is the transverse compressive strength, S^L is the longitudinal shear strength, S^T is the transverse shear strength and β is the coefficient that determines the contribution of the shear stress to the fiber tensile initiation criterion. It is noteworthy that all the input strength variables are temperature dependent (Equation 3.15). A value of 1 or higher (Equation 3.16 to Equation 3.19) indicates that the damage initiation

criterion has been met. After damage is initiated, the stiffness matrix of the plane stress changes and the corresponding stresses of the composite can be computed by Equation 3.20.

$$\begin{Bmatrix}\sigma_1\\ \sigma_2\\ \tau_{12}\end{Bmatrix}=\frac{1}{D}\begin{bmatrix}(1-d_f)E_1 & (1-d_f)(1-d_m)v_{21}E_1 & 0\\ (1-d_f)(1-d_m)v_{12}E_2 & (1-d_m)E_2 & 0\\ 0 & 0 & (1-d_s)GD\end{bmatrix}\begin{Bmatrix}\varepsilon_1-\alpha_1\Delta T\\ \varepsilon_2-\alpha_2\Delta T\\ \gamma_{12}\end{Bmatrix} \quad \text{Equation 3.20}$$

where $D=1-(1-d_f)(1-d_m)v_{12}v_{21}$, d_f is the current state of fiber damage, d_m is the current state of epoxy matrix damage and d_s is the current state of shear damage. The parameter damage, d represents the catastrophic failure of carbon and Kevlar fibers with values in the range of ($0 \leq d \leq 1$). When d attains d_{max} (equals to 1), the element loses 100% of residual stiffness and fails completely with no bearing capacity, causing the affected element to be removed. The procedure employed to predict residual stress, HAZ and kerf width is shown in Figure 3.10.

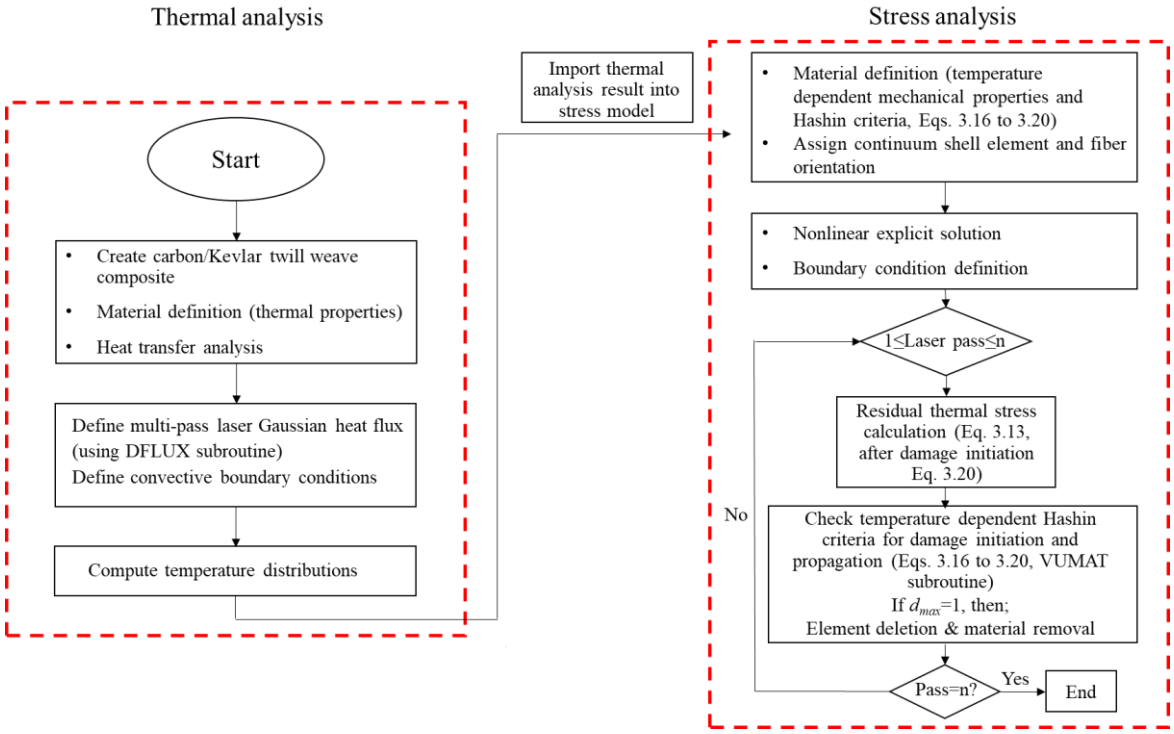

Figure 3.10: Analysis procedure for the modelling in Abaqus

CHAPTER 4

RESULTS AND DISCUSSION

4.1 Introduction

Laser cutting of carbon/Kevlar hybrid composite was carried out. In the following section, experimental and numerical results are presented.

4.2 Experimental Results

After designing and running the experiments, the responses were recorded. The analysis of variance (ANOVA) method statistically measures the effect of input variables on the response variables. The measured characteristics of kerf and HAZ are shown in Table 4.1. To check the appropriateness of different regions of the carbon/Kevlar composite sample, three experiments (setting parameters at No. 1) were performed at specified regions and it was found out that the errors between the output results are less than 5% (Appendix 2). Thereafter, rest of the experiments were done in one run in the same selected region of carbon/Kevlar composite at specified distance. Furthermore, three measurements of HAZs, kerf characteristics, their mean values and the standard deviation are shown in Appendix 3. It is noteworthy to mention that all experiments were performed at different time frameworks, and it was given 60 seconds for the CO_2 laser tube to become cool. As it is seen in Table 4.1, the run order of experiments was set based on center point to check whether the laser was calibrated after 6 runs. It was found out that the results of two sets of experiments at center point (run order number 7 and number 8) have less than 10% error, which is acceptable based on other researchers findings (Cui et al., 2016; Kotlyar et al., 2019). This was used as a method whether laser system was calibrated and after checking the alignment of reflecting mirrors, the rest of the experiments were conducted.

Table 4.1: Design of experiment and responses

Experimental input parameter					Response			
No. Standard order	No. Run order	Laser Power (W)	Cutting Speed (mm/s)	Standoff Distance (mm)	Top kerf width, T_k (mm)	Bottom kerf width, B_k (mm)	Kerf ratio (T_k/B_k)	HAZ (mm)
1	1	36	15	50.8	0.758	0.754	1.005	0.662
2	2	40	15	50.8	0.814	0.813	1.002	0.690
3	3	36	25	50.8	0.676	0.653	1.035	0.451
4	4	40	25	50.8	0.690	0.686	1.005	0.515
5	5	36	20	49.8	0.817	0.767	1.066	0.499
6	6	40	20	49.8	0.889	0.821	1.083	0.661
7	9	36	20	51.8	0.951	0.940	1.012	0.664
8	10	40	20	51.8	0.973	0.998	0.974	0.752
9	11	38	15	49.8	1.017	0.977	1.041	0.721
10	12	38	25	49.8	0.698	0.611	1.142	0.554
11	13	38	15	51.8	1.011	1.044	0.969	0.818
12	14	38	25	51.8	0.693	0.713	0.972	0.428
13	7	38	20	50.8	0.753	0.765	0.984	0.574
14	8	38	20	50.8	0.694	0.692	1.003	0.570
15	15	38	20	50.8	0.718	0.749	0.959	0.590

4.2.1 Heat Affected Zone (HAZ)

The ANOVA results of the HAZ is shown in Table 4.2. It reveals that cutting speed parameter has statistically effect on the HAZ at the 95% confidence level. On the other hand, the presence of the laser power factor and SOD do not significantly affect the HAZ of the samples.

Table 4.2: ANOVA results for HAZ

Source	DF	Adj SS	Adj MS	*F*-Value	*p*-Value	
Power	1	0.014697	0.014697	4.3	0.093	
Speed	1	0.111435	0.111435	32.59	0.002	significant
SOD	1	0.006361	0.006361	1.86	0.231	
Power*Power	1	0.000213	0.000213	0.06	0.813	
Speed*Speed	1	0.000142	0.000142	0.04	0.847	
SOD*SOD	1	0.012708	0.012708	3.72	0.112	
Power*Speed	1	0.000315	0.000315	0.09	0.774	
Power*SOD	1	0.001374	0.001374	0.4	0.554	
Speed*SOD	1	0.012401	0.012401	3.63	0.115	
Error	5	0.017095	0.003419			
Total	14	0.176869				

The response surface plots of HAZ with respect to variation in input parameters are shown in Figure 4.1. It can be observed the HAZ increases with the increase of laser power and decrease of cutting speed (Figure 4.1a). In both cases, considerable increase in HAZ were reported due to increased absorption of thermal energy and longer laser-material exposure. In contrast, higher cutting speed with reduced exposure time lead to narrow HAZ which agrees with (Leone & Genna, 2018; Li et al., 2019; Rao et al., 2017). By referring to Figure 4.1b and Figure 4.1c, the minimum HAZ can be observed when SOD is equivalent to focal length (50.8 mm) i.e., the smallest beam spot. It should be noted that with the increase of laser power, the HAZ is more pronounced at 51.8 mm SOD as compared to 49.8 mm SOD.

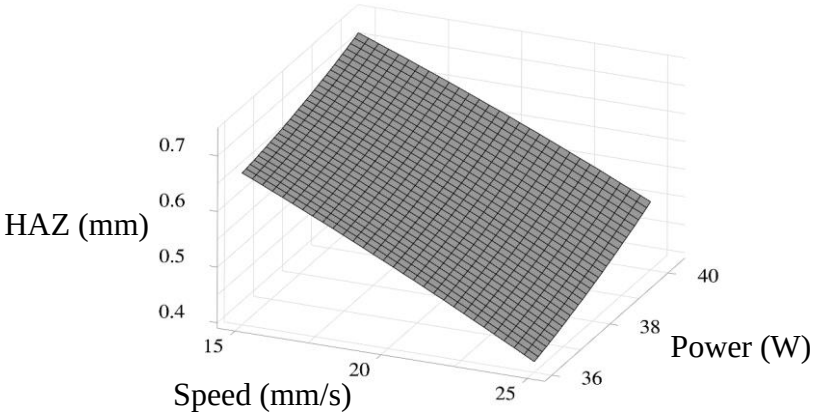

(a)

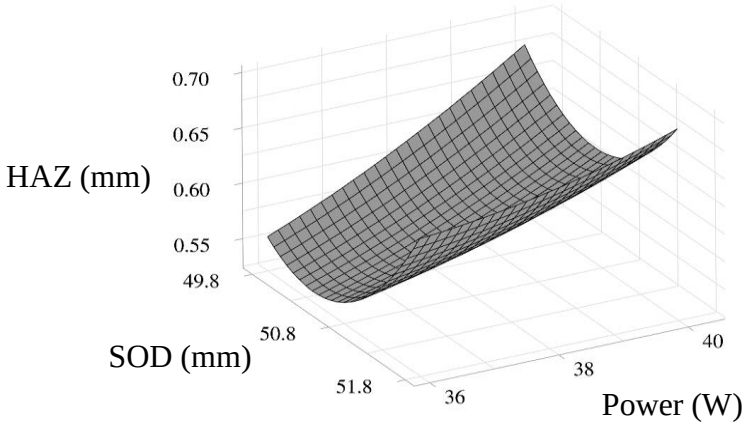

(b)

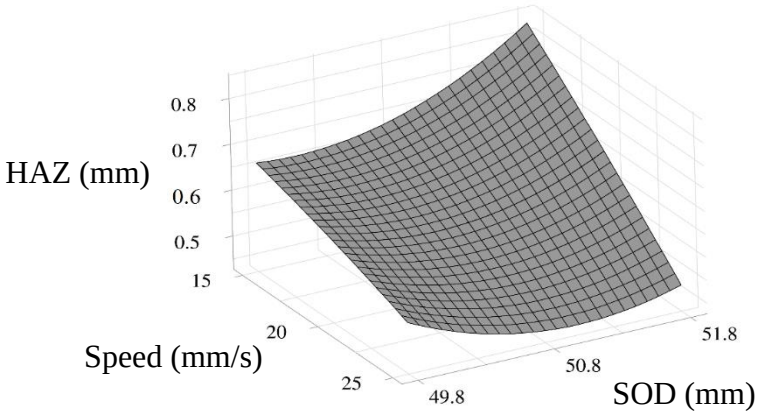

(c)

Figure 4.1: Response surface plots of HAZ with respect to different combinations of the input process parameters, (a) laser power - cutting speed; (b) laser power – SOD; (c) cutting speed – SOD

As shown in Figure 4.2a, the HAZ of Kevlar fibers can be divided into two distinguishable regions. HAZ (I) shows the side effect of thermal loading on the region adjacent to kerf, sufficiently enough to cause epoxy layer to melt and leaving epoxy residues upon re-solidification on the surface of exposed Kevlar fibers (Figure 4.2d). Similarly, in the neighbouring region of HAZ (II), there is no longer layer of epoxy exists indicating its complete vaporization (Leone & Genna, 2018). Due to significantly low thermal decomposition of matrix (epoxy) as compared to both fibers, the former is readily decomposed and vaporized. The HAZ (II) also shows charring (Figure 4.2b) and swelling of Kevlar fibers (Figure 4.2c) which are not observed on carbon fibers. This is because the thermal conductivity of carbon fiber is about 120 times higher than Kevlar fiber, which further accelerates decomposition and burning of the latter. As shown Figure 4.2d, Kevlar fibers are completely burned in HAZ (II) region which makes it so brittle, resulting in noticeable separation from HAZ (I) region. It is noted that HAZ is an important quality indicator of the cut region using lasers. Based on findings (Li et al., 2020; Raza et al., 2019; Solati et al., 2019), high power lasers produce an extended HAZ which results in the damage width of burnt area and decreases the strength of composites on the top surface of the cut region. It has been discovered that the value of HAZ increases to 1 mm by using lasers more than 500 W (El-Hofy & El-Hofy, 2019). Whereas, based on the achieved results of low power CO_2 laser, it is seen that defected area in Kevlar and carbon fibers shows HAZ value less than 0.7 mm.

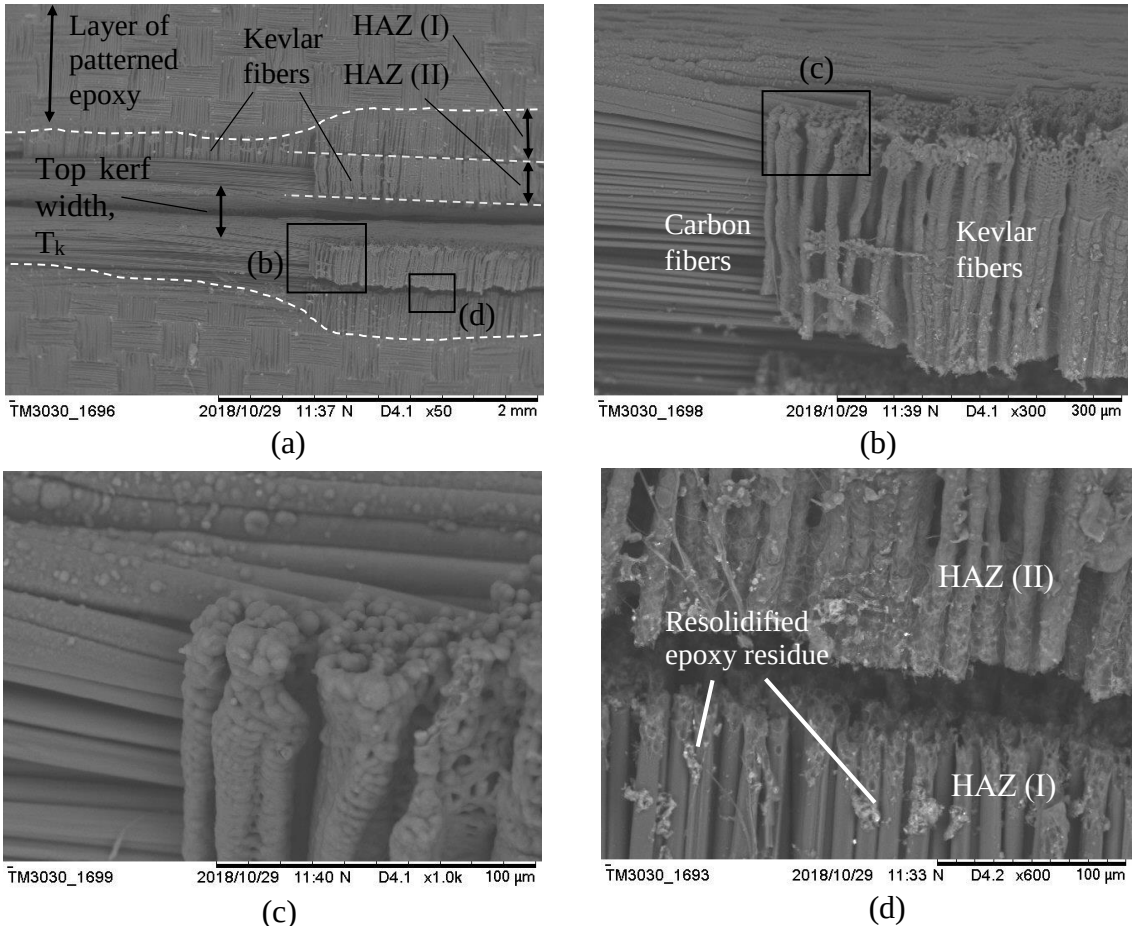

Figure 4.2: SEM micrographs of HAZ (experiment no. 4), (a) two dissimilar regions of heat affected zones; (b) completely burnt and separated Kevlar fibers; (c) swelling of burnt Kevlar fibers; (d) crack due to the brittle feature of charred Kevlar fibers

4.2.2 Kerf Characteristics

The ANOVA results of the average kerf widths (T_k and B_k) developed in the laser cutting process are shown in Tables 4.3 and 4.4. Results reveal that cutting speed and quadratic term of SOD have statistically effect on the kerfs at the 95% confidence level.

Table 4.3: ANOVA results for the Top Kerf (T_k)

Source	DF	Adj SS	Adj MS	*F*-Value	*p*-Value	
Power	1	0.003311	0.003311	0.53	0.501	
Speed	1	0.08908	0.08908	14.13	0.013	significant
SOD	1	0.005325	0.005325	0.84	0.4	
Power*Power	1	0.004015	0.004015	0.64	0.461	
Speed*Speed	1	0.001456	0.001456	0.23	0.651	
SOD*SOD	1	0.086718	0.086718	13.75	0.014	significant
Power*Speed	1	0.000459	0.000459	0.07	0.798	
Power*SOD	1	0.000637	0.000637	0.1	0.764	
Speed*SOD	1	0	0	0	1	
Error	5	0.03153	0.006306			
Total	14	0.222833				

Table 4.4: ANOVA results for the Bottom Kerf (B_k)

Source	DF	Adj SS	Adj MS	*F*-Value	*p*-Value	
Power	1	0.00515	0.00515	0.74	0.428	
Speed	1	0.106731	0.106731	15.44	0.011	significant
SOD	1	0.033747	0.033747	4.88	0.078	
Power*Power	1	0.001274	0.001274	0.18	0.686	
Speed*Speed	1	0.002673	0.002673	0.39	0.561	
SOD*SOD	1	0.060571	0.060571	8.76	0.032	significant
Power*Speed	1	0.000164	0.000164	0.02	0.884	
Power*SOD	1	0.000005	0.000005	0	0.98	
Speed*SOD	1	0.000305	0.000305	0.04	0.842	
Error	5	0.034567	0.006913			
Total	14	0.24674				

Figure 4.3 and Figure 4.4 show response surface plots that demonstrate the relationship between different laser processing parameters and the kerf widths. It is observed that both top and bottom kerf widths decrease significantly with the increase of cutting speed. The increment of cutting speed enhances the cooling effect of the composite and reduces the temperature in inner layers. It leads to less penetration of laser beam and reduction of material removal from the top and bottom surface of the composite. In contrast, it is evident that reduction in cutting speed results in increase of both kerf widths and consequently matrix recession (Figure 5.2d). This agrees with the finding reported in (Gautam & Mishra, 2019a; Negarestani & Li, 2013). Different thermal conductivity and decomposition temperature of fibers and epoxy matrix enforce a non-uniform heat propagation mechanism along the kerf depth despite the constant energy per unit length ratio. This emphasizes the influence of anisotropic characteristics of the material.

In contrast, an increase of laser power produces a first slightly decrease of top kerf width followed by a steep increase (Raza et al., 2019), as shown in Figure 4.3a. For bottom kerf width, it remains almost constant up to 38 W and afterwards increases at the increase of power up to 40 W (Figure 4.4a). By the increase of laser power, the material absorbs more thermal energy emitting from incident laser beam that leads to more evaporation of material resulting wider kerf width. These aspects are in agreement with what reported in (Gautam & Mishra, 2019b; Leone et al., 2014; Marimuthu et al., 2019).

The effect of SOD is significantly obvious on both top and bottom kerfs (Figure 4.3b, Figure 4.3c, Figure 4.4b and Figure 4.4c). This was discussed previously by other researchers (Masoud et al., 2020; Mishra et al., 2020). As SOD is equivalent to focal length (50.8 mm), both top and bottom kerfs indicate lowest amounts. Here, the focused laser beam

forms a high energy column of heat which enter the material and results in vaporization and burning of matrix and fibers. By increase or decrease of SOD, the size of the beam spot would vary proportionally (Figure 3.4).

The change of SOD away from focal position leads to bigger HAZ and kerf widths. It is noted that both top and bottom kerf widths are relatively smaller for 49.8 mm SOD as compared to 51.8 mm SOD.

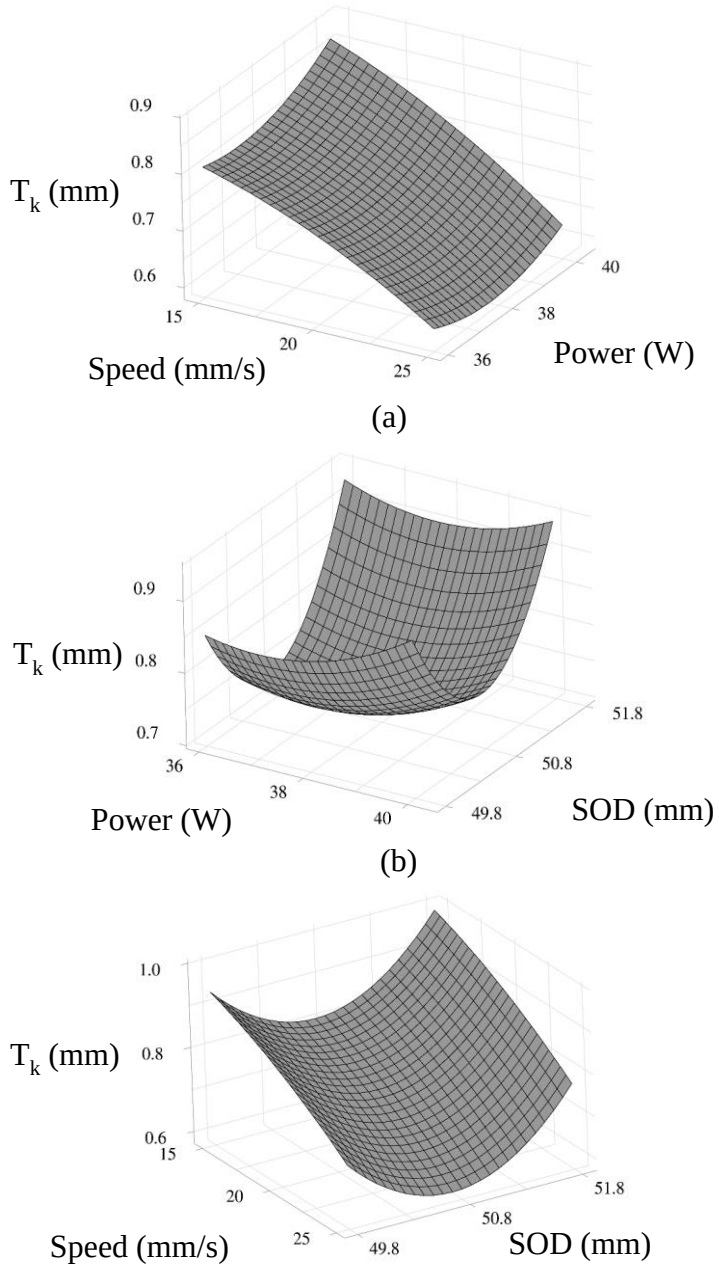

Figure 4.3: Response surface plots of top kerf width with respect to different combinations of the input process parameters, (a) power - speed; b) power - SOD; (c) speed – SOD

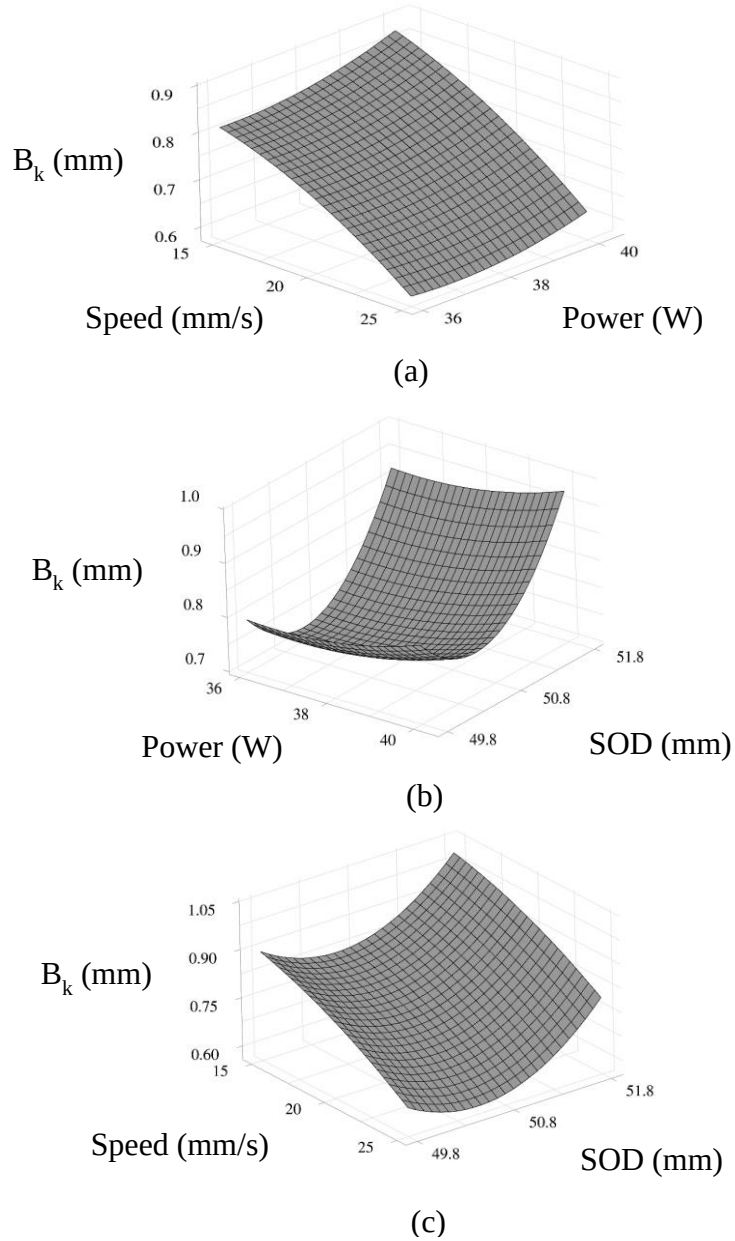

Figure 4.4: Response surface plots of bottom kerf width with respect to different combinations of the input process parameters, (a) power - speed; (b) power - SOD; (c) speed – SOD

The deviation of the cut surface from the desired surface can be expressed in terms of kerf ratio. This parameter defines the geometrical accuracy of the machined workpiece. The closer kerf ratio to 1, the more perpendicular the cut surface to the plane surface of the

composite. Nevertheless, the workpiece will have to be machined afterwards to remove the unwanted taper if the kerf ratio is significantly lower or higher than 1. Table 4.5 shows the ANOVA data for the kerf ratio. It indicates SOD and quadratic term of SOD has dominant effect on kerf ratio due to *p*-value less than 0.05.

Table 4.5: ANOVA results for the Kerf Ratio ($\frac{T_k}{B_k}$)

Source	DF	Adj SS	Adj MS	*F*-value	*p*-value	
Power	1	0.000348	0.000348	0.72	0.434	
Speed	1	0.002344	0.002344	4.86	0.079	
SOD	1	0.020594	0.020594	42.68	0.001	significant
Power*Power	1	0.000964	0.000964	2	0.217	
Speed*Speed	1	0.00067	0.00067	1.39	0.292	
SOD*SOD	1	0.004648	0.004648	9.63	0.027	significant
Power*Speed	1	0.000182	0.000182	0.38	0.566	
Power*SOD	1	0.000763	0.000763	1.58	0.264	
Speed*SOD	1	0.002443	0.002443	5.06	0.074	
Error	5	0.002413	0.000483			
Total	14	0.034762				

Figure 4.5 shows response surface plots of kerf ratio with respect to different process parameters. It is clear that when the beam spot was positioned exactly at the focal length (50.8 mm SOD), the kerf ratio is considerably close to 1. This is because the laser beam has maximum energy and it forms a column of high energy resulting in effective burning of material along the optical path of the laser (Genna et al., 2020). Figure 4.6 shows precise and good cut quality of fibers at the focal length.

It is observed for higher cutting speed and lower laser power; kerf ratio deviates higher than 1 (Figure 4.5a). At high cutting speed, the interaction time between laser beam

and top surface of the material reduces, causing less thermal energy penetrates into the material thickness. As a result, the top kerf width is found relatively larger as compared to the bottom. Similarly, when the laser power decreases, less energy is provided which causes bigger kerf on top than bottom.

In addition, defocusing the laser beam causes the kerf ratio to deviate from 1. As depicted in Figure 4.5b and Figure 4.5c, it is found the kerf ratio increases with the decrease of SOD. For the SOD positioned at 49.8 mm, it is reported that the kerf ratio is higher than 1. This is because the beam intensity reduces through the thickness of the material due to anisotropic absorption and reflection of fibers and epoxy matrix (Dumbhare et al., 2018). The reduced beam intensity causes less fibers and epoxy decomposition at the bottom surface as compared to the top surface.

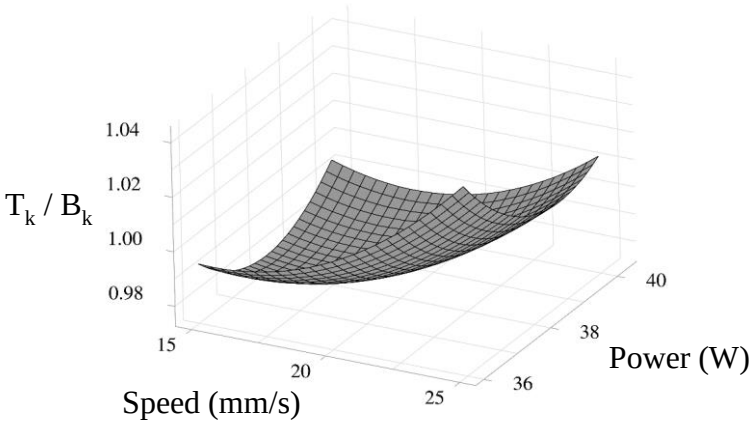

(a)

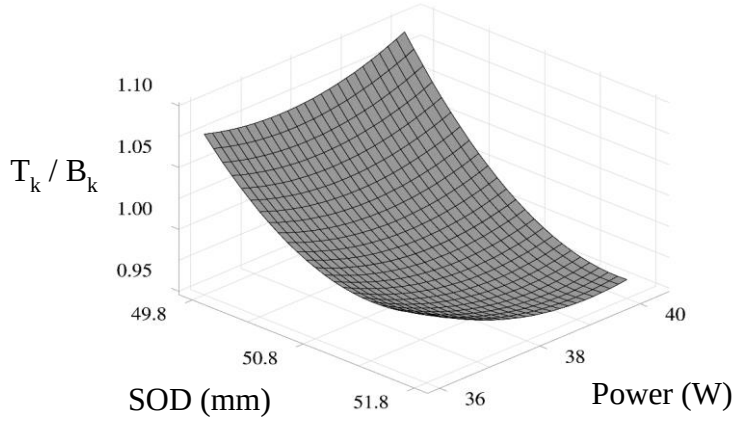

(b)

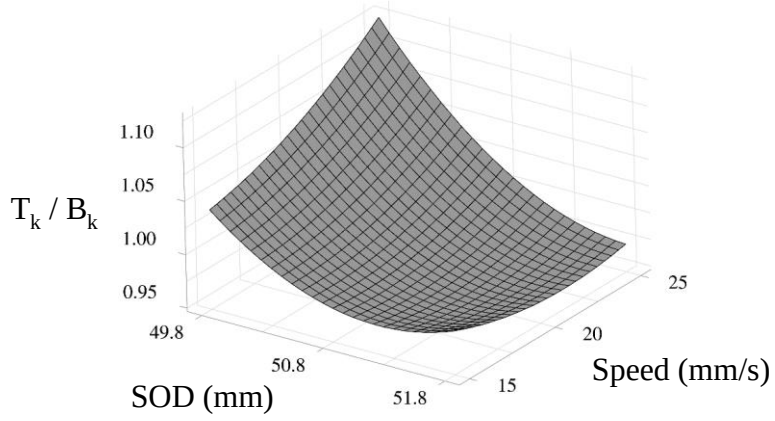

(c)

Figure 4.5: Response surface plots of kerf ratio with respect to different combinations of the input process parameters, (a) power – speed; (b) power – SOD; (c) speed - SOD

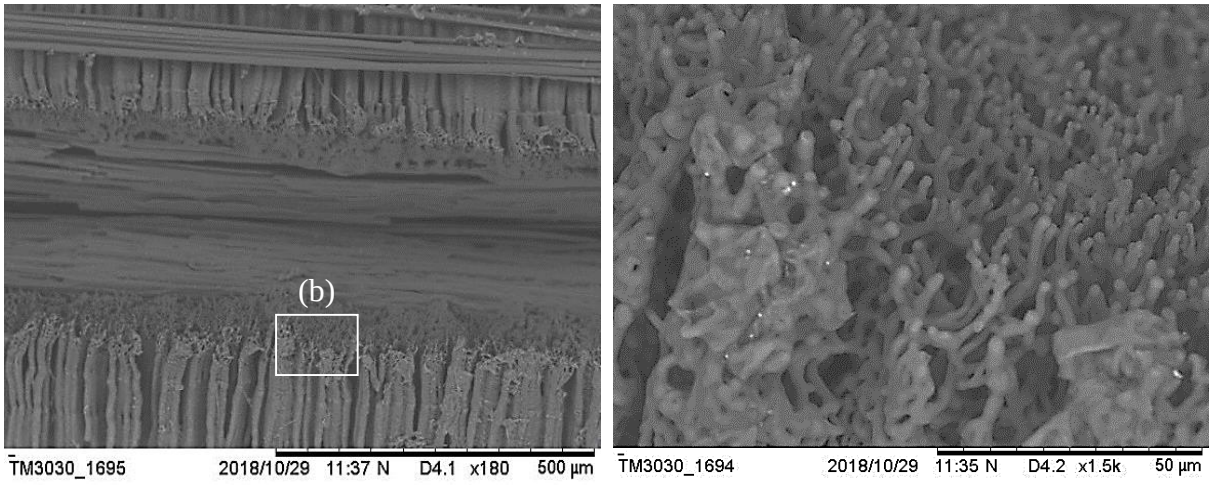

(a) (b)

Figure 4.6: SEM micrographs of, (a) cutting area at 50.8 mm SOD; (b) enlarged Kevlar fibers. Sample of experiment standard no. 3

4.2.3 Fiber Pullout

The effect of SODs on fiber pullouts are shown in Figure 4.7. Generally, as the SOD is moved upward or downward from focal position, the area influenced by the laser beam is bigger. Hence, the thermal damage at the beam entrance becomes larger which varies with respect to beam spot size. This effectively leads to temperature rise of fibers and matrix in the entrance region where the combustion temperature is the major process for mass removal from the kerf during the cutting, as previously discussed by (Li et al., 2019; Ming et al., 2018). Since epoxy has lower combustion temperature than the fibers, the former burns for a longer period while the latter remains physically unaffected, resulting in fiber pullout. As shown in Figure 4.7, the amount of fiber pullout for 49.8 mm SOD is lesser than that of 51.8 mm SOD though theoretically they have the same beam spot size on the surface. This can be attributed to the nature of Gaussian beam in which the power density is not evenly distributed across the beam spot (Hecht, 2002). Experimentally, it is evident that 49.8 mm SOD has lower HAZ than that of 51.8 mm SOD (Figure 4.1b).

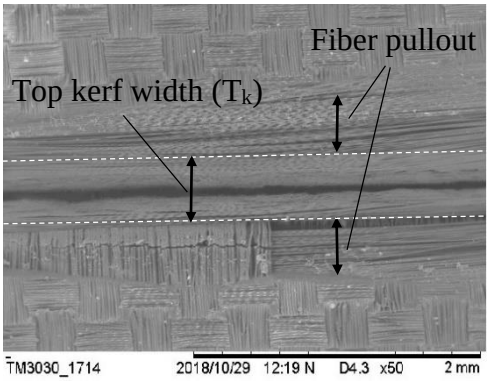

(a)

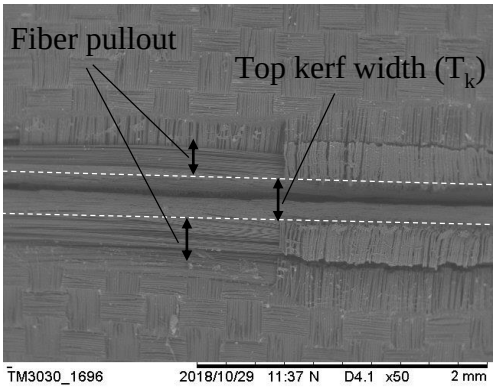

(b)

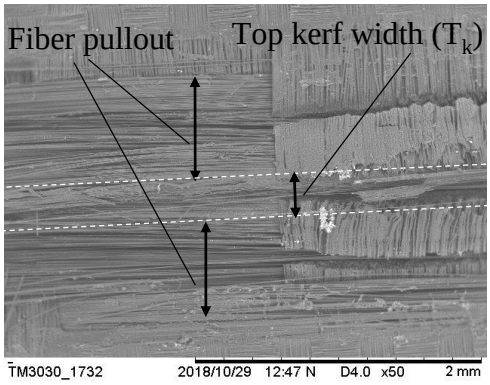

(c)

Figure 4.7: Comparison of extent of fiber pullout for three different SODs, (a) SOD = 49.8 mm (experiment no. 10); (b) SOD= 50.8 mm (experiment no. 3); (c) SOD= 51.8 mm (experiment standard no. 12)

4.2.4 Fiber Orientation

Another essential feature of cutting bidirectional carbon/Kevlar composite is pointed out in Figure 4.8. For better visualization, the boundary of the produced kerfs is marked by the dashed line in Figure 4.8a. In the areas in which the carbon fibers oriented parallel to the cutting direction, one can observe a pronounced local widening of the produced kerf. The kerf size is relatively larger as compared to Kevlar fibers oriented perpendicular to the cutting direction. This agrees well with the finding in (Karataş et al., 2020; Kononenko et al., 2014). The reason is at which the carbon fibers are parallel to the laser direction, some of the incident beam are reflected partially by the cylindrical surfaces of the carbon fibers. This phenomenon leads to scattering and accumulating of heat to the perpendicular direction (Li et al., 2019). Consequently, the anisotropic scattering of the radiation leads to an anisotropic ablation which results in widening kerf width. On the contrary, HAZ extent is much greater and more noticeable in the region of Kevlar fibers (Figure 4.8b). This is clearly shown by the extent of the epoxy vaporized area on the local fiber orientation in bidirectional composite, attributed to lower thermal conductivity of the perpendicular Kevlar fibers as compared to parallel carbon fibers. Therefore, one may observe larger area of burnt Kevlar fibers and vaporized epoxy matrix. Figure 4.8c and Figure 4.8d show examples of burnt Kevlar fibers and resolidified/vaporized epoxy matrix, respectively.

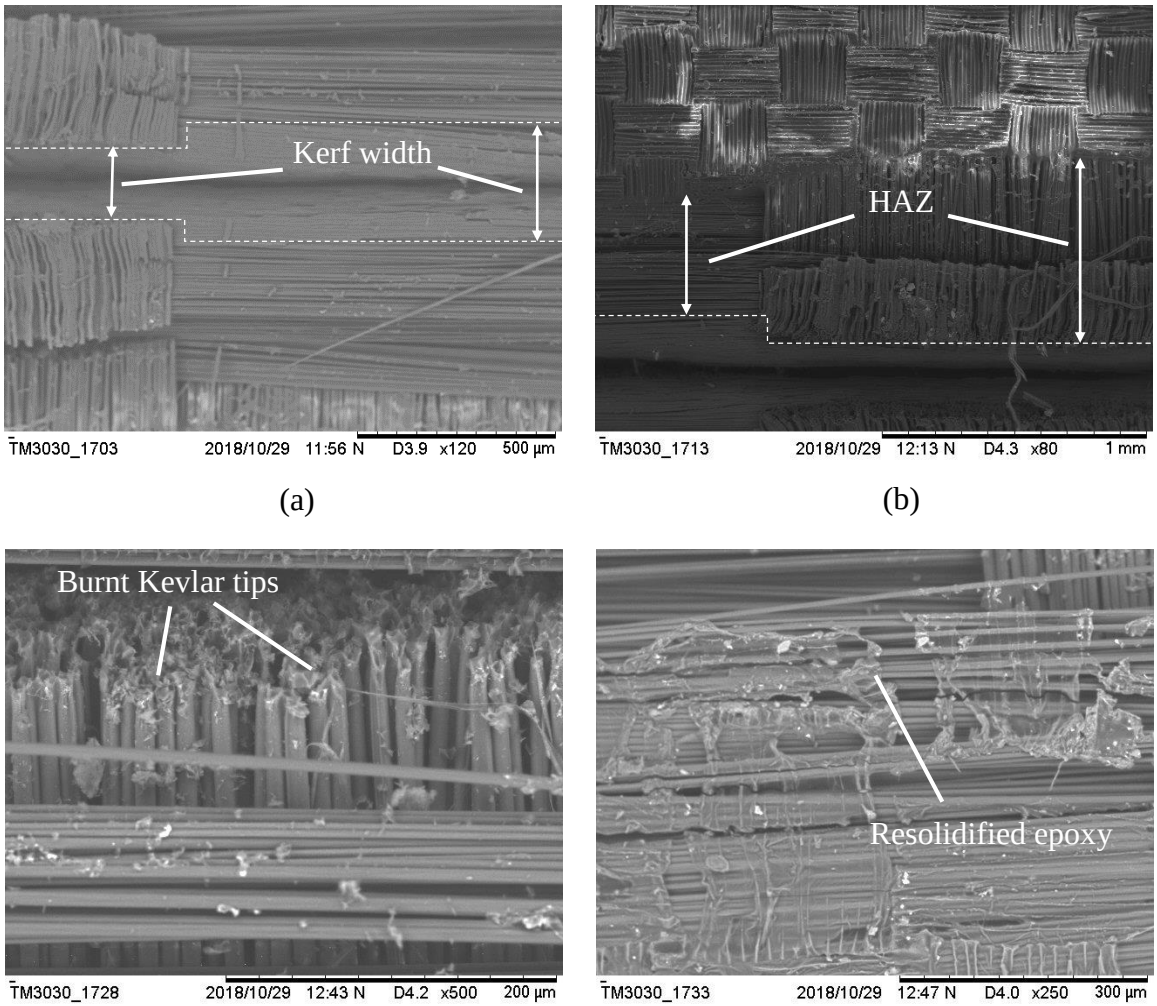

Figure 4.8: The effect of bidirectional fiber orientation on, (a) kerf width; (b) HAZ extent; (c) Kevlar fibers; (d) epoxy matrix. Sample of experiment standard no. 4

4.3 Optimization

The response optimizer option of Minitab statistical software was used here to optimize input parametric combinations. Figure 4.9 shows the calculated optimum input and output parameters based on ANOVA results. The predicted optimum input parameters are 37.6 W, 25 mm/s, and 51.04 mm. Confirmation experiment was carried out to validate the predicted results. Table 4.6 lists the measured output parameters. The errors for HAZ, top

kerf width, bottom kerf width and kerf ratio are found out to be within 0.8%, 9.7%, 2.9% and 6.36%, respectively. This indicates that the produced results are in very close agreement with the predicted results. The main source of error is the inconsistent beam quality which may be affected by water cooling system. The error cannot be verified due to unavailability of the instrument (laser beam profiler).

Figure 4.10 shows less heat affected zone and fiber burnings in the cutting region using the optimum parameters.

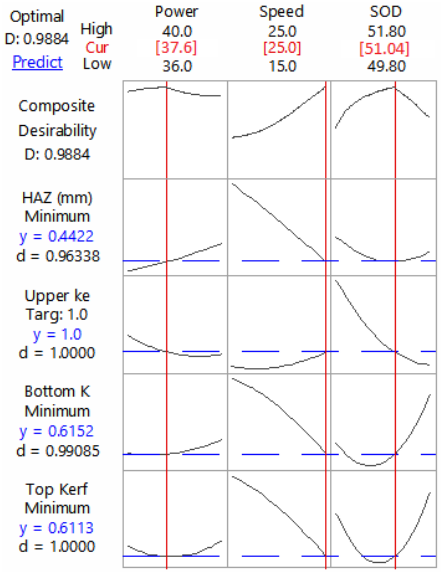

Figure 4.9: Optimum parameters of cutting and the predicted results of HAZ, top kerf width, bottom kerf width and kerf ratio

Table 4.6: Experimental and predicted values of HAZ , top kerf width, bottom kerf width, and kerf ratio at the optimum levels

Parameter	Experimental value	Predicted value	Error
HAZ (mm)	0.446 mm	0.4422 mm	0.8%
Top Kerf Width (mm)	0.6772 mm	0.6113 mm	9.7%
Bottom Kerf Width (mm)	0.6339 mm	0.6152 mm	2.9%
Kerf Ratio	1.068	1	6.36%

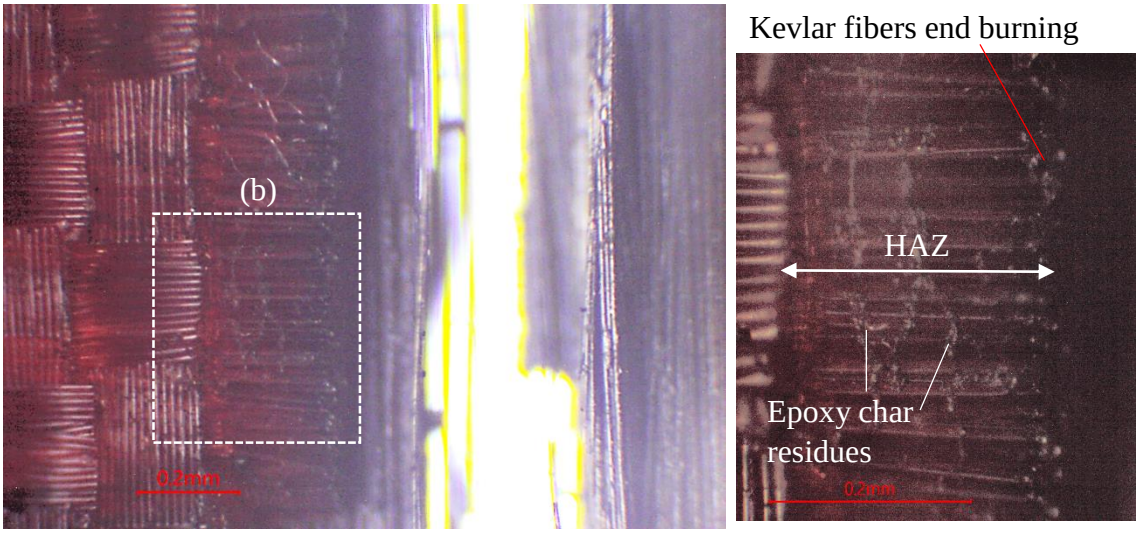

Figure 4.10: (a) The cutting area of optimum laser parameters; (b) less heat affected zone of cutting area and fibers burning

It should be noted all the experiments and following results have been performed by moving the laser beam parallel to the carbon fibers. It was discovered that using the same parameters and number of passes, through cut cannot be obtained when laser beam moves in perpendicular to the carbon fibers. In other words, relatively higher number of passes is required for cutting the composite in that direction. Figure 4.11 shows region of heat affected carbon fibers and melted Kevlar fibers.

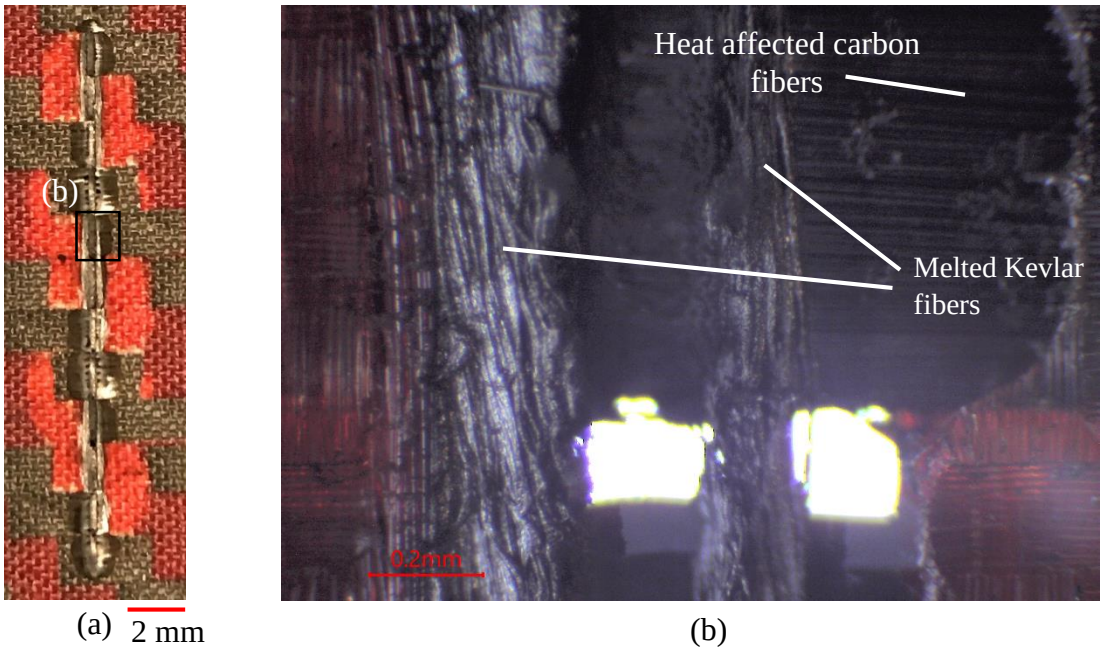

Figure 4.11: (a) Cutting area by moving the laser beam perpendicular to the carbon fibers; (b) remained heat affected carbon fibers and melted Kevlar fibers

4.4 Numerical Results

Temperature and residual stresses are predicted using Abaqus software. For investigation purposes, two paths were defined and also two nodes were selected on Kevlar and carbon side near cutting direction, as shown in Figure 4.12. The coordinates of the specific nodes are listed in Table 4.7 while the location descriptions on the specific paths is listed in Table 4.8.

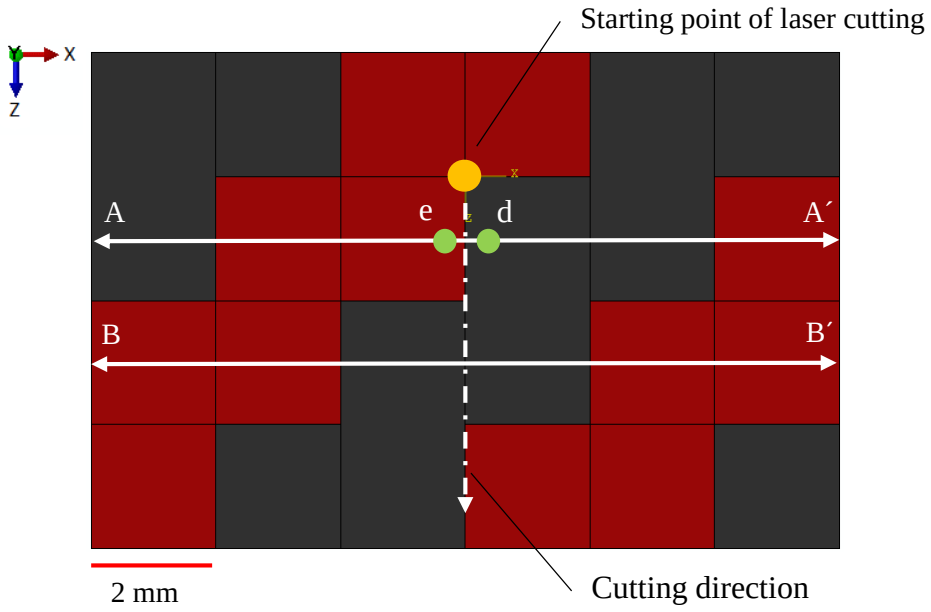

Figure 4.12: Two-dimensional view of composite

Table 4.7: The coordinates of the specific nodes

Node	d	e
X(mm)	2e-5	-2e-5
Y(mm)	0	0
Z(mm)	1	1

Table 4.8: The location descriptions on the specific paths

Path	Equation
A-A´	Z= 1 (y=0)
B-B´	Z= 3 (y=0)

4.4.1 Thermal Analysis

Figure 4.13 shows the nodal temperature gradient for the case of laser parameters. Figure 4.13a shows temperature gradient of the 1st laser pass. The temperature gradient

around the fibers is inhomogeneous for all passes. The reason for this phenomenon can be attributed to different thermal properties of carbon and Kevlar fibers. Thermal conductivity of carbon fibers is approximately 120 times more than Kevlar fibers (Table 3.1). Hence, Kevlar fibers retain more heat as compared to carbon fibers. It can be observed in Figure 4.13b that after the completion of the 2nd pass, the remaining residual temperature from the 1st pass results in a greater temperature distribution. Similarly, the same pattern can be observed after the 3rd pass due to heat accumulation of the preceding passes (Figure 4.13c). The time taken for the completion of each cutting pass is sufficiently long to maintain low temperature value in the initial cutting region as evidently observed on nodal temperature legend (NT11) in Figure 4.13a, Figure 4.13b and Figure 4.13c. This causes a large temperature difference between the region where the cutting ends and begins. On the contrary, temperature decay becomes gradual along the cutting edges due to conduction and convection of heat to the surrounding environment (Yilbas & Akhtar, 2012; Yilbas et al., 2017). It should be noted that due to large discrepancy between thermal conductivity of Kevlar laminate and carbon fibers, heat conduction from the cutting edge on carbon side dominates over the convection.

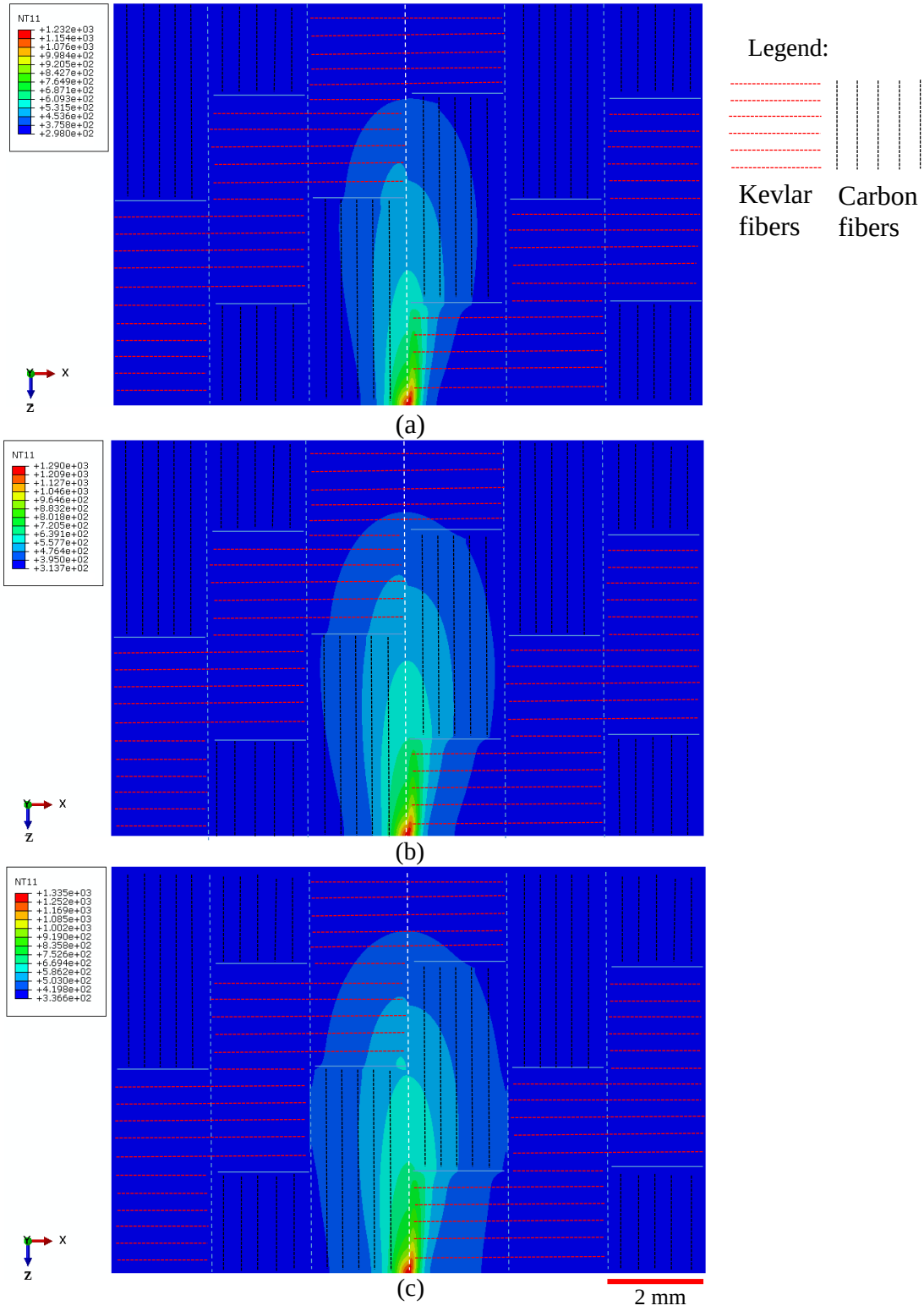

Figure 4.13: Temperature gradient for each laser pass, (a) 1st pass (max temperature= 1232˚K, t=0.24 s); (b) 2nd pass (max temperature= 1290˚K, t=1.04 s); (c) 3rd pass (max temperature= 1335˚K, t=1.84 s)

To reveal the temperature evolution of the specimen for each laser pass, the temperature histories of two specified nodes (nodes d & e, Figure 4.12) on composite top surface are displayed in Figure 4.14. At the start of cutting, temperature of the composite is similar to ambient temperature at 298 ˚K. A steep temperature increase can be seen for each pass. These nodes achieve the peak temperature when the laser approaches near them. It takes about 0.04 seconds to reach maximum temperature for both nodes (z = 1 mm, t = 0.04 seconds, velocity = 25 mm/s). Once the laser beam moves away from the nodes, temperature decays sharply. The total cutting process takes 0.24 seconds for each pass. For subsequent pass to happen, there is 0.56 seconds delay for the laser beam to return to its origin. At this juncture, one can observe rapid cooling of the composite which fall exponentially due to convective and conduction heat transfer from the cutting edge (Equation 3.9). Because of short cooling cycle, there is insufficient time for the materials to return to ambient temperature, resulting an increase of the recorded maximum temperature. The maximum temperatures recorded for Kevlar fibers for each pass are 973 ˚K, 1023 ˚K and 1073 ˚K. The same pattern of temperature profile can be observed for carbon fibers.

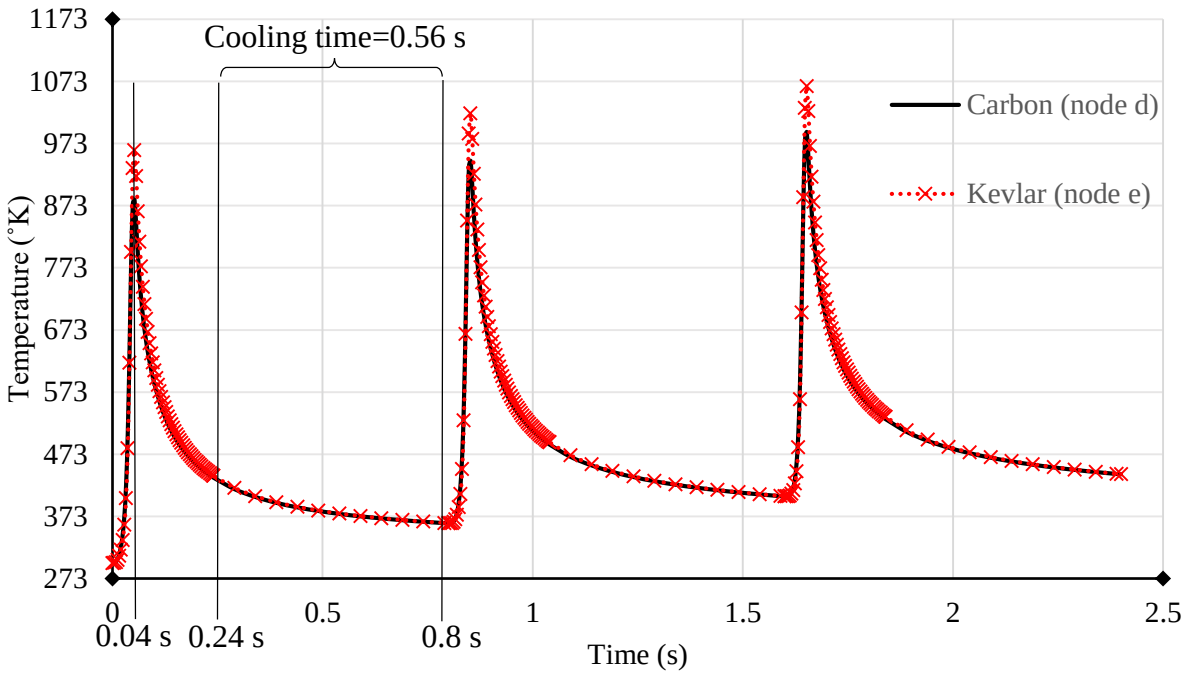

Figure 4.14: Temperature histories of specific nodes (d & e) for cutting parameters: power= 37.6 W and speed= 25 mm/s

Temperature distributions normal to the cutting direction (Figure 4.12) for different laser passes are shown in Figure 4.15. In general, the temperature gradient along the x-axis reduces sharply from the heat source location, and as the distance increases further away from the heat source location, the decay in the temperature gradient becomes gradual. The same finding was shown by (Ghorashi et al., 2019). This indicates that sharp decay in the temperature gradient is expected to generate high thermal stress in this region (Figure 4.16 to Figure 4.20). By referring to Figure 4.12, Figure 4.13 and Figure 4.15a, the rate of temperature decay is not symmetrical due to existence of dissimilar fibers along A-A´. It is interesting to note that in Figure 4.15a, on carbon side, there is sudden drop from maximum temperature of 1133˚K to 1003˚K. Once the temperature drops to 1003˚K, the rate of temperature decay on carbon side is less steep than that of Kevlar side. The sharp decay of temperature at Kevlar fibers results in high temperature gradients in this region. This can be

attributed to the diffusion of temperature along carbon fibers due to higher thermal conductivity. On the contrary, based on findings by (Sihn et al., 2019), for path B-B´, due to the symmetrical presence of carbon fibers the temperature distribution at both sides of cutting area is homogeneous, as shown in Figure 4.15b. The trends for each temperature profile are quite similar which show the effect of increasing number of passes on increasing the temperature for each path. It is noted that the predicted final temperature after the 3rd pass for furthest point from the region irradiated by laser is 363 ˚K i.e., an increase of 65 ˚K (Figure 4.15b).

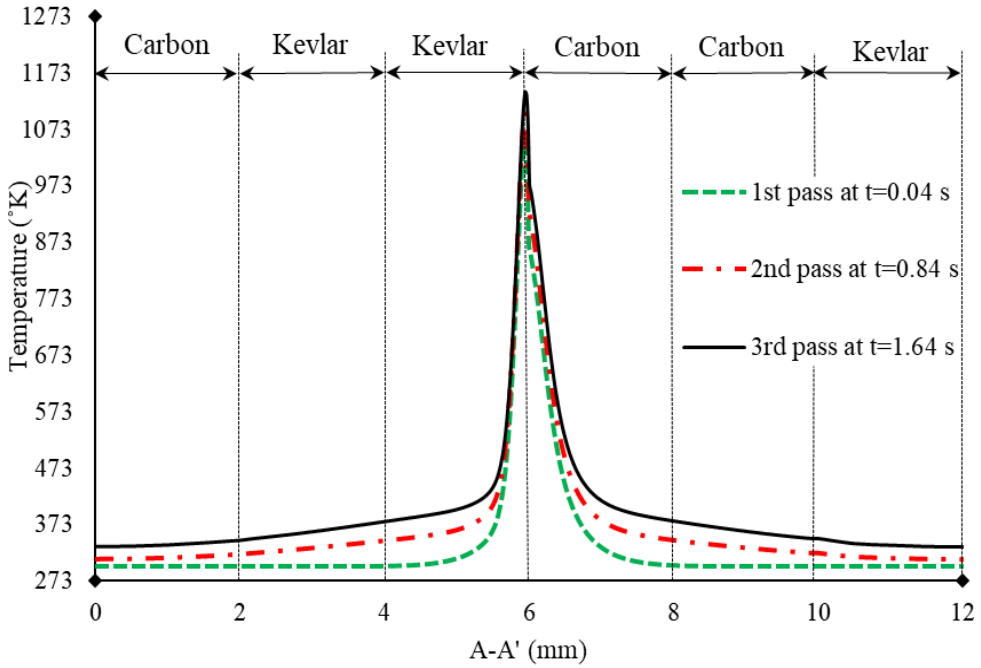

(a)

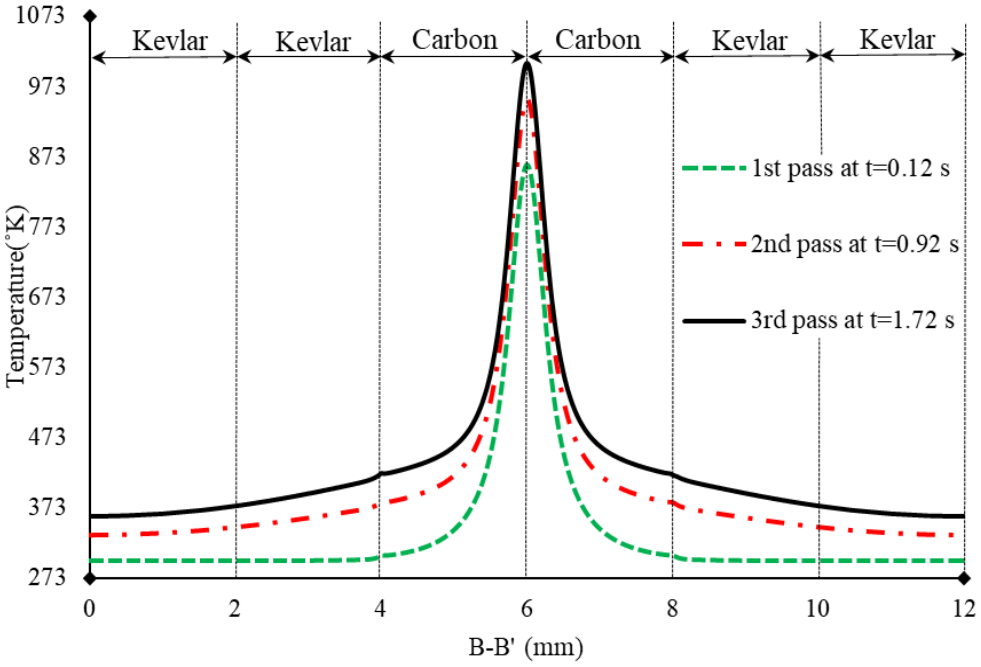

(b)

Figure 4.15: Temperature distribution along, (a) path A-A´; (b) path B-B

4.4.2 Stress Analysis

During laser cutting process, the thermal stress may be developed as a consequence of temperature gradient in carbon/Kevlar composite, regularly generated by rapid heating or cooling. If the outer temperature changes more quickly than the inner temperature, differential dimensional changes confine the free expansion or contraction of the adjacent volume elements within the composite (Wang et al., 2017). Hence, laser heating induces thermal forces and thermal moments which result in tensile or compressive stress. The distribution of the thermal stress would affect the quality of machined composite by laser. If the thermal stress exceeds the critical value, the fracture/damage will occur. Equation 3.13 indicates that the thermal stress rises with the increase of thermal gradient.

Figure 4.16 shows the predicted distribution of residual stress perpendicular to the cutting direction (S_{xx}) and the element removal profile of the carbon/Kevlar composite after each pass. It depicts that the adjacent region near the cutting zone and neighboring HAZ had a significant stress concentration. The approximate maximum values of equivalent stress for carbon and Kevlar fibers are 40.7 MPa (compressive) and 33.2 MPa (tensile), respectively. As shown in Figure 4.16a, due to higher thermal conductivity and higher decomposition temperature of carbon fibers, no element deletion happens in carbon fibers after the 1st pass. On the contrary, Kevlar fibers undergo some ablation. However, the rate of material removal in the region of cutting increases due to heat accumulation after the 2nd pass and 3rd pass, as shown in Figure 4.16b and Figure 4.16c. A detailed comparison between the experimental result (SEM micrograph) and numerical simulation is shown in Figure 4.16d. Cutting edges demonstrate regular pattern with some major defects such as fiber pullout of the carbon fibers and excessive sideways burning on Kevlar side. By comparing Figure 4.16c and Figure 4.16d, it can be observed stress attains considerably high values near the cutting region where

the temperature gradient is high. The significant decay of stress occurs in the region where the temperature decreases along the cutting line, which is attributed to the similar trend of the temperature gradient variation at the cutting edges (Figure 4.13 and Figure 4.15). The same finding was shown by Yilbas et al. (2017) and Fu et al. (2015).

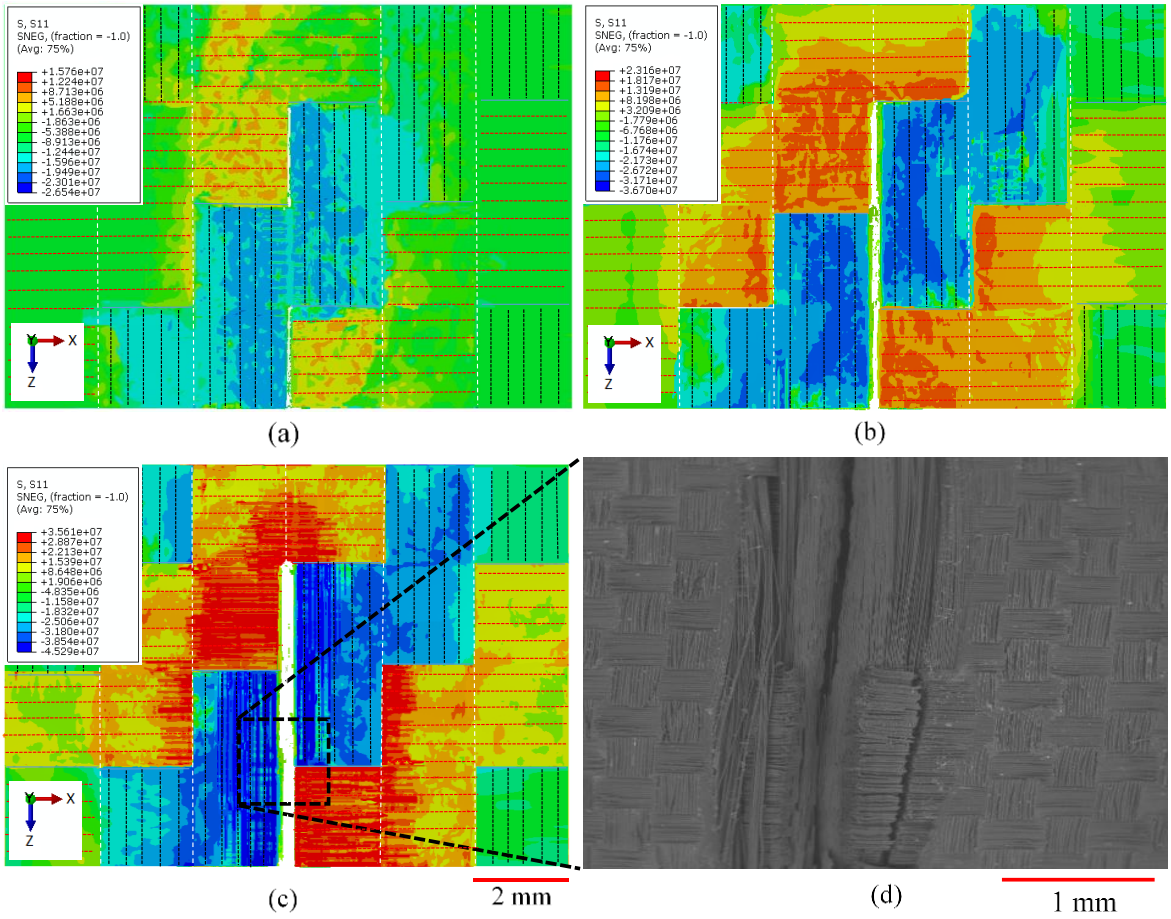

Figure 4.16: Element removal and residual thermal stress profile (S_{xx}); (a) 1st pass, (b) 2nd pass, (c) 3rd pass, (d) SEM micrograph result from experiment after 3rd pass

Figure 4.17 shows profiles of in-plane stress in x-direction (S_{xx}) along the path A-A´ for each pass. In general, the stress increases with the number of passes. Since the time delay of starting the next laser pass is fairly short (0.56 secs), cooling of the region is expected to be incomplete. This results in the increase of temperature gradient, generating relatively

higher thermal stress level after each subsequent pass (Tamrin et al., 2020). However, there is no residual stress in the middle section which corresponds to the actual size of kerf width as evident in Figure 4.17. This is because elastic moduli (E_1 and E_2) have been significantly affected by temperature rise (Equation 3.14), leading to the loss of strength. At the edges of the kerf, one can also observe steep increase in tension on Kevlar side and compression on carbon side. Once maximum stress is reached, the residual stress decreases gradually following the pattern of temperature profile due to transient heat conduction (Equation 3.8). It is noted that there is a steep change in stress profile in the border of carbon and Kevlar fibers. The findings are quite similar to previously performed research by (Bandaru et al., 2020; Hejjaji et al., 2016).

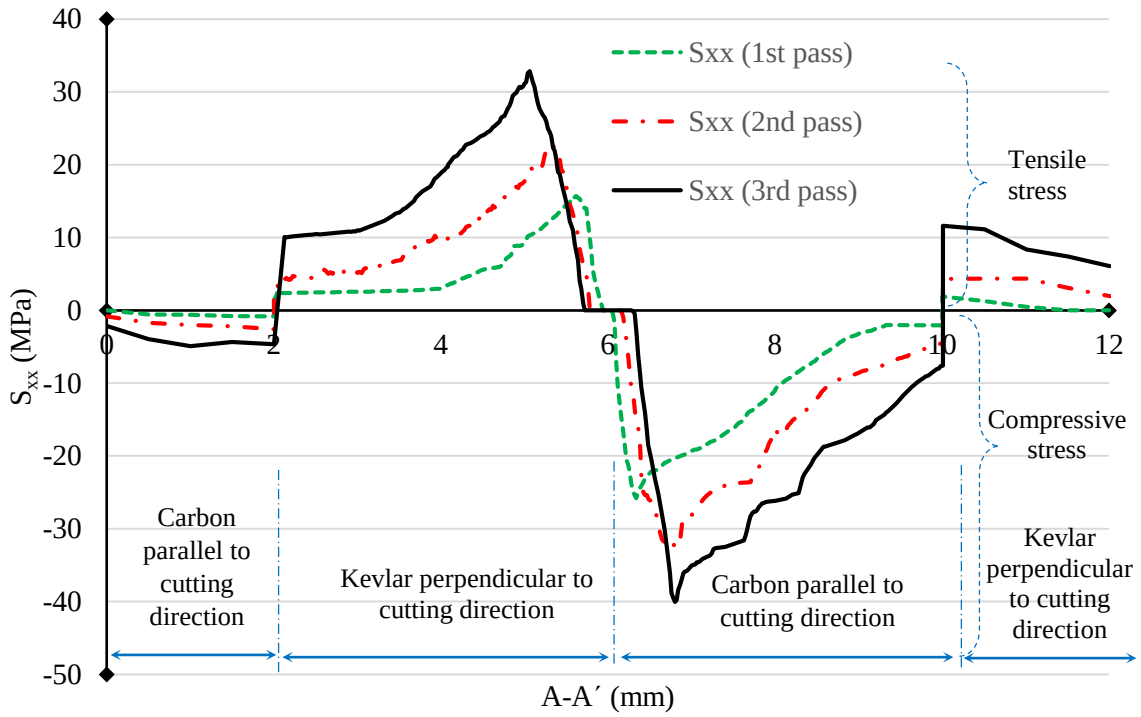

Figure 4.17: In-plane stress in x-direction (S_{xx}) along path A-A´

Figure 4.18 shows in-plane stress in z-direction (S_{zz}) along path A-A´. It is interesting to note that the residual stress in carbon fibers is more noticeable than that of Kevlar fibers as the latter has smaller transverse elastic modulus (E_2) while the former has higher longitudinal elastic modulus (E_1). As shown in Figure 4.17 and Figure 4.18, it can be observed that carbon fibers are in compression in both longitudinal and transverse directions due to higher thermal conductivity which then leads to rapid cooling.

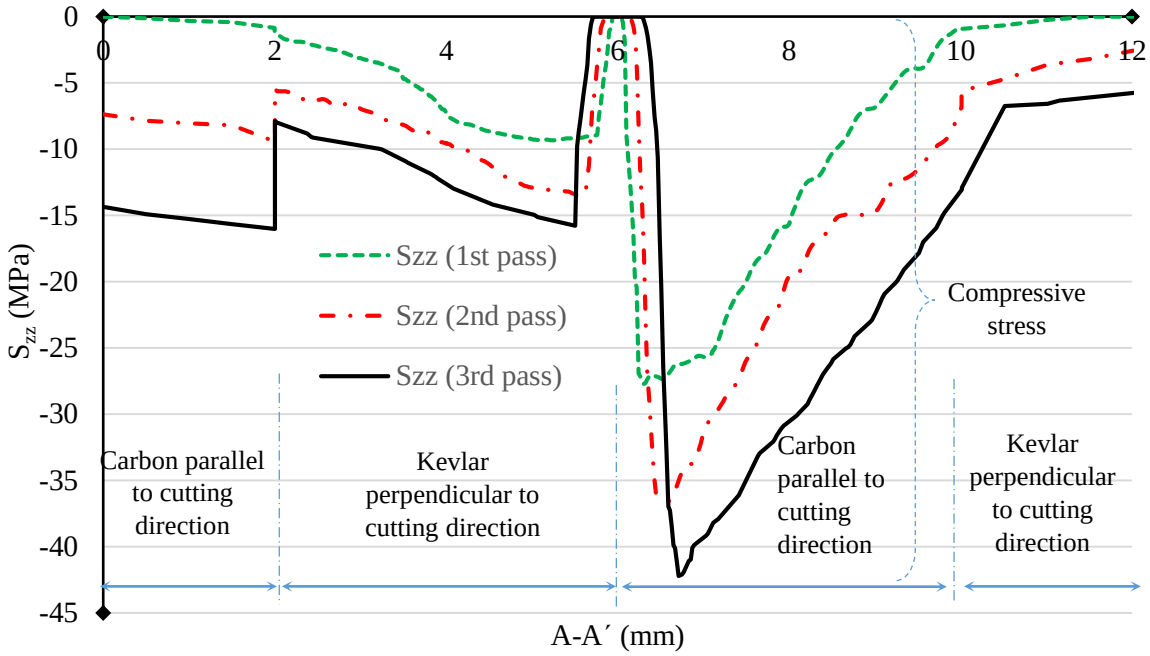

Figure 4.18: In-plane stress in z-direction (S_{zz}) along path A-A´

Figure 4.19 and Figure 4.20 show plane stresses in x- and z-direction (S_{xx} and S_{zz}) for different laser passes during the cutting process along path B-B´. In general, the stress profile is symmetrical in shape. Due to rapid heat dissipation of carbon fibers, there is no ablation occurs after the 1st pass but there exists minor compressive stress in the cutting region. After the 3rd pass, complete loss of strength results in zero residual stress.

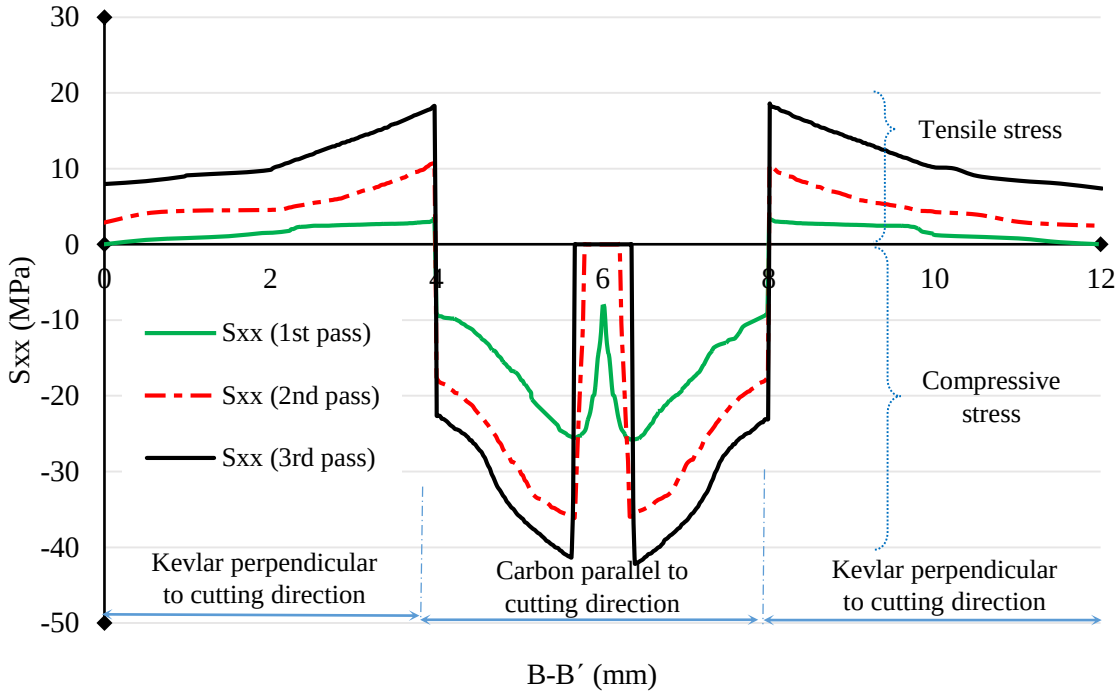

Figure 4.19: S_{xx} distribution along path B-B´

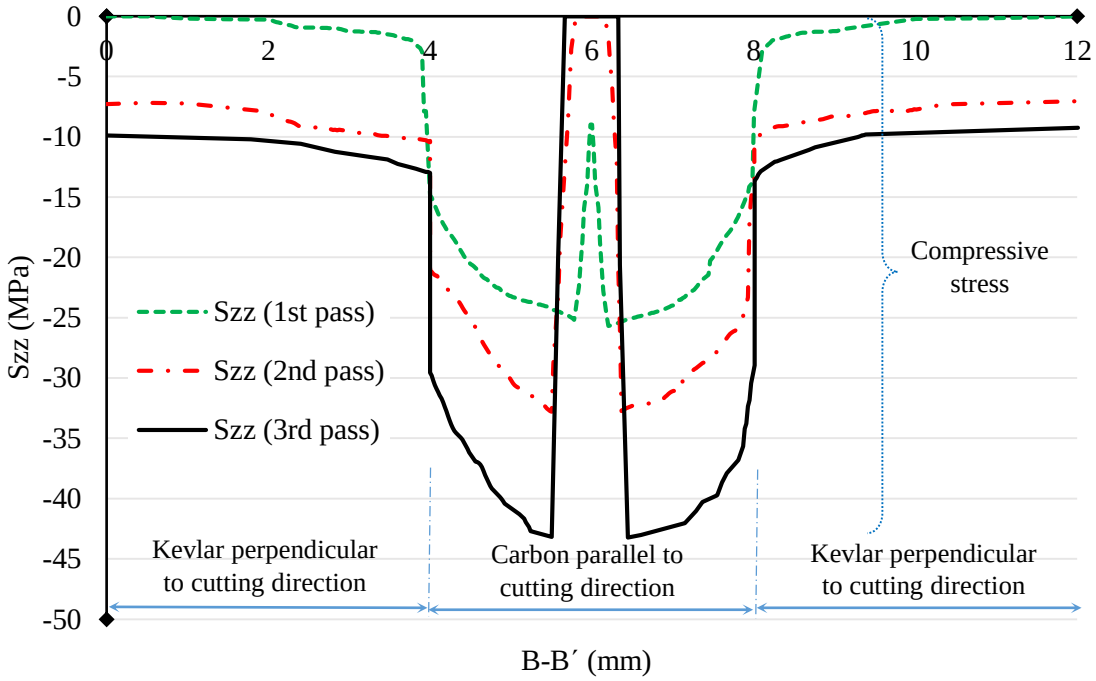

Figure 4.20: S_{zz} distribution along path B-B´

4.4.3 HAZ and kerf formation

Figure 4.21 compares numerical and experimental results of multi-pass laser cutting. In overall, it shows that the numerical results agree well with the experiment concerning HAZ region and kerf width. Kerf width can be measured when the fibers undergo complete ablation where the element is completely removed when damage parameter, *d* equals to 1. Near-maximum damage to composite occurs when damage parameter, *d* is near 1 but fibers remain there with significantly reduced strength. As shown in Figure 4.21, it is interesting to note that both experiment and numerical show similar HAZ features consisting of two distinguishable regions: (a) vaporized matrix and charred fibers near the cutting kerf in region (I), and (b) damage in the neighbouring region predominantly in matrix accompanied by minimal fiber pullout in region (II).

The effects of thermal conductivity on HAZ extension is fairly pronounced as shown in Figure 4.21. HAZ extent is much greater and more noticeable in the region of Kevlar fibers in this type of bidirectional composite. This can be attributed to lower thermal conductivity of the perpendicular Kevlar fibers as compared to parallel carbon fibers. Hence, larger area of burnt Kevlar fibers and vaporized epoxy matrix are observed both numerically and experimentally. Accordingly, larger area loses its strength thoroughly due to reaching high temperature. This is similarly the same finding as discussed by other researchers (Elsheikh et al., 2019; Gautam & Mishra, 2019b; Yilbas et al., 2017).

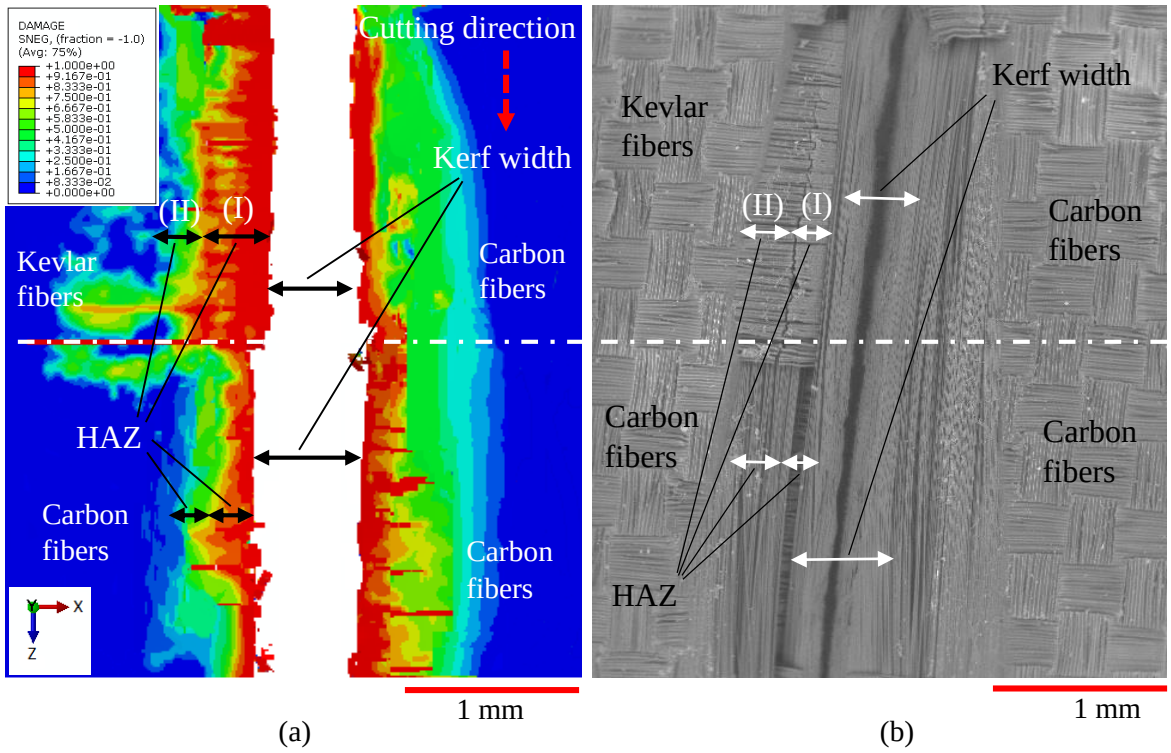

Figure 4.21: The effect of fiber orientation and thermal conductivity on HAZ and kerf width, (a) numerical simulation; (b) SEM micrograph from experiment

Table 4.9 compares results of kerf width and HAZ for both experiment and numerical simulation. The errors of kerf width and HAZ are considerably small i.e., 8.2 % and 5.1 % error, respectively. These can be attributed to discrepancy in estimating thermal-mechanical properties (Table 3.1 and Table 3.2) of the carbon/Kevlar hybrid composite. The comparisons of simulation results with experimental results show there is a great consistency between the results of numerical simulation and experimental measurements of laser optimum parameters. Therefore, the finite element model proves to be suitable for simulating laser ablation of carbon/Kevlar hybrid composite.

Table 4.9: Experimental and numerical results of kerf width and HAZ

Result / Parameter	Experiment	Numerical	Error (%)
Kerf width (mm)	0.677	0.621	8.2 %
HAZ (mm)	0.446	0.469	5.1 %

CHAPTER 5

CONCLUSION AND RECOMMENDATIONS

5.1 Conclusion

In the present study, the effects of different cutting parameters using low-power CW CO_2 laser on synthetic hybrid composite (carbon/Kevlar) was investigated. Response surface methodology was adopted to optimize the response parameters i.e., kerf characteristics and HAZ. Additionally, numerical simulation utilizing Abaqus was performed to calculate the stresses and damaged area developed in the cutting section. The main conclusions from the analysis and results are drawn as follows:

i. In overall, findings evidently showed that laser cutting of carbon/Kevlar composite is possible at low power laser (40 W) with minimum of three passes. The correlation of standoff distance (SOD) and other process parameters (e.g. laser power and cutting speed) was also found effective in laser cutting of hybrid composite. The cutting quality was improved by positioning SOD at focal length. Difference between the thermal properties of carbon fibers, Kevlar fibers and polymer matrix (epoxy) was found to influence HAZ and kerf widths. High thermal conductivity of carbon fibers particularly resulted in large extent of matrix recession and burning of Kevlar fibers around the cut path. Kerf widths were significantly affected by cutting speed and quadratic term of SOD. In areas which the fibers were perpendicular to cutting direction, the kerf width is smaller than that of those parallel to the cutting direction. Fiber pullout varies with standoff distance where it was found minimum at focal length (Objective 1).

ii. ANOVA showed that medium power level (37.6 W) at maximum level of cutting speed (25 mm/s) and SOD of 51.04 mm are optimum in multi-pass cutting of carbon/Kevlar composite. It was observed deviation factor is below 10% for all cut characteristics of predicted and experimented optimum parameters (Objective 2).

iii. By performing numerical simulation, nodal temperature gradient and temperature distribution were plotted for each laser pass. It was discovered that the temperature gradient around the fibers is inhomogeneous due to higher thermal conductivity of carbon fibers than Kevlar fibers. Hence, Kevlar fibers retain more heat as compared to carbon fibers. Furthermore, the remaining residual temperature can be observed after 2nd and 3rd pass due to heat accumulation of the preceding passes. Stress profiles showed that the stress generally increases with the number of passes. Due to a significant temperature rise and loss of strength in the area of laser cutting line, there is no residual stress in the middle section of composite which corresponds to the actual size of kerf width. Once the composite elements reached the decomposition temperature and lost their strength, damage parameter based on Hashin damage resulted in element deletion. When damage parameter (d) is near 1, remaining fibers demonstrate significantly reduced strength. Finally, the numerical results of HAZ region and kerf width agree well with the experiment with errors of 8.2% and 5.1%, respectively (Objective 3).

The effect of laser processing parameters on both HAZ and kerf characteristics were discussed and it was found that by increase or decrease of each laser parameter, carbon/Kevlar composite undergoes different cut characteristics. Among the parameters, low power and high cutting speed show greater influence on output result (Hypothesis 1). Variation of thermal and mechanical properties of the carbon/Kevlar composite constituents

(including carbon fibers, Kevlar fibers and epoxy resin) results in larger HAZ of Kevlar fibers, extensive fiber pullout of carbon fibers and different temperature gradients and stresses on the surface of carbon/Kevlar composite. Additionally, by changing the direction of cutting to 90 degrees, it is observed laser needs more number of passes to cut the sample due to laser movement in perpendicular direction of carbon fibers (Hypothesis 2). Numerical model shows great consistency compared to experimental investigation. User subroutines enable the definition of Gaussian laser beam as a heat source and temperature dependent Hashin criteria as a method for element deletion during laser movement (Hypothesis 3).

5.2 Recommendations

Recommended future work may include the following:

i. Development of three-dimensional Hashin damage criteria using VUSDFLD and VUMAT subroutines for element deletion.
ii. Employment of thermal camera for real-time investigation of thermal distribution and heat propagation during multi-pass laser cutting of synthetic hybrid composite.
iii. Feasibility study for evaluating the use of low-power CO_2 laser for cutting a novel glass/Kevlar/carbon composite.
iv. Intelligent laser cutting of synthetic hybrid composites by artificial intelligence for improved cut characteristics.

REFERENCES

Abaqus, V. (2014). 6.14 Documentation. *Dassault Systemes Simulia Corporation, 651*.

Adalarasan, R., Santhanakumar, M., & Rajmohan, M. (2015). Optimization of laser cutting parameters for Al6061/SiCp/Al_2O_3 composite using grey based response surface methodology (GRSM). *Measurement, 73*, 596 - 606.

Al-Lami, A., Hilmer, P., & Sinapius, M. (2018). Eco-efficiency assessment of manufacturing carbon fiber reinforced polymers (CFRP) in aerospace industry. *Aerospace Science and Technology, 79*, 669 - 678.

Al-Sulaiman, F., Yilbas, B., Ahsan, M., & Karatas, C. (2009). CO_2 laser cutting of Kevlar laminate: influence of assisting gas pressure. *The International Journal of Advanced Manufacturing Technology, 45*(1-2), 62 - 70.

Asim, M., Jawaid, M., Saba, N., Nasir, M., & Sultan, M. T. H. (2017). Processing of hybrid polymer composites—a review. In *Hybrid Polymer Composite Materials* (Thakur, V. K., Thakur, M. K., Gupta, R. K.), pp. 1-22. London: Elsevier Applied Science Publication.

Aslan, A., Güneş, A., Salur, E., Şahin, Ö. S., Karadağ, H. B., & Akdemir, A. (2018). Mechanical properties and microstructure of composites produced by recycling metal chips. *International Journal of Minerals, Metallurgy, and Materials, 25*(9), 1070-1079.

Bandaru, A. K., Chouhan, H., & Bhatnagar, N. (2020). High strain rate compression testing of intra-ply and inter-ply hybrid thermoplastic composites reinforced with Kevlar/basalt fibers. *Polymer Testing, 84*, 106 - 407.

Biswas, R., Kuar, A., Sarkar, S., & Mitra, S. (2010). A parametric study of pulsed Nd: YAG laser micro-drilling of gamma-titanium aluminide. *Optics & Laser Technology, 42*(1), 23 - 31.

Bluemel, S., Staehr, R., Jaeschke, P., Suttmann, O., & Overmeyer, L. (2015). Correlation of internal and surface temperatures during laser cutting of epoxy-based carbon fibre reinforced plastics. *Journal of Reinforced Plastics and Composites, 34*(8), 662 - 671.

Botelho, E. C., Silva, R. A., Pardini, L. C., & Rezende, M. C. (2006). A review on the development and properties of continuous fiber/epoxy/aluminum hybrid composites for aircraft structures. *Materials Research, 9*(3), 247 - 256.

Choudhury, I., & Chuan, P. (2013). Experimental evaluation of laser cut quality of glass fibre reinforced plastic composite. *Optics and Lasers in Engineering, 51*(10), 1125 - 1132.

Chouhan, H., Singh, D., Parmar, V., Kalyanasundaram, D., & Bhatnagar, N. (2016). Laser machining of Kevlar fiber reinforced laminates–Effect of polyetherimide versus polypropylene matrix. *Composites Science and Technology, 134*, 267 - 274.

Cugnoni, J., Amacher, R., Kohler, S., Brunner, J., Kramer, E., Dransfeld, C., . . . Botsis, J. (2018). Towards aerospace grade thin-ply composites: Effect of ply thickness, fibre, matrix and interlayer toughening on strength and damage tolerance. *Composites Science and Technology, 168*, 467 - 477.

Cui, G., Yang, C., Li, Z.-l., & Zhou, Z. (2016). Experimental study and theoretical calculation of flammability limits of methane/air mixture at elevated temperatures and pressures. *Journal of Loss Prevention in the Process Industries, 41*, 252 - 258.

Davim, J. P., Barricas, N., Conceicao, M., & Oliveira, C. (2008). Some experimental studies on CO_2 laser cutting quality of polymeric materials. *Journal of Materials Processing Technology*, *198*(1-3), 99 - 104.

Di Ilio, A., & Tagliaferri, V. (1989). Thermal damage in laser cutting of $(0/90)_{2s}$ aramid/epoxy laminates. *Composites*, *20*(2), 115 - 119.

Du, J., Ming, W., Ma, J., He, W., Cao, Y., Li, X., & Liu, K. (2018). New observations of the fiber orientations effect on machinability in grinding of C/SiC ceramic matrix composite. *Ceramics International, 44*(12), 13916 - 13928.

Dubey, A. K., & Yadava, V. (2008). Laser beam machining—a review. *International Journal of Machine Tools and Manufacture, 48*(6), 609 - 628.

Dumbhare, P. A., Dubey, S., Deshpande, Y. V., Andhare, A. B., & Barve, P. S. (2018). Modelling and multi-objective optimization of surface roughness and kerf taper angle in abrasive water jet machining of steel. *Journal of the Brazilian Society of Mechanical Sciences and Engineering*, *40*(5), 1 - 13.

El-Hofy, M., & El-Hofy, H. (2019). Laser beam machining of carbon fiber reinforced composites: a review. *The International Journal of Advanced Manufacturing Technology, 101*(9-12), 2965 - 2975.

Elsheikh, A. H., Deng, W., & Showaib, E. A. (2019). Improving laser cutting quality of polymethylmethacrylate sheet: experimental investigation and optimization. *Journal of Materials Research and Technology, 9*(2), 1325 – 1339.

Eltawahni, H., Olabi, A.-G., & Benyounis, K. (2011). Investigating the CO_2 laser cutting parameters of MDF wood composite material. *Optics & Laser Technology, 43*(3), 648 - 659.

Finger, J., Weinand, M., & Wortmann, D. (2013). Ablation and cutting of carbon-fiber reinforced plastics using picosecond pulsed laser radiation with high average power. *Journal of Laser Applications, 25*(4), 1 - 5.

Fu, C., Sealy, M. P., Guo, Y., & Wei, X. (2015). Finite element simulation and experimental validation of pulsed laser cutting of nitinol. *Journal of Manufacturing Processes, 19*, 81 - 86.

Fu, K., & Ye, L. (2019). Modelling of lightning-induced dynamic response and mechanical damage in CFRP composite laminates with protection. *Composite Structures, 218*, 162 - 173.

Fürst, A., Hipp, D., Klotzbach, A., Hauptmann, J., Wetzig, A., & Beyer, E. (2016). Increased Cutting Efficiency due to Multi-Wavelength Remote-Laser-Ablation of Fiber-Reinforced Polymers. *Advanced Engineering Materials, 18*(3), 403 - 408.

Gaitonde, V., Karnik, S., Rubio, J. C., Correia, A. E., Abrao, A., & Davim, J. P. (2008). Analysis of parametric influence on delamination in high-speed drilling of carbon fiber reinforced plastic composites. *Journal of Materials Processing Technology, 203*(1-3), 431 - 438.

Gautam, G. D., & Mishra, D. R. (2019). Dimensional accuracy improvement by parametric optimization in pulsed Nd: YAG laser cutting of Kevlar-29/basalt fiber-reinforced hybrid composites. *Journal of the Brazilian Society of Mechanical Sciences and Engineering, 41*(7), 1 - 22.

Gautam, G. D., & Mishra, D. R. (2019). Firefly algorithm based optimization of kerf quality characteristics in pulsed Nd: YAG laser cutting of basalt fiber reinforced composite. *Composites Part B: Engineering, 176*, 1 - 15.

Genna, S., Menna, E., Rubino, G., & Tagliaferri, V. (2020). Experimental Investigation of Industrial Laser Cutting: The Effect of the Material Selection and the Process Parameters on the Kerf Quality. *Applied Sciences, 10*(14), 49 - 56.

Ghavidel, A. K., Azdast, T., Shabgard, M. R., Navidfar, A., & Shishavan, S. M. (2015). Effect of carbon nanotubes on laser cutting of multi-walled carbon nanotubes/poly methyl methacrylate nanocomposites. *Optics & Laser Technology, 67*, 119 - 124.

Ghorashi, M. S., Farrahi, G. H., & Movahhedy, M. R. (2019). Considering cyclic plasticity to predict residual stresses in laser cladding of Inconel 718 multi bead samples. *Journal of Manufacturing Processes, 42*, 149 - 158.

Giridharan, R. (2019). Preparation and property evaluation of Glass/Ramie fibers reinforced epoxy hybrid composites. *Composites Part B: Engineering, 167*, 342 - 345.

Goldak, J., Chakravarti, A., & Bibby, M. (1984). A new finite element model for welding heat sources. *Metallurgical Transactions B, 15*(2), 299 - 305.

Gururaja, M., & Rao, A. H. (2012). A review on recent applications and future prospectus of hybrid composites. *International Journal of Soft Computing and Engineering (IJSCE), 1*(6), 352 - 355.

Hashin, Z. (1980). Failure criteria for unidirectional fiber composites. *Journal of Applied Mechanics, 47*(2), 329 - 334.

Hayat, M. D., Singh, H., He, Z., & Cao, P. (2019). Titanium metal matrix composites: An overview. *Composites Part A: Applied Science and Manufacturing, 121*, 418 - 438.

Hecht, E. (2002). *Optics*, 4th. International ed., San Francisco: Addison-Wesley.

Hejjaji, A., Singh, D., Kubher, S., Kalyanasundaram, D., & Gururaja, S. (2016). Machining damage in FRPs: Laser versus conventional drilling. *Composites Part A: Applied Science and Manufacturing, 82*, 42 - 52.

Herzog, D., Jaeschke, P., Meier, O., & Haferkamp, H. (2008). Investigations on the thermal effect caused by laser cutting with respect to static strength of CFRP. *International Journal of Machine Tools and Manufacture, 48*(12-13), 1464 - 1473.

Herzog, D., Schmidt-Lehr, M., Canisius, M., Oberlander, M., Tasche, J.-P., & Emmelmann, C. (2015). Laser cutting of **carbon** fiber reinforced plastic using a 30 kW fiber laser. *Journal of Laser Applications, 27*(S2), 1 - 17.

Herzog, D., Schmidt-Lehr, M., Oberlander, M., Canisius, M., Radek, M., & Emmelmann, C. (2016). Laser cutting of carbon fibre reinforced plastics of high thickness. *Materials & Design, 92*, 742 - 749.

Hong, K.-M., & Shin, Y. C. (2017). Prospects of laser welding technology in the automotive industry: A review. *Journal of Materials Processing Technology, 245*, 46 - 69.

Hyer, M. W., & White, S. R. (2009). *Stress analysis of fiber-reinforced composite materials*, 3rd ed., Pennsylvania: DEStech Publications, Inc.

Isa, M., Ahmed, A., Aderemi, B., Taib, R., & Mohammed-Dabo, I. (2013). Effect of fiber type and combinations on the mechanical, physical and thermal stability properties of polyester hybrid composites. *Composites Part B: Engineering, 52*, 217 - 223.

Jaeschke, P., Kern, M., Stute, U., Kracht, D., & Haferkamp, H. (2014). Laser processing of continuous carbon fibre reinforced polyphenylene sulphide organic sheets—Correlation of process parameters and reduction in static tensile strength properties. *Journal of Thermoplastic Composite Materials, 27*(3), 324 - 337.

Jariwala, H., & Jain, P. (2019). A review on mechanical behavior of natural fiber reinforced polymer composites and its applications. *Journal of Reinforced Plastics and Composites, 38*(10), 441 - 453.

Karataş, M. A., Motorcu, A. R., & Gökkaya, H. (2020). Optimization of machining parameters for kerf angle and roundness error in abrasive water jet drilling of CFRP composites with different fiber orientation angles. *Journal of the Brazilian Society of Mechanical Sciences and Engineering, 42*(4), 1 - 27.

Karimzad Ghavidel, A., Navidfar, A., Shabgard, M., & Azdast, T. (2016). Role of CO_2 laser cutting conditions on anisotropic properties of nanocomposite contain carbon nanotubes. *Journal of Laser Applications, 28*(3), 1 - 9.

Khan, F., Qayyum, F., Asghar, W., Azeem, M., Anjum, Z., Nasir, A., & Shah, M. (2017). Effect of various surface preparation techniques on the delamination properties of vacuum infused Carbon fiber reinforced aluminum laminates (CARALL): Experimentation and numerical simulation. *Journal of Mechanical Science and Technology, 31*(11), 5265 - 5272.

Kim, H. S. (2000). On the rule of mixtures for the hardness of particle reinforced composites. *Materials Science and Engineering: A, 289*(1-2), 30 - 33.

Kim, H. S., Wang, W.-X., & Takao, Y. (1999). Evaluation by FEM of temperature-dependent damage behavior in quasi-isotropic carbon/epoxy laminates. *Advanced Composite Materials, 8*(3), 247 - 257.

Kononenko, T., Freitag, C., Komlenok, M., Onuseit, V., Weber, R., Graf, T., & Konov, V. (2014). Oxygen-assisted multipass cutting of carbon fiber reinforced plastics with ultra-short laser pulses. *Journal of Applied Physics, 115*(10), 103 - 107.

Kotlyar, V. V., Kovalev, A. A., & Porfirev, A. P. (2019). Calculation of fractional orbital angular momentum of superpositions of optical vortices by intensity moments. *Optics Express, 27*(8), 11236 - 11251.

Kwon, D.-J., Kim, J.-H., Park, S.-M., Kwon, I.-J., DeVries, K. L., & Park, J.-M. (2019). Damage sensing, mechanical and interfacial properties of resins suitable for new CFRP rope for elevator applications. *Composites Part B: Engineering, 157*, 259 - 265.

Le, H., Penchev, P., Henrottin, A., Bruneel, D., Nasrollahi, V., Ramos-de-Campos, J. A., & Dimov, S. (2020). Effects of Top-hat Laser Beam Processing and Scanning Strategies in Laser Micro-Structuring. *Micromachines, 11*(2), 1 - 17.

Leone, C., & Genna, S. (2018). Heat affected zone extension in pulsed Nd: YAG laser cutting of CFRP. *Composites Part B: Engineering, 140*, 174 - 182.

Leone, C., Genna, S., & Tagliaferri, V. (2014). Fibre laser cutting of CFRP thin sheets by multi-passes scan technique. *Optics and Lasers in Engineering, 53*, 43 - 50.

Li, M., Gan, G., Zhang, Y., & Yang, X. (2020). Thermal defect characterization and strain distribution of CFRP laminate with open hole following fiber laser cutting process. *Optics & Laser Technology, 122*, 1 - 11.

Li, M., Huang, M., Chen, Y., Gong, P., & Yang, X. (2019). Effects of processing parameters on kerf characteristics and surface integrity following abrasive waterjet slotting of Ti6Al4V/CFRP stacks. *Journal of Manufacturing Processes, 42*, 82 - 95.

Li, M., Li, S., Yang, X., Zhang, Y., & Liang, Z. (2019). Effect of lay-up configuration and processing parameters on surface quality during fiber laser cutting of CFRP laminates. *The International Journal of Advanced Manufacturing Technology, 100*(1-4), 623 - 635.

Li, Z., Zheng, H., Lim, G., Chu, P., & Li, L. (2010). Study on UV laser machining quality of carbon fibre reinforced composites. *Composites Part A: Applied Science and Manufacturing, 41*(10), 1403 - 1408.

Liu, Y.-C., Wu, C.-W., Huang, Y.-H., Song, H.-W., & Huang, C.-G. (2017). Interlaminar damage of carbon fiber reinforced polymer composite laminate under continuous wave laser irradiation. *Optics and Lasers in Engineering, 88*, 91 - 101.

Mallick, P. K. (2007). *Fiber-reinforced composites: materials, manufacturing, and design*, 3rd ed., Florida: CRC press.

Marimuthu, S., Antar, M., & Dunleavey, J. (2019). Characteristics of micro-hole formation during fibre laser drilling of aerospace superalloy. *Precision Engineering, 55*, 339 - 348.

Marimuthu, S., Dunleavey, J., Liu, Y., Antar, M., & Smith, B. (2019). Laser cutting of aluminium-alumina metal matrix composite. *Optics & Laser Technology, 117*, 251 - 259.

Masoud, F., Sapuan, S., Mohd Ariffin, M. K. A., Nukman, Y., & Bayraktar, E. (2020). Cutting processes of natural fiber-reinforced polymer composites. *Polymers, 12*(6), 1 - 17.

Meijer, J. (2004). Laser beam machining (LBM), state of the art and new opportunities. *Journal of Materials Processing Technology, 149*(1-3), 2 - 17.

Ming, I. W. M., Azmi, A. I., Chuan, L. C., & Mansor, A. F. (2018). Experimental study and empirical analyses of abrasive waterjet machining for hybrid carbon/glass fiber-reinforced composites for improved surface quality. *The International Journal of Advanced Manufacturing Technology, 95*(9-12), 3809 - 3822.

Mishra, D. R., Dutt, G. G., Prakash, D., Bajaj, A., Sharma, A., Bisht, R., & Gupta, S. (2020). Optimization of kerf deviations in pulsed Nd: YAG laser cutting of hybrid composite laminate using GRA. *FME Transactions, 48*(1), 109 - 116.

Mivehchi, H., & Varvani-Farahani, A. (2010). The effect of temperature on fatigue strength and cumulative fatigue damage of FRP composites. *Procedia Engineering, 2*(1), 2011-2020.

Muramatsu, M., Harada, Y., Suzuki, T., & Niino, H. (2015). Infrared stress measurements of thermal damage to laser-processed carbon fiber reinforced plastics. *Composites Part A: Applied Science and Manufacturing, 68*, 242 - 250.

Nagesh, S., Murthy, H. N., Pal, R., Dev, S. S., & Krishna, M. (2017). Investigation of the effect of nanofillers on the quality of CO_2 laser cutting of FRP nanocomposites. *The International Journal of Advanced Manufacturing Technology, 90*(5-8), 2047 - 2061.

Nattapat, M., Marimuthu, S., Kamara, A., & Esfahani, M. N. (2015). Laser surface modification of carbon fiber reinforced composites. *Materials and Manufacturing Processes, 30*(12), 1450 - 1456.

Negarestani, R., & Li, L. (2013). Fibre laser cutting of carbon fibre–reinforced polymeric composites. *Proceedings of the Institution of Mechanical Engineers, Part B: Journal of Engineering Manufacture, 227*(12), 1755 - 1766.

Negarestani, R., Sundar, M., Sheikh, M., Mativenga, P., Li, L., Li, Z., . . . Lim, G. (2010). Numerical simulation of laser machining of carbon-fibre-reinforced composites. *Proceedings of the Institution of Mechanical Engineers, Part B: Journal of Engineering Manufacture, 224*(7), 1017 - 1027.

Niino, H., Kawaguchi, Y., Sato, T., Narazaki, A., Kurosaki, R., Muramatsu, M., . . . Nagashima, T. (2014). Laser cutting of carbon fiber reinforced thermo-plastic (CFRTP) by IR laser irradiation. *Journal of Laser Micro Nanoengineering, 9*(2), 180 - 186.

Ning, F., Wang, H., Cong, W., & Fernando, P. (2017). A mechanistic ultrasonic vibration amplitude model during rotary ultrasonic machining of CFRP composites. *Ultrasonics, 76*, 44 - 51.

Ohkubo, T., Sato, Y., Matsunaga, E. I., & Tsukamoto, M. (2017). Three-dimensional numerical simulation during laser processing of CFRP. *Applied Surface Science, 417*, 104 - 107.

Ohkubo, T., Tsukamoto, M., & Sato, Y. (2016). Numerical simulation of combustion effects during laser processing of carbon fiber reinforced plastics. *Applied Physics A, 122*(3), 1 - 5.

Pan, C., & Hocheng, H. (1996). The anisotropic heat-affected zone in the laser grooving of fiber-reinforced composite material. *Journal of Materials Processing Technology, 62*(1-3), 54 - 60.

Pan, C., & Hocheng, H. (2001). Evaluation of anisotropic thermal conductivity for unidirectional FRP in laser machining. *Composites Part A: Applied Science and Manufacturing*, *32*(11), 1657 - 1667.

Pesce, P., Lagazzo, A., Barberis, F., Repetto, L., Pera, F., Baldi, D., & Menini, M. (2019). Mechanical characterisation of multi vs. uni-directional carbon fiber frameworks for dental implant applications. *Materials Science and Engineering: C, 102*, 186 - 191.

Priyanka, P., Dixit, A., & Mali, H. S. (2019). High strength Kevlar fiber reinforced advanced textile composites. *Iranian Polymer Journal, 1*, 1-18.

Quintero, F., Riveiro, A., Lusquiños, F., Comesaña, R., & Pou, J. (2011). CO_2 laser cutting of phenolic resin boards. *Journal of Materials Processing Technology, 211*(11), 1710 - 1718.

Rao, S., Sethi, A., Das, A. K., Mandal, N., Kiran, P., Ghosh, R., . . . Mandal, A. (2017). Fiber laser cutting of CFRP composites and process optimization through response surface methodology. *Materials and Manufacturing Processes, 32*(14), 1612 - 1621.

Raza, M. S., Datta, S., Bule, B., & Saha, P. (2019). Parametric study of laser cutting of carbon fibre reinforced polymer (CFRP) and the effect of fibre orientation on cutting quality. *Advances in Materials and Processing Technologies, 5*(2), 202 - 212.

Reddy, P. S., Kesavan, R., & Ramnath, B. V. (2018). Investigation of mechanical properties of aluminium 6061-silicon carbide, boron carbide metal matrix composite. *Silicon, 10*(2), 495 - 502.

Riveiro, A., Quintero, F., Lusquiños, F., Del Val, J., Comesaña, R., Boutinguiza, M., & Pou, J. (2012). Experimental study on the CO_2 laser cutting of carbon fiber reinforced plastic composite. *Composites Part A: Applied Science and Manufacturing, 43*(8), 1400 - 1409.

Russo Spena, P. (2017). CO_2 laser cutting of hot stamping boron steel sheets. *Metals, 7*(11), 1 - 18.

Safri, S. N. A., Sultan, M. T. H., Jawaid, M., & Jayakrishna, K. (2018). Impact behaviour of hybrid composites for structural applications: A review. *Composites Part B: Engineering, 133*, 112 - 121.

Salama, A., Li, L., Mativenga, P., & Whitehead, D. (2016). TEA CO_2 laser machining of CFRP composite. *Applied Physics A, 122*(5), 1 - 19.

Sheng, P. S., & Joshi, V. S. (1995). Analysis of heat-affected zone formation for laser cutting of stainless steel. *Journal of Materials Processing Technology, 53*(3-4), 879 - 892.

Shyha, I. (2013). An investigation into CO_2 laser trimming of CFRP and GFRP composites. *Procedia Engineering, 63*, 931 - 937.

Siakeng, R., Jawaid, M., Ariffin, H., Sapuan, S., Asim, M., & Saba, N. (2019). Natural fiber reinforced polylactic acid composites: A review. *Polymer Composites, 40*(2), 446 - 463.

Sihn, S., Pitz, J., Gerzeski, R. H., Roy, A. K., & Vernon, J. P. (2019). Experimentally-validated computational model for temperature evolution within laser heated fiber-reinforced polymer matrix composites. *Composite Structures, 207*, 966 - 973.

Solati, A., Hamedi, M., & Safarabadi, M. (2019). Combined GA-ANN approach for prediction of HAZ and bearing strength in laser drilling of GFRP composite. *Optics & Laser Technology, 113*, 104 - 115.

Staehr, R., Bluemel, S., Jaeschke, P., Suttmann, O., & Overmeyer, L. (2016). Laser cutting of composites—Two approaches toward an industrial establishment. *Journal of Laser Applications, 28*(2), 1 - 7.

Steen, W. M., & Mazumder, J. (2010). *Laser material processing,* 4th ed., London: Springer-Verlag London Limited.

Sun, D., Han, F., & Ying, W. (2018). Numerical simulation of water jet–guided laser cutting of carbon fiber–reinforced plastics. *Proceedings of the Institution of Mechanical Engineers, Part B: Journal of Engineering Manufacture, 10,* 2023 - 2032.

Suthar, J., & Patel, K. (2018). Processing issues, machining, and applications of aluminum metal matrix composites. *Materials and Manufacturing Processes, 33*(5), 499 - 527.

Swolfs, Y., Gorbatikh, L., & Verpoest, I. (2014). Fibre hybridisation in polymer composites: a review. *Composites Part A: Applied Science and Manufacturing, 67,* 181 - 200.

Swolfs, Y., Verpoest, I., & Gorbatikh, L. (2019). Recent advances in fibre-hybrid composites: materials selection, opportunities and applications. *International Materials Reviews, 64*(4), 181 - 215.

Tabata, N., Yagi, S., & Hishii, M. (1996). Present and future of lasers for fine cutting of metal plate. *Journal of Materials Processing Technology, 62*(4), 309 - 314.

Takahashi, K., Tsukamoto, M., Masuno, S., & Sato, Y. (2016). Heat conduction analysis of laser CFRP processing with IR and UV laser light. *Composites Part A: Applied Science and Manufacturing, 84,* 114 - 122.

Takahashi, K., Tsukamoto, M., Masuno, S., Sato, Y., Yoshida, H., Tsubakimoto, K., . . . Ogata, H. (2015). Influence of laser scanning conditions on CFRP processing with a pulsed fiber laser. *Journal of Materials Processing Technology, 222*, 110 - 121.

Tamrin, K., Moghadasi, K., & Sheikh, N. (2020). Experimental and numerical investigation on multi-pass laser cutting of natural fibre composite. *The International Journal of Advanced Manufacturing Technology, 107*, 1483 - 1504.

Tong, Y., Bai, S., Zhang, H., & Ye, Y. (2013). Laser ablation behavior and mechanism of C/SiC composite. *Ceramics International, 39*(6), 6813 - 6820.

Turner, J., Scaife, R., & El-Dessouky, H. (2015). Effect of machining coolant on integrity of CFRP composites. *Advanced Manufacturing: Polymer & Composites Science, 1*(1), 54 - 60.

Vigneshwaran, S., Uthayakumar, M., & Arumugaprabu, V. (2018). Abrasive water jet machining of fiber-reinforced composite materials. *Journal of Reinforced Plastics and Composites, 37*(4), 230 - 237.

Wang, B., Han, W., Ming, Y., Zhang, X., Zhu, Y., Duan, Y., . . . Zhao, H. (2020). Preparation and Tribological Study of Graphene Coating on Glass Fiber-Reinforced Composite Using Modified Percolating-Assisted Resin Film Infusion Method. *Materials, 13*(4), 1 - 15.

Wang, H., Cao, M., Siddique, A., Sun, B., & Gu, B. (2017). Numerical analysis of thermal expansion behaviors and interfacial thermal stress of 3D braided composite materials. *Computational Materials Science, 138*, 77 - 91.

Whitlow, T., Jones, E., & Przybyla, C. (2016). In-situ damage monitoring of a SiC/SiC ceramic matrix composite using acoustic emission and digital image correlation. *Composite Structures, 158,* 245 - 251.

Wu, C.-W., Wu, X.-Q., & Huang, C.-G. (2015). Ablation behaviors of carbon reinforced polymer composites by laser of different operation modes. *Optics & Laser Technology, 73,* 23 - 28.

Xu, H., & Hu, J. (2017). Modeling of the material removal and heat affected zone formation in CFRP short pulsed laser processing. *Applied Mathematical Modelling, 46,* 354 - 364.

Yang, J., Liu, J., Liu, W., Wang, J., & Tang, T. (2015). Recycling of carbon fibre reinforced epoxy resin composites under various oxygen concentrations in nitrogen–oxygen atmosphere. *Journal of Analytical and Applied Pyrolysis, 112,* 253 - 261.

Yang, L. J., Cheng, X. L., Wang, G. W., Xue, Q. M., Ding, Y., & Wang, Y. (2017). Experimental evaluation of cutting quality of carbon fibre reinforced polymer with pulsed laser. *Applied Mechanics and Materials, 868,* 172 - 177.

Yilbas, B., & Akhtar, S. (2012). Laser cutting of Kevlar laminates and thermal stress formed at cutting sections. *Optics and Lasers in Engineering, 50*(2), 204 - 209.

Yilbas, B., Akhtar, S., & Karatas, C. (2017). Laser circular cutting of Kevlar sheets: Analysis of thermal stress filed and assessment of cutting geometry. *Optics & Laser Technology, 96,* 180 - 189.

Yilbas, B. S., Khan, S., Raza, K., Keles, O., Ubeyli, M., Demir, T., & Karakas, M. S. (2010). Laser cutting of 7050 Al alloy reinforced with Al_2O_3 and B4C composites. *The International Journal of Advanced Manufacturing Technology, 50*(1-4), 185 - 193.

Yilbas, B. S., Shaukat, M. M., & Ashraf, F. (2017). Laser cutting of various materials: Kerf width size analysis and life cycle assessment of cutting process. *Optics & Laser Technology*, *93*, 67 - 73.

Zhu, C., Zhu, P., & Liu, Z. (2019). Uncertainty analysis of mechanical properties of plain woven carbon fiber reinforced composite via stochastic constitutive modeling. *Composite Structures*, *207*, 684 - 700.

APPENDICES

Appendix 1- Publications

1. **Moghadasi, K.**, & Tamrin, K. F. (2020). Experimental investigation and parameter optimization of low power CO_2 laser cutting of a carbon/Kevlar fiber-reinforced hybrid composite. *Lasers in Engineering (Old City Publishing)*, *45*(1-3), 85-108. (IF: 0.538)
2. **Moghadasi, K.**, & Tamrin, K. F. (2020). Multi-pass laser cutting of carbon/Kevlar hybrid composite: Prediction of thermal stress, heat-affected zone, and kerf width by thermo-mechanical modeling. *Proceedings of the Institution of Mechanical Engineers, Part L: Journal of Materials: Design and Applications*, *234*(9), 1228-1241. (IF: 2.014)

Appendix 2 – Experimental results of HAZ for different regions of carbon/Kevlar composite to check the impact of material characteristic variation, laser source calibration and digital microscope calibration (Experiment No.1: P= 36 W, V= 15 mm/s, SOD= 50.8 mm)

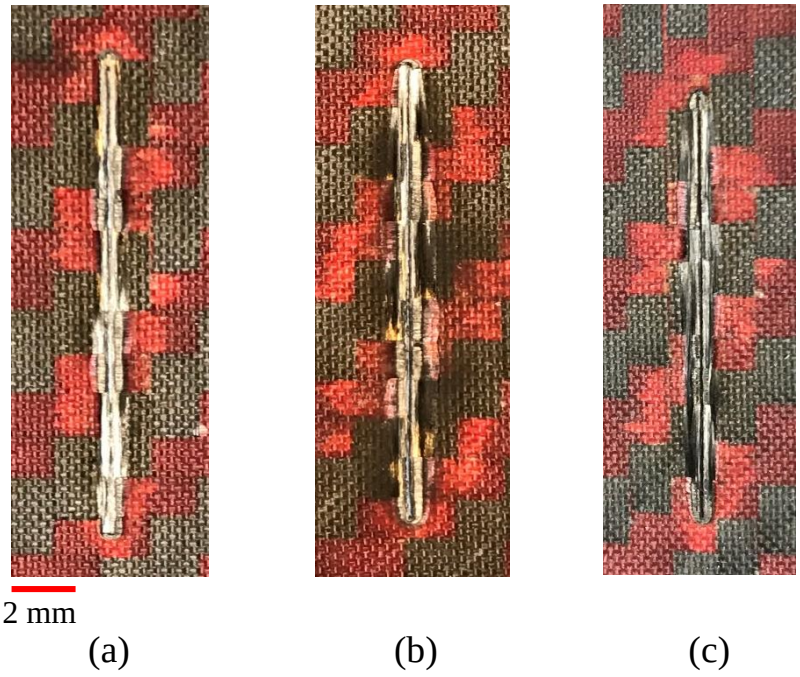

Figure A: Samples of laser cutting at different regions of carbon/Kevlar composite (experiment standard order No. 1)

Table A: HAZ measurement of different regions and error calculation based on comparison with each other

Samples of laser cutting at different regions and HAZ measurement		
(a)	(b)	(c)
0.662 mm	0.680	0.656
Calculated error (%) [$(HAZ_1-HAZ_2)/(HAZ_1+HAZ_2)/2*100$]		
(a) & (b)	(a) & (c)	(b) & (c)
2.6 %	0.9 %	3.5 %

Appendix 3 – HAZ and Kerf Width Measurement

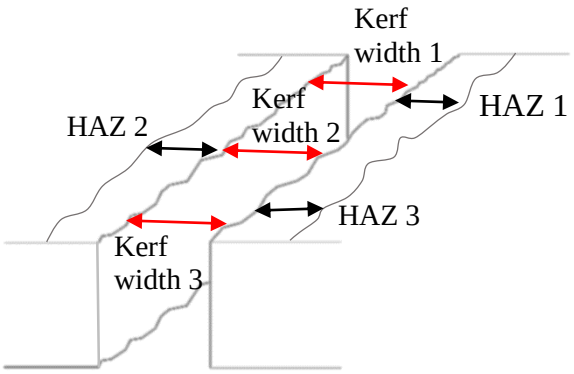

$$\text{Average kerf width} = \frac{\text{kerf width 1} + \text{kerf width 2} + \text{kerf width 3}}{3}$$

$$\text{Average HAZ} = \frac{\text{HAZ 1} + \text{HAZ 2} + \text{HAZ 3}}{3}$$

Figure B: Schematic diagram for measuring HAZ and kerf width

Table B: Measured kerf widths and HAZs for performed experiments including their average and standard deviation

Experimental input parameter				Response		
No.	Laser Power (W)	Cutting Speed (mm/s)	Standoff Distance (mm)	Top kerf width, T_k (mm)	Bottom kerf width, B_k (mm)	HAZ (mm)
1	36	15	50.8	0.748 0.768 0.759 $\bar{x}$ = 0.758 σ = 0.008	0.749 0.752 0.762 $\bar{x}$ = 0.754 σ = 0.0055	0.651 0.695 0.640 $\bar{x}$ = 0.662 σ = 0.023
2	40	15	50.8	0.805 0.825 0.813 $\bar{x}$ = 0.814 σ = 0.008	0.809 0.819 0.811 $\bar{x}$ = 0.813 σ = 0.004	0.675 0.7 0.695 $\bar{x}$ = 0.69 σ = 0.01
3	36	25	50.8	0.672 0.675 0.682 $\bar{x}$ = 0.676 σ = 0.0041	0.652 0.649 0.658 $\bar{x}$ = 0.653 σ = 0.0037	0.447 0.452 0.455 $\bar{x}$ = 0.451 σ = 0.0032

Table B continued

No.	Laser Power (W)	Cutting Speed (mm/s)	Standoff Distance (mm)	Top kerf width, T_k (mm)	Bottom kerf width, B_k (mm)	HAZ (mm)
4	40	25	50.8	0.682 0.699 0.689 $\overline{x}$ = 0.69 σ = 0.0069	0.679 0.692 0.687 $\overline{x}$ = 0.686 σ = 0.0053	0.509 0.512 0.524 $\overline{x}$ = 0.515 σ = 0.0064
5	36	20	49.8	0.81 0.819 0.823 $\overline{x}$ = 0.817 σ = 0.0054	0.759 0.769 0.773 $\overline{x}$ = 0.767 σ = 0.0058	0.491 0.498 0.508 $\overline{x}$ = 0.499 σ = 0.0069
6	40	20	49.8	0.882 0.888 0.897 $\overline{x}$ = 0.889 σ = 0.0061	0.814 0.82 0.829 $\overline{x}$ = 0.821 σ = 0.0061	0.654 0.663 0.665 $\overline{x}$ = 0.661 σ = 0.0047
7	36	20	51.8	0.94 0.954 0.96 $\overline{x}$ = 0.951 σ = 0.0083	0.936 0.943 0.941 $\overline{x}$ = 0.94 σ = 0.0029	0.656 0.67 0.665 $\overline{x}$ = 0.664 σ = 0.0057
8	40	20	51.8	0.965 0.974 0.98 $\overline{x}$ = 0.973 σ = 0.0061	0.997 1.01 0.987 $\overline{x}$ = 0.998 σ = 0.0094	0.755 0.744 0.758 $\overline{x}$ = 0.752 σ = 0.006
9	38	15	49.8	1.012 1.022 1.016 $\overline{x}$ = 1.017 σ = 0.0041	0.97 0.975 0.986 $\overline{x}$ = 0.977 σ = 0.0066	0.725 0.72 0.719 $\overline{x}$ = 0.721 σ = 0.0026
10	38	25	49.8	0.705 0.692 0.696 $\overline{x}$ = 0.698 σ = 0.0054	0.605 0.611 0.616 $\overline{x}$ = 0.611 σ = 0.0044	0.555 0.549 0.558 $\overline{x}$ = 1.017 σ = 0.0037
11	38	15	51.8	1.007 1.015 1.01 $\overline{x}$ = 1.011 σ = 0.0033	1.038 1.05 1.045 $\overline{x}$ = 1.044 σ = 0.0049	0.815 0.82 0.819 $\overline{x}$ = 0.818 σ = 0.0021

Table B continued

No.	Laser Power (W)	Cutting Speed (mm/s)	Standoff Distance (mm)	Top kerf width, T_k (mm)	Bottom kerf width, B_k (mm)	HAZ (mm)
12	38	25	51.8	0.687 0.699 0.692 $\bar{x}$ = 0.693 σ = 0.0049	0.712 0.718 0.708 $\bar{x}$ = 0.713 σ = 0.0041	0.427 0.432 0.424 $\bar{x}$ = 0.428 σ = 0.0033
13	38	20	50.8	0.759 0.751 0.748 $\bar{x}$ = 0.753 σ = 0.0046	0.758 0.763 0.773 $\bar{x}$ = 0.765 σ = 0.0062	0.568 0.573 0.58 $\bar{x}$ = 0.574 σ = 0.0049
14	38	20	50.8	0.693 0.7 0.688 $\bar{x}$ = 0.694 σ = 0.0049	0.694 0.686 0.697 $\bar{x}$ = 0.692 σ = 0.0046	0.565 0.569 0.576 $\bar{x}$ = 0.753 σ = 0.0045
15	38	20	50.8	0.71 0.72 0.724 $\bar{x}$ = 0.718 σ = 0.0058	0.748 0.743 0.755 $\bar{x}$ = 0.749 σ = 0.0049	0.591 0.583 0.597 $\bar{x}$ = 0.590 σ = 0.0057

Note: $\bar{x}$ = Mean, σ = Standard deviation

$$\sigma = \sqrt{\frac{1}{N}\sum_{i=1}^{N}(x_i - \bar{x})^2}$$